Investigating effects of interpass time during hot finish rolling on the evolution of texture in AA3104 Can Body Stock

Prepared by:

Ms. Nkopo Chaole

Centre for Materials Engineering

Department of Mechanical Engineering

University of Cape Town

Supervisors:

Dr. Sarah George, Dr. Nasheeta Hanief

Submitted to the Centre for Materials Engineering, Department of Mechanical Engineering at the University of Cape Town in partial fulfilment of the academic requirements for a Master of Science degree in Materials Engineering

February 2025

Key Words: Hot finish rolling, plane strain compression, Interpass time, recovery, recrystallisation, texture

PLAGARISM DECLARATION

1. "I know the meaning of plagiarism and declare that all the work in the document, save for that which is properly acknowledged, is my own. This thesis/dissertation has been submitted to the Turnitin module (or equivalent similarity and originality checking software), and I confirm that my supervisor has seen my report and any concerns revealed by such have been resolved with my supervisor."

2. Each significant contribution to, and quotation in, this project from the work or works of other people has been attributed and has been cited and referenced.

3. This project is my work.

4. I have not allowed and will not allow anyone to copy my work to pass it off as his or her work.

5. I acknowledge that copying someone else's assignment or project, or part of it, is wrong and declare that this is my work.

Signature: Signed by candidate

Date:

Acknowledgements

I wish to express my deepest gratitude to God Almighty for His guidance and strength throughout this journey.

I would like to convey my deepest appreciation to the following individuals and organisations for their invaluable contributions to my research:

- **Dr. Sarah George**, my supervisor, for her unwavering support, insightful guidance, and assistance with laboratory equipment during my research.
- **Dr. Nasheeta Hanief**, my co-supervisor, for her mentorship, extensive support in my SEM-EBSD training, and invaluable guidance throughout this process.
- **Professor Robert Knutsen**, for his generous time assisting with EBSD, expert advice, and continuous support.
- **Mr Ernesto Ismail and Daniel Slater,** for their help in paramaterial.
- **Mike Shirran**, for his guidance and assistance.
- **Penny Louw**, for her support and assistance with my experiments in the lab.
- **Maxwell Vos**, for his help with my experiments.
- **Dr. Arno Janse Van Vurren**, for his assistance in conducting EBSD tests at NMU.
- **Soraya Von Willingh**, for her help and support at EMU.
- The **staff and students of the Centre for Materials Engineering (CME)** for their encouragement and assistance in the lab.
- To **my family and friends** for their steadfast support and constant encouragement
- **Hulamin** for supplying the samples, supporting the project, and providing financial assistance.

It has been a truly rewarding experience working on this project, and I am immensely grateful for the support and guidance I have received along the way.

Abstract

During the hot rolling process of aluminium strips using a single stand reversing mill, there is inter-pass time variability along the strip length, resulting in non-uniform microstructure and texture development, impacting the final mechanical properties of the material. During this multipass process, the leading end (LE) and tailing end (TE) interchange their positions with each pass. Therefore, the material at the LE and TE of the strip experience different thermomechanical process histories. During hot rolling, deformation and annealing processes occur simultaneously. The nature of the dominant annealing mechanism, be it recovery or recrystallisation, will effectively reduce the strain accumulated in the structure owing to plastic deformation. The strain accumulation is further reduced during extended softening periods (interpass times) through rearrangement or reduction of dislocations by static recovery or recrystallisation.

This study investigates the microstructure and texture evolution in AA3104 Can Body Stock (CBS) during hot finish rolling by simulating multi-pass, high temperature rolling using plane strain compression tests using a Gleeble 3800. Two scenarios were simulated: Position A, with a longer inter-pass time between the first two passes (P1 and P2) and a shorter time before the third pass (P3), and Position B, with a short interpass time between P1 and P2 and then a longer inter pass time before P3. Post-deformation, samples were quenched, then annealed and analysed using Polarised Optical Microscopy (POM) and Scanning Electron Microscopy equipped with Electron Backscatter Diffraction (SEM-EBSD). Cube texture (Cb), a recrystallisation texture component, was used as a comparative metric to study the effect of variability in interpass time on texture evolution during hot finish rolling.

The results showed that Position A exhibited a combination of small and larger grain sizes, while Position B showed a uniform grain size distribution. According to grain orientation spread (GOS) results, it can be assumed that there was static recovery during the longer interpasses. This was evidenced by the highly recovered grains in position B after the longer interpass time experienced after P2. Furthermore, hardness testing revealed that due to the extended softening period between P2 and P3, the strain accumulation was reduced, ultimately leading to a lower stored energy within the final structure after P3. While position

A, which experienced a short interpass time between P2 and P3, exhibited a higher stored energy in the final structure after P3.

Interrogation into the texture after a recrystallisation anneal post P3 revealed that Position A, with a long-short interpass time combination, exhibited stronger Cb texture as a dominant texture component while Position B, with short-long interpass time combination, exhibited Gs and P texture as the dominant texture components. These variations highlight the role of recovery and recrystallisation behaviour taking place during inter-pass time and the influence thereof on the grain structure and texture development during hot rolling. Moreover, the results suggested that the development of Cb texture also depends on the initial texture before recrystallisation. Position A exhibited a stronger and higher volume fraction of Bs texture following deformation in P3, as well as a stronger and higher volume fraction of Cb texture after recrystallisation. This observation suggests that during the recrystallisation anneal heat treatment process, Bs-oriented grains may have transformed into Cb-textured grains through the migration of special grain boundaries, specifically coincident site lattice (CSL) boundaries.

The insight gained from these results can be used as a guide for proposals or troubleshooting of process parameter changes for process optimisation during the hot rolling of AA3104 CBS material.

Table of contents

List of figures

List of tables

List of equations

List of Abbreviations

Bs: Brass

Cb: Cube

CBS: Can Body Stock

CSL: Coincidence Lattice Site

Cu: Copper

D&I: Drawing and Ironing

EBSD: Electron Backscattered Diffraction

GOS: Grain Orientation Spread

Gs: Goss

HAGB: High Angle Grain Boundary

KAM: Kernal Average Misorientation

LAGB: Lower Angle Grain Boundary

LE: Leading End

Mn: Manganese

ND: Normal direction

ODF: orientation distribution function

P: Pass

POM: Polarized Optical Microscopy

PSC: Plane Strain Compression

PSN: Particle Site Nucleation

RD: Rolling direction

RXN: Recrystallisation

SEM: Scanning Electron Microscope

SFE: Stalking Fault Energy

SIBM: Strain-Induced Boundary Migration

t: Interpass time

TD: Transfers Direction

TE: Tailing End

1. Introduction

1.1. Background and motivation of study

Aluminium possesses attractive properties such as lightweight, ductility, and a high strength-to-weight ratio, making it highly desirable for various applications. This has led to its extensive use in buildings, boats, cars, household appliances, packaging, computers, cell phones, and more. However, the formability of aluminium sheets is poor compared to commercial steel; therefore, it is essential to control and enhance random texture, which is associated with improved formability. Aluminium semi-fabricators supply rolled sheets to manufacturers of finished products, such as beverage cans and other food packaging. A common food packaging material is AA3104-H19 aluminium alloy can body stock (CBS) material used for the manufacture of the body of beverage cans.

During the thermomechanical processing of AA3104-H19, the goal is to maximise Cb texture during the inter-annealing heat treatment. In multi-stand hot rolling mills, complete recrystallisation can occur naturally through self-annealing due to the continuous processing at elevated temperatures. However, in a single stand reversing mill, this is not possible because the material cools between passes. As a result, the hot-rolled material may require an inter-annealing treatment—heating it to a high temperature after rolling—to induce recrystallisation. This heat treatment promotes the development of the Cb texture, which is primarily responsible for the formation of 0° and 90° ears during deep drawing. On the next stage of processing, cold rolling, strong rolling textures are introduced. These rolling textures contribute to the formation of 45° ears during deep drawing.

In CBS applications, both Cb and rolling textures are essential. By carefully balancing these textures will result in a product with minimal anisotropy, ensuring a balance between recrystallisation and deformation textures, which helps to minimise earing during subsequent forming (deep drawing and wall ironing). Earing refers to the uneven, wavy edges that form along the rim of a cup or drawn part during the deep drawing process. This phenomenon occurs due to the anisotropy of the plastic strain ratio (r), which affects the material's ability to deform uniformly[1], [2]. During deep drawing, the plastic strain ratio determines the flow of metal and the extent of wall thickening in various directions. Anisotropy causes non-uniform metal flow, resulting in the formation of ears in regions where the material's

deformation resistance is higher or lower. Controlling texture evolution, as well as minimising anisotropy, helps to reduce earing and improve the quality of the drawn part.

Excessive plastic anisotropy is undesirable because it can lead to poor mechanical properties [3]. It also leads to incomplete trimming of a drawn and ironed (D&I) can body and uneven distribution of stress in the final product, compromising the structural integrity and performance of the can body. Furthermore, additional steps must be employed to correct the ears, which increases the production costs. This trimming of the ears means that a significant amount of material is lost during manufacture. Additionally, studies have indicated that these ears often cause the can body maker to jam during subsequent re-drawing and ironing processes, resulting in machine downtime and a reduction in productivity [4]. Therefore, the production processes of AA3104-H19 metal sheets must be controlled to optimise productivity and produce metal sheets with desirable properties by minimising anisotropy. To create metal sheets with low anisotropy (low earing), the rolling textures (S, Cu, and Bs), characterised by ears at 45^{o}, must be balanced by recrystallisation texture, preferably Cb texture, characterised by ears at 0/90^{o} [3]. Thus, controlling the entire production process to control texture evolution and maximising Cb texture development during hot rolling to the re-roll gauge is essential. Furthermore, it is important to find optimum parameters that will lead to the development of the desired texture and microstructure at each step of the process.

During the hot rolling process of aluminium strips using a single stand reversing mill, there is inter-pass time variability along the strip length, resulting in non-uniform microstructure and texture development, impacting the final mechanical properties of the material. During this multipass process, the leading end (LE) and tailing end (TE) interchange their positions with each pass. Therefore, the material at the LE and TE of the strip experience different thermomechanical process histories. During hot rolling, deformation and annealing processes occur simultaneously. The nature of the dominant annealing mechanism, be it recovery or recrystallisation, will effectively reduce the strain accumulated in the structure owing to plastic deformation. The strain accumulation is further reduced during extended softening periods (interpass times) through rearrangement or reduction of dislocations by static recovery or recrystallisation.

To this end, this study aims to investigate the microstructure and texture evolution in AA3104 CBS during hot finish rolling by simulating multi-pass deformations that based on industrial processing parameters. Two scenarios were simulated: Position A, with a longer inter-pass time between the first two passes (P1 and P2) and a shorter time before the third pass (P3), and Position B, with a short interpass time between P1 and P2 and then a longer inter pass time before P3.

1.2. Objectives of the study

The objectives of the study are to:

- Perform a series of plane strain compression (PSC) on AA3104 transfer bar material representing the full thermomechanical history for positions A and B to simulate the hot finish rolling using Gleeble 3800,
- Characterise the microstructure and texture development of positions A and B at all critical steps throughout the full rolling sequence.
- Characterise the final texture for positions A and B after finishing rolling, followed by a simulated batch/recrystallisation anneal to use Cb texture volume fraction as a comparative metric.

1.3. Methodology

To achieve these objectives, metal samples were sectioned from a transfer bar to fit 12mm thickness (normal direction) by 20mm transverse direction by 30mm rolling direction. The project incorporated plane strain compression (PSC) testing on the Gleeble 3800. Samples underwent varied simulated thermomechanical processing, and samples were quenched and then exposed to a controlled recrystallisation anneal after deformation to allow for a fully recrystallised microstructure. The samples were then sectioned and metallographic prepared by grinding and polishing to mirror the finish, and the properties, microstructural, and texture evolution were characterised. Microstructure and texture evolution incorporated POM (Polarized Optical Microscopy), SEM (Scanning Electron Microscope), and EBSD micro-texture analysis.

1.4. Scope and limitations of the study

Several studies [3]– [6] have investigated how different processing parameters affect the microstructure and texture evolution of aluminium alloys, more specifically on the centre part of the hot transfer bar. However, few studies [9], [10] take into consideration how the microstructure and texture evolution of the centre of the transfer bar compares to that of the edge or how the inter-pass time affects the microstructure and texture of the edges during hot finish rolling on a single stand reversing mill. Theoretically, material rolled in a single-stand hot finish mill (HFM), typically in three passes, is more likely to exhibit greater microstructural variation compared to that processed in a three-stand tandem HFM. This is because the time between successive deformations (inter-pass time) in a single stand reversing HFM is not uniform, varying along the length of the strip from one end to the centre and the other end.

Compared to a three-stand tandem HFM, a single-stand HFM (typically operating in three passes) introduces greater microstructural variation due to non-uniform inter-pass times. These times fluctuate from one end of the strip to the centre and the other end, leading to inconsistencies in deformation. Additionally, variations in rolling speed caused by acceleration and deceleration during coiling and uncoiling, along with intermittent delays from threading challenges, further contribute to these fluctuations [10]. This study specifically investigates how these variations, along with strain per pass, influence the final microstructure and texture of the material. The microstructural and texture analyses are specifically conducted on the transfer bar centre, the leading and tail ends of both deformed and annealed samples. However, in this study, only the microanalysis of textures will be conducted using EBSD and macro analysis of texture using XRD will not be employed.

1.5. Aim of the study

This study investigates the effects of inter-pass time variability experienced during hot finish rolling of AA3104 can body stock on a single stand reversing mill, where the leading (LE) and tail (TE) ends of the sheet experience different inter-pass times. This will be achieved by investigating the variations experienced at position A relative to position B on the final texture of the rolled sheet after simulated finish rolling conditions using plane strain compression (PSC) on the Gleeble 3800.

1.6. Research questions.

How do processing parameters affect the development of texture during each pass?

What effect does inter-pass time have on the texture evolution of position A and position B during each pass and on subsequent annealing?

2. Literature review

2.1. Overview

The physical and mechanical properties of aluminium make it the most widely used metal after steel on the market. It has a strength-to-weight ratio higher than steel and similar approaches for conductor cables. Aluminium also displays excellent electrical and thermal conductivity; it is ductile and corrosion-resistant; aluminium and aluminium alloys form a passive oxide layer upon reaction with oxygen which can spontaneously renew itself if it is damaged. Aluminium is easily formable and visually attractive, which makes interesting material for different applications. Aluminium is non-toxic and has no impact on taste, making it the preferred material in the food and packaging industry. It is commonly used for cans, foils, bakery equipment, and beverage cans. [11].

However, pure aluminium has a low yield strength of about 25MPa and it cannot be used where strength is a requirement. Therefore, aluminium has attracted researchers to improve its strength to meet the requirements of different applications. To improve the mechanical and physical properties of pure aluminium, different elements are added during the production process to produce aluminium alloys with distinct properties to fulfil the desired performance. Comparing the mechanical properties of pure aluminium and aluminium alloys, it has been proved that the addition of a small number of alloying elements produces an increase in yield strength, tensile strength, and the strain hardening response. Aluminium alloy series are classified according to the major alloying elements they contain, and they are further classified according to whether they are heat-treatable or not.

The initial strength of all aluminium alloys is improved by adding other elements. In non-heat-treatable aluminium alloys, strength can be further increased by cold working or strain hardening. In contrast, heat-treatable aluminium alloys gain additional strength through specific heat treatments. These treatments take advantage of the fact that certain alloying elements become more soluble in aluminium at elevated temperatures. By carefully controlling the heating and cooling processes, the alloy's strength is significantly enhanced.

The major alloying elements include copper, manganese, zinc, magnesium, and silicon. It has also been shown that combinations of these alloying elements influence the workability of

the material. Table *1* shows the classification of the aluminium alloy series with the major alloying elements.

Table 1 Classification of aluminium alloys *[11]*

Non hardening alloys are work hardened through cold working		
Main alloying element	*Serial number*	*Examples of alloys*
More than 99% pure, with traces of Cu, Fe, Si	1xxx	Al 99,0; Al 99,5; Al 99,85
Mn	3xxx	Al-Mn; Al-Cu-Mn-Mg
Mg	5xxx	AlMg3; Al-Mg-Mn-Cr
Other elements	8xxx	Al-Fe-Si; Al-Li-Mg-Cu
Hardening alloys are hardened through natural and artificial hardening		
Cu	2xxx	Al-Cu-Si-Mg
Si	4xxx	Al-Si-Mg
Mg, Si	6xxx	Al-Mg-Si
Zn	7xxx	Al-Zn-Mg-Cu

Each alloying element plays a significant role in the improvement of mechanical properties, hence the final performance of the material. Copper in the 2xxx series provides strength as it enables precipitation hardening, and silicon in the 4xxx series reduces the melting point of aluminium and improves its fluidity in the molten form [12]. Therefore, the 4xxx aluminium alloy series are used as filler materials in fusion welding and brazing [13]. As shown in Table *1*, the 3xxx series contains manganese, which provides a slight increase in the strength of the metal and high formability and drawability, which is the most desired property for the production of beverage cans [14].

2.2. AA3xxx series

AA3104 falls under the AA3xxx series. It is a non-heat treatable alloy with medium strength but good formability as well as good weldability, and excellent corrosion resistance. Since it is non-heat treatable, its strength can be improved by solute-solution strengthening and cold working; hence, can body stock is manufactured using a highly work-hardened state of AA3104 (AA3104-H19). The high strength is required to prevent buckling during deep drawing

and ironing and to provide strength for the can body, particularly the base dome. AA3014-H19 is the most widely used aluminium alloy in the production of beverage cans due to its good deep-drawing properties. It has better mechanical properties at elevated temperatures than the 1xxx aluminium alloy series. Table *2* shows other alloying elements, and their proportion amounts present in the AA3104 alloy.

Table 2 Other alloying elements are present in AA3104 aluminium alloy.

Elements	Al	Cu	Ga	Fe	Mg	Mn	Si	Ti	V	Zn	Other
Wt.%	95.0-98.4	0.05-0.25	≤0.05	≤0.80	0.80-1.30	0.80-1.40	≤0.60	≤0.10	≤0.05	≤0.25	≤0.15

2.3. Production of AA3014 Can Body Stock

The production process of AA3014 CBS involves several steps to achieve the required dimensions, microstructural and textural features, and mechanical properties for the final product. A schematic of the process is shown in Figure 1. Firstly, the primary metal, consisting of primary and recycled material, is melted at 660-700 ^{o}C and cast, producing ingots. Then, the ingots are homogenised at 550-600^{o}C for 4-8 hours to achieve a consistent microstructure. The homogenised slabs are then transferred to hot rolling mills for reduction of thickness. The hot rolling process consists of two critical steps: hot rough rolling and hot finish rolling. In a hot rough rolling mill, the slabs experience multiple passes through a single stand reversing mill to reduce the thickness by approximately 95%, producing a transfer bar. The transfer bar is transferred to the hot finish rolling mill, which also consists of a single stand reversing mill. The finish rolling is the most critical step in the production of CBS because deformation occurs at high temperatures whereby deformation and annealing, in the form of recovery and/or recrystallisation, occur simultaneously, thereby affecting the microstructure development. Most importantly, unlike tandem mills, a single stand reversing mill has coilers and decoilers on both ends. Thus, the leading end (LE) and tail end (TE) keep interchanging positions during the successive rolling passes.

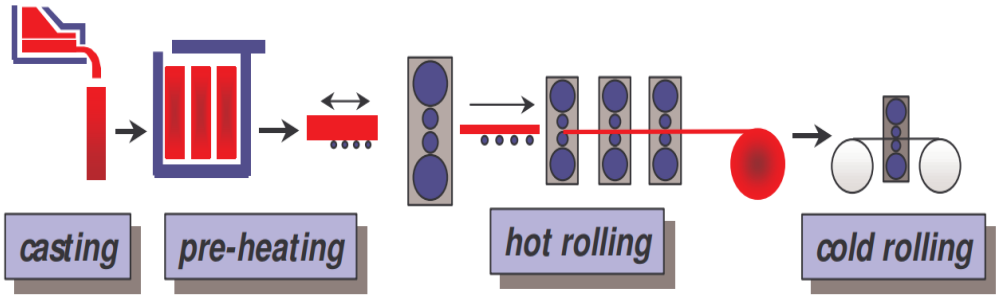

Figure 1 Process diagram for thermo-mechanical production of AA3104 can body stock [4], [15]

During finish rolling on a reversing mill, while the LE is deforming, the TE is restoring, and while the TE is deforming, the LE is restoring. The material at the LE and TE experiences different thermomechanical histories. Therefore, both positions ultimately attain different strain accumulation and time for annealing during inter-pass time. As a result, mechanical properties, microstructure, and texture evolution between the two positions vary. The evolution of crystallographic texture during the thermomechanical processing of aluminium strips results in the formation of extreme plastic anisotropy, which leads to poor mechanical properties [3], [16]. However, Hutchinson [17] showed that texture development, prevention and/or control of the Cb component, especially, are dependent on the specific commercial products or industrial processes. Table 3 shows some of the examples Hutchinson mentioned in [17] where Cb texture was required or had to be controlled.

Table 3 Examples of Cb texture control in industrial processes and products *[17]*.

Material	**Application**	**Requirement**
Aluminium alloys	Deep drawn boxes and cans	Balanced texture with mixture of cube and R components to minimize earing in both annealed and rolled conditions
Copper sheet	Processing of thin sheet and foil	Minimise cube texture as its presence leads to bad ductility and band breaks
Pure aluminium	Foil for electrolytic condensers	Maximise cube texture to optimize tunnel etching to increase the surface area
Nickel-iron permalloy	Soft magnetic material for field screening	Maximise cube texture to utilize the easy magnetization directions <100>
Nickel alloys	Substrate for high temperature superconducting phases	Sheet surface with (100)[001] orientation for epitaxial microstructure control
Copper	Photo-voltaic connection flat wires on silicon solar cells	<100> direction along the wire minimise Young's modulus to reduce loading and fracture of the silicon wafers

2.4. Texture

Texture refers to the preferred arrangement of grains within a polycrystalline material [18], [19]. It is a key microstructural characteristic that directly influences the material's degree of anisotropy and hence, the mechanical and physical properties of polycrystalline materials [18]. When the grain orientation is random, the material is said to be isotropic. Conversely, when the grains take a preferred orientation, the material is said to be anisotropic. This means that since the properties of the material depend on the individual grains, then the properties depend on the preferred orientation[18], [19]. This is because grain is a building block of material, and each grain has a preferred orientation and slip system.

Figure 2 shows a sheet of polycrystalline material where the orientation of each grain is described using a simple unit cell glyph rotated relative to the rolling direction (RD) of the material. Figure 2 (a) shows crystallites with preferred orientations, and (b) shows crystallites with random orientations.

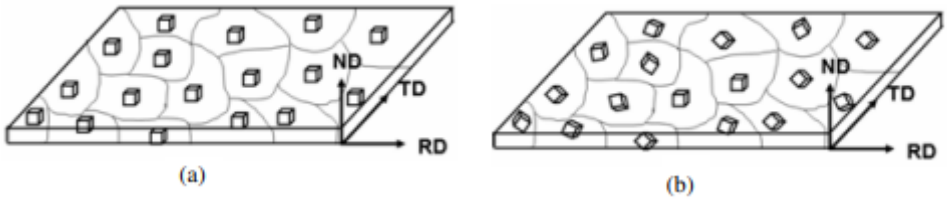

Figure 2 Schematic illustrations of a) preferred orientation and b) random orientation [19].

The metal castings have a random texture and some highly distinct deformation and recrystallisation textures, which depend on material, purity, and solidification conditions. But during metal processing, at every step, the texture gets modified, and it is very difficult to control it. The primary development of texture occurs during plastic deformation and the subsequent recrystallization process. A specific crystallographic texture is required to minimise the ears and increase productivity while reducing material losses and usage [20]. Literature shows that there should be a balance between recrystallisation texture intensities (Cube (Cb) {001} <100> and Goss (Gs) {110} <001>) and rolling texture intensities (β-fibre, Copper (Cu) {112} <111>, S {123} <634>, and Brass (Bs)) {110} <112>) on the cold rolled body sheet that is ready to be drawn into can bodies to control the production of ears on the can bodies during drawing [20], [21].

2.5. Representation of texture

Texture in a rolled strip of material can simply be presented by Miller indices {hkl}[uvw], where {hkl} represents planes of these grains which lie parallel to the sheet plane whereas [uvw] direction points to the rolling direction [19]. The most important concept of Miller indices representation is that it highlights important planes and directions that are parallel to the principal directions in the specimen, which are practical and important in texture analysis [22]. Furthermore, a less complicated texture can be represented using pole figures determined from x-ray diffraction (XRD) and EBSD methods. However, this method does not give full information to determine the true and complete texture of the material. Therefore, the orientation distribution function is normally used [19]. Figure 3 shows a schematic illustration of the (110) plane parallel to the normal plane (and perpendicular to the normal direction (ND)) of the sheet, and the direction [001] of the grain is parallel to the rolling direction (RD) of the sheet.

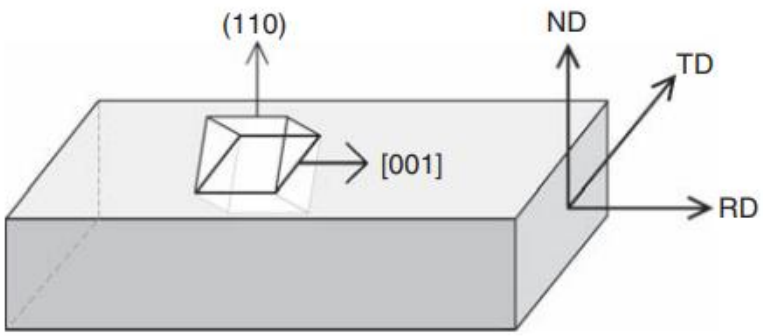

Figure 3 Schematic illustration of the relationship between the grain and specimen axes for the (110) [001]. The grain plane (110) is parallel to the normal plane of the specimen and the [001] direction of the grain is parallel to the rolling direction of the specimen [22].

2.5.1. Texture using pole figures.

A pole figure is a 2D stereographic projection where the axes are defined by an external reference. A specific hkl pole is plotted from all the crystallites in the polycrystalline material, with the external reference explained using the normal direction (ND), rolling direction (RD), and transverse direction (TD) [23]. Traditional pole figure measurements are constructed by

recording the intensity of a certain X-ray diffraction angle as a function of rotation and tilt of the sample. Pole figures are used to characterise well-known texture components qualitatively [18]. A polycrystalline material with a random texture is shown in Figure 4 (a), and if a material has some degree of texture, it will be shown in Figure 4 (b).

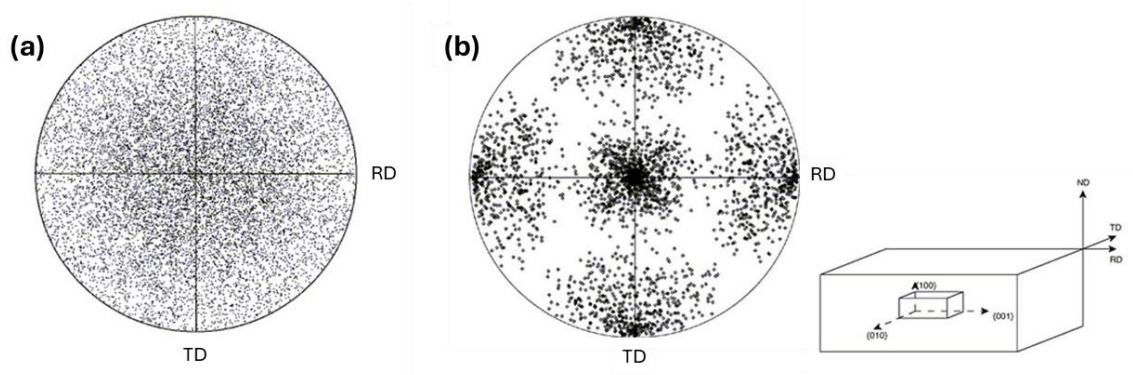

Figure 4 Pole figures showing (a) the random orientation and (b) some degree of texture [23].

The representation of texture on the pole figures can also be shown using contours, especially where many grains are involved as poles may overlap and obscure the true orientation density. Regions of high orientation density are shown by large numbers of closely stacked contour lines, while regions of low orientation are shown by few lines which are widely spaced. Figure 5 shows an illustration of pole figures using contour lines.

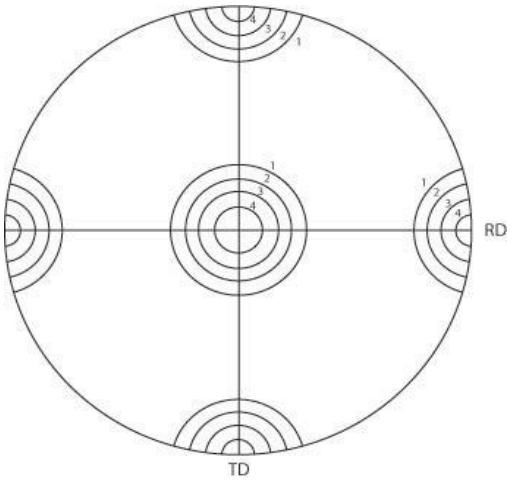

Figure 5 Pole figure showing preferred orientation using contour lines [23].

2.5.2. Texture using Orientation distribution function (ODF)

The disadvantage of using pole figures is that it provides insufficient information on the orientation of the grains because poles from different orientations may overlap making it difficult to identify the orientation of individual grains. Furthermore, it is not easy to record the entire pole figure range [22]. Therefore, to quantitively characterise the crystallographic texture of a polycrystalline material, the Orientation distribution function (ODF) in Euler space per Bunge notation must be used as they have higher resolving power [18], [19]. Volume fractions of ideal texture components can be quantified from an ODF. The ODF describes the orientation of each grain concerning three Euler angles (ψ_1, ϕ, ψ_2), which define the orientation between the crystal axes using a 3-dimensional orientation space [18], [19], [22]. The complete ODF consists of a set of rotations representing each grain in the specimen. ODFs are constructed from pole figures using different mathematical models [19] that include harmonic methods and discrete methods.

Comparing the two methods, the discrete method is suitable for sharp textures and low symmetries, as it reduces the required number of pole figures. In contrast, the harmonic method is suitable only for smooth textures and requires a significantly large number of pole figures for materials with low crystal symmetry [18]. Furthermore, harmonic methods may lead to false intensities called ghost peaks, which can be limited by using discrete methods. However, harmonic methods can be computed very quickly with low computer memory because each order of expansion can be computed separately. Even though discrete methods consider various symmetries, they require a lot of computing memory, and experimental data accuracy is more critical than in harmonic methods [18].

2.6. Measurement of texture

The techniques that are used for texture analysis are based on the diffraction of radiation by a crystal lattice [22]. Crystallographic lattice planes can diffract radiation at a certain angle, and this provides information on their arrangement and orientation of the sampled volume of material concerning some fixed reference axes. The angles θ at which diffraction occurs depend on both the wavelength λ and the spacing of the scattering atoms d according to

Bragg's law. Bragg diffraction is a 3D periodic, and it is the result of waves reflected from different crystal planes. Equation 1 below explains Bragg's law,

$$n\lambda = 2d\,sin\theta \qquad \textit{Equation 1}$$

where λ = wavelength, n = the order of reflection, d = the interplanar spacing, and θ =angle of the diffracted wave

Bragg's law is crucial when measuring texture, if the wavelength of the radiation used is known, the lattice planes which diffracted the radiation can be identified from the measured Bragg angles through which the waves are diffracted. A diffraction pattern is created by measuring the intensity of scattered waves at different scattering angles. Intense peaks, called Bragg peaks, appear in the pattern when the scattered waves fulfil Bragg's Law. Each set of overall has a specific interplanar spacing d, which is related to the lattice constant (a) shown in the Equation 2.

$$d = \frac{a}{\sqrt{h^2+k^2+l^2}} \qquad \textit{Equation 2}$$

where d= interplanar spacing, a = lattice constant and h, k, l = {hkl} points

Therefore, given that the lattice constant is known, the individual peaks can be constructed using Bragg's law.

2.6.1. X-rays

X-ray diffraction (XRD) is the oldest and most common method used for texture analysis, originally employed by Wever [13] – [15], [17]. XRD provides information on the overall macrotexture of a material volume from a flat specimen by measuring the intensities of diffraction maxima, and X-ray tubes or synchrotrons are used as X-ray sources [22]. Just like other methods, Bragg's law is applied. To determine the preferred orientation of the sample with a known set of crystal planes {hkl}, a monochromatic beam of radiation of a specific wavelength is used, and the detector is set to proper Bragg angle, 2θ of the diffraction peak of interest [22], [24]. Then, the sample is rotated in a goniometer until crystal plane hkl is in the reflection condition [19], [22]. When a polycrystalline material is rotated, the grains in the sampled volume may align such that their crystal planes {hkl} meet the Bragg condition for their interplanar spacing, resulting in a measured diffracted intensity [22]. The direct output

from an X-ray texture goniometer is a chart that displays the diffracted intensity relative to the specimen's rotation angles. This data can be represented in a pole figure or used to calculate the 3-D Orientation Distribution Function (ODF).

To determine the texture, a reflection or transmission method can be used, where a sample with a large thickness and plane surface can reflect the X-rays while the thin slab of thickness can allow X-rays to penetrate. Since x-rays are easily absorbed by matter, the transmission method is only applicable to a very thin sample and materials with incredibly low absorption and these include metals such as Al, Be, and Mg, but most pole figures are constructed using the reflection method [25]. XRD is fast and easy to perform on an X-ray laboratory diffractometer, but there is a high chance of defocusing effects, as a result, XRD employs sophisticated corrections which must be performed on the measured intensities and in practice, measurements are generally not possible when the tilt angle is below approximately $\sim 25^{\circ}$ [18], [24]. Moreover, a high number of diffraction peaks and smaller angular distance may cause overlap even at low or moderate tilt angles [19]. It gives an average texture to the material and is best used to complement another technique.

2.6.2. Neutron diffraction

Neutron diffraction is one of the methods used for texture analysis, and it works similarly to XRD. However, since neutrons are scattered by the atomic nucleus, their interaction is much weaker than that of X-rays, which interact with shell electrons. This results in significantly lower absorption and much higher penetration depth for neutrons [13] – [15], [17]. Due to low absorption, it is suitable for bulk texture investigations of large-volume samples and in-situ texture analysis for texture changes during heating, cooling, or in-situ deformation [18], [24]. However, neutron diffraction demands nuclear reactors with a constant flux of thermal neutrons or with pulsed neutrons at spallation sources which is extremely expensive. Furthermore, due to weak interaction, it requires an exceedingly long time for analysis.

2.6.3. Electron diffraction

Like X-ray diffraction and neutron diffraction, electron diffraction is also based on Bragg's law, but it utilises a beam of electrons to generate a diffraction pattern [26], [27]. Different diffraction patterns from numerous grain orientations can be found by tilting the sample for the incident electron beam [28]. Therefore, the crystal structure can be mapped in three dimensions. Unlike XRD, electron diffraction intensity is remarkably high because electrons are less penetrating, and they can scatter more intensely [27]. As a result, electrons are sensitive, even on a very thin layer sample, thus giving a strong diffraction pattern in a brief time. Furthermore, electron diffraction techniques can obtain crystallographic information with high accuracy and high resolution [26], [27]. Among all the electron diffraction techniques, SEM-EBSD is the most common for the analysis of texture due to the easy availability and operation of a scanning electron microscope (SEM) [19]. Moreover, it does not require much background in texture theory from the user.

2.7. SEM-EBSD

In this technique, as electrons are bombarded on the sample, they interact with the uppermost surface layer of the sample producing electron back-scatter diffraction patterns (EBSD), which are captured on the phosphor screen and recorded with a low-intensity video camera or a CCD device [19]. The diffraction pattern is unique to the crystal structure and orientation at the point (or volume) where the electron beam interacts with the sample [29]. Therefore, this pattern can be used to analyse crystal orientation, distinguish between crystallographically distinct phases, characterise grain boundaries, and offer insights into the local crystalline quality. EBSD enables detailed analysis of localized features in heterogeneous samples, providing spatially distributed information that can be visualized in maps and images [29]. Areas of different sizes can be mapped depending on the purpose, whether large or small, while still achieving high resolution. For example, mapping a 50 × 50 µm area with a 0.2 µm step size can yield an indexing rate above 70%, providing a detailed map of deformed samples. Additionally, the montage technique can be used to stitch together smaller maps, allowing the creation of a much larger map—such as 1700 × 900 µm—with a 1 µm step size, achieving indexing rates above 90%. However, indexing rates also depend heavily on the

quality of sample preparation. For instance, recrystallised aluminium samples can achieve up to 100% indexing, whereas deformed samples may have lower indexing due to overlapping diffraction patterns. Using smaller step sizes enhances detail, as they increase the number of pixels analysed in the scanned area.

It allows the determination of local texture information in a quantitative manner, which is very important in the study of recrystallisation [25], and it also aids in bridging the gap between bulk texture measurement techniques such as XRD [19]. Even though SEM-EBSD is a commonly used technique for texture measurements, there are still some drawbacks: sample preparation is extremely crucial, and the automatic indexing process is not often dependable. Failing to thoroughly prepare the sample can lead to the reproduction of texture artefacts [19].

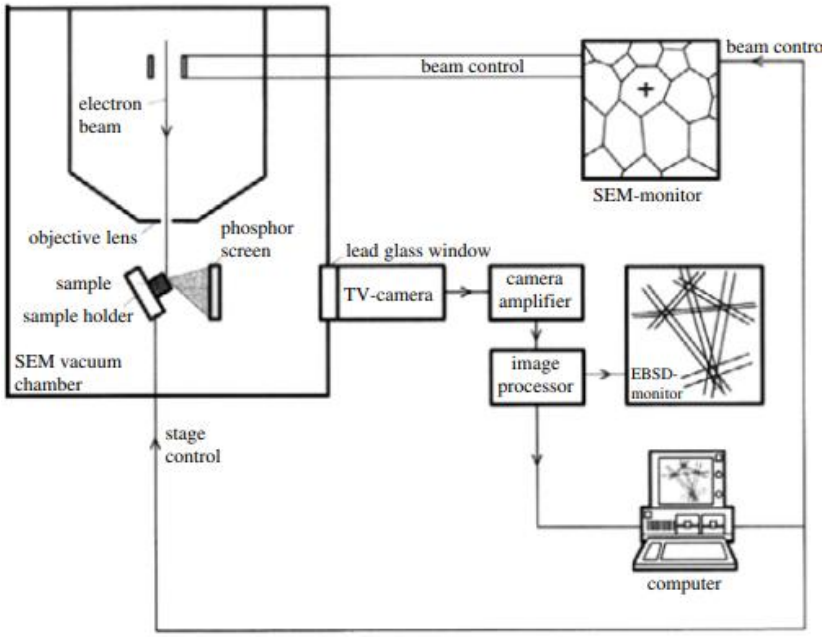

Figure 6 Illustration of EBSD setup.

2.8. Can body manufacture

Due to a combination of strength and formability of AA3014 aluminium alloy, it is an ideal alloy for the production of beverage cans. To acquire the strength requirements, AA3104 can body stock is used in H19 temper, which is a heavily work-hardened state [30]. Can bodies require high strength to sustain structural stability and avoid buckling of the can base under

high internal pressure, as for the very thin can wall of < 0.1mm after ironing [15]. The production of a can involve several processing stages, which are shown in Figure 7 and it is clearly explained by Hosford and Duncan [31]. The first step of the can body manufacturing process is carried out in a “Cupper”, where circular or near circular blanks are stamped from coiled sheets and then deep drawn to form cups. Thereafter, they are redrawn and ironed on the body maker to meet the required height. Finally, the cups are trimmed to remove ears at the top of the can to set an even cup height. Next, the body undergoes necking to match the outer diameter of the lid, and the can end is then attached to the body, forming a flange [23], [25]– [28].

Non-circular blanks can also be used, as demonstrated by Zaky et al. [34], who showed that cups drawn from circular blanks always form ears, while cups drawn from non-circular blanks significantly minimise earing. This highlights the importance of closely controlling earing in CBS.

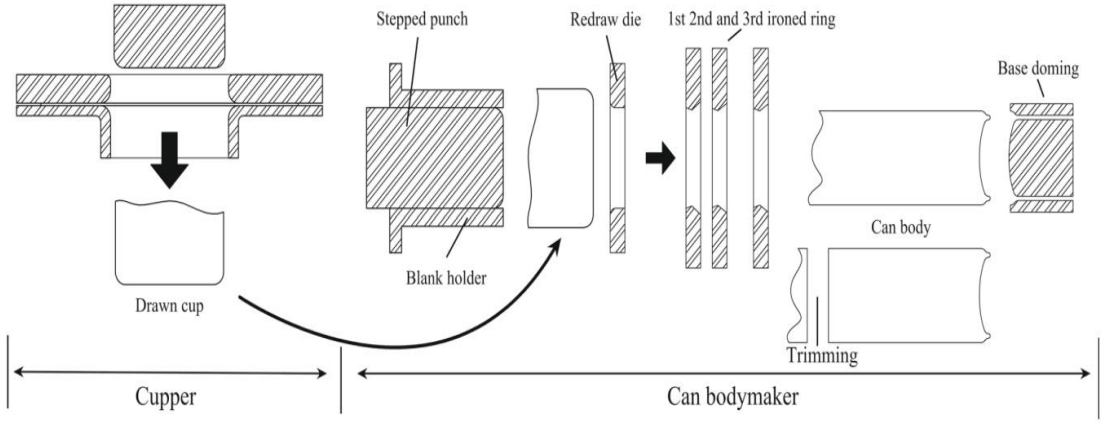

Figure 7 A general manufacturing process of aluminium can bodies [33].

Texture and microstructure development are especially important phenomena to take into consideration during the manufacturing process of can body stocks. Materials’ strong anisotropy behaviour, which is related to texture, can cause unacceptable effects on the properties of the part being produced [35]. Studies have shown that failure to control and balance texture during can body stock processing can lead to poor formability properties of the material and the development of uneven rims on the can called ears during the deep drawing and ironing process of can bodies [4], [15], [20], [21], [32], [35]. Earing is also produced in the sidewall of the can, giving rise to an uneven flange diameter [21]. Ears are

associated with many problems, which can lower productivity and loss of material [4], [30] [15].

Engler [4] explained that some conditions may result in a two-fold earing, and under these circumstances, the specimens cannot endure the hold-down pressure that supports the blank during can forming without experiencing some circumferential flow and pinching. The pinched ears that form can cause the body maker to jam during subsequent re-drawing and ironing, leading to machine downtime and decreased productivity. Furthermore, the wavy cup rims are destructive to the transport of the can bodies, and they can also result in pinholes or cracking during the ironing of the can body [15], [21]. Earing can be quantitatively expressed as a single number, Z, where Z is defined as the ratio of the average height of ears (h_e) to the average height of troughs (h_t). Material with earing values Z < 5% and ΔZ > 0% is acceptable to produce Al beverage can [15], [30]. The expression for ΔZ can be found in Equation 3.

$$\frac{2h45º - (h0º + h90º)}{h0º + h90º} \qquad \textit{Equation 3}$$

Recrystallisation texture is associated with the formation of ears at 0°, 90°, 180°, and 270° with Cb texture at 0°/90° while rolling texture is associated with ears at 45° (45°, 135°, 225°, 315°) [1], [4]. Literature also shows that before cold rolling the AA3104 can body sheet, Cb texture must dominate during recrystallisation after hot finishing rolling. During cold rolling, Cb-oriented crystals rotate, reducing 0°/90° ears and increasing 45° ears [1], [4]. Depending on the amount of cold work and prior Cb texture to cold working, three types of earing can occur, namely (b)type A (four ears), type B (c) (six years), and (d) type C (eight ears), as explained in [1]. Shi et al. [1] explained that for commercial AA3014-H14, sheet type B is dominant as shown in Figure 8 (c). The 45° ears produced during cold rolling are balanced off by a Cb texture, which is retained from the recrystallised hot strip because Cb-oriented grains slowly rotate and the resulting 0°/90° ears can offset the newly forming 45° ears even under high rolling reductions. As a result, the cup height profile displays a distinct six-ear pattern, with ears positioned at 0°, 45°, 135°, 180°, 225°, and 315° relative to the rolling direction (RD), while the ears at 90°/270° are eliminated as shown by type B in Figure 8 [1], [4], [21].

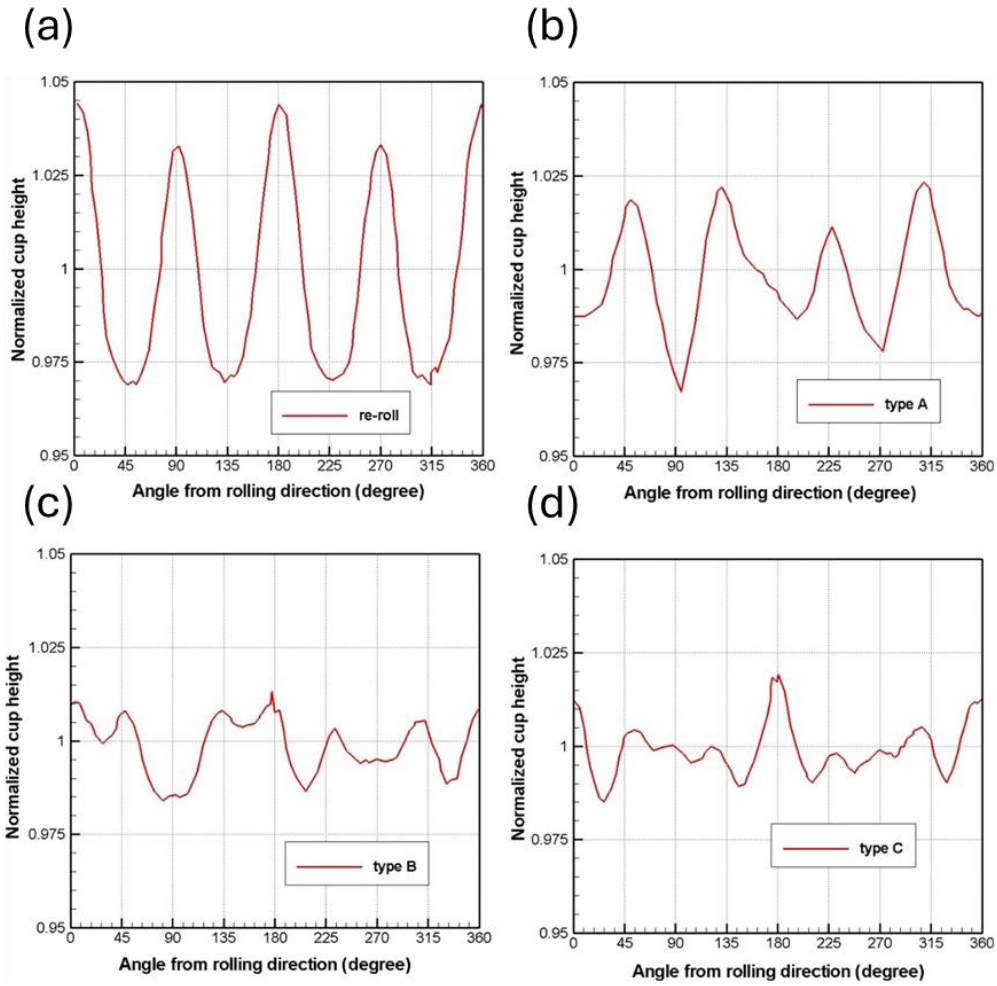

Figure 8 Different types of earing profiles of AA314 (a) re-roll, (b) type A at final gauge, (c) type B at final gauge, and (d) type C at final gauge [1]

On the other hand, texture can be very helpful; it can enhance the formability and drawability of the material. The drawability of the material can be measured by the Lankford parameter, r, which is the ratio of width strain to thickness strain in the rolling direction. When r, measured in the longitudinal, transverse, and 45° orientations, is unity or closer to one, the material is said to be randomly oriented, and when it ranges from 0.5 to 2.5 in cubic metals, it is to be textured [36]. During deep drawing, orientations with high values of r resist wall thickening, leading to the formation of troughs and improved formability in deep drawing [36]. In contrast, the low value of r leads to earing as the anisotropy becomes significant. As a result, the material easily elongates in certain circumferential directions, leading to the formation of ears on the cup. The random texture is preferred to improve drawability. Y shear texture, characterised by major rotated Cb {001} <11C0> and minor E {111} <110> and F {111}

<112> components, is also needed to enhance the formability and drawability of the material during deformation.

2.9. Texture development during processing of can body sheet (CBS)

Texture and microstructure changes at every step of the production process of AA3104 can body stock sheet material. A schematic of the production process is illustrated in Figure 1. The formation of an optimal texture with minimal acceptable earing at the final gauge heavily relies on the strength of the Cb texture that forms during hot rolling and the extent of subsequent cold rolling [4]. Studies [4], [30] have shown that fully recrystallised grains after hot rolling lead to the formation of Cb-oriented grains, which balances the rolling texture on the final gauge; as a result, acceptable ears can be formed during drawing. The graph in Figure 9 indicates the changes in earing during cold rolling with three different starting structures of AA3104 material, namely, fully recrystallised, partially recrystallised, and un-recrystallised. Therefore, monitoring the hot deformation process to control texture and minimise earing is particularly important.

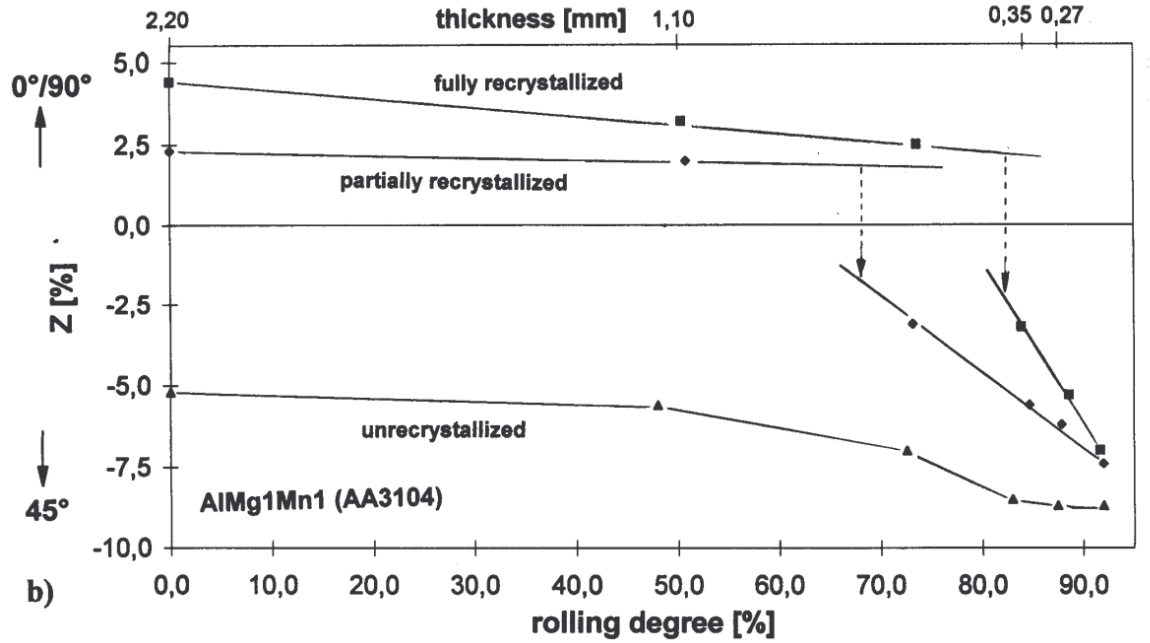

Figure 9 Effect of cold rolling on % earing [15]

In hot rolling, ingots pass through two sets of rollers, a roughing mill and a multi-stand finishing mill, as shown in Figure 1 for a single stand reversing mill. During rough rolling, the ingots are repeatedly rolled back and forth to reduce the thickness of the ingot so that they

can be accepted in the finishing mill. During finish rolling on a single stand reversing mill, the strip is also repeatedly rolled back and forth and coiled on either end owing to the length of the strip at this point. The alternating cycles of deformation, recovery and recrystallisation following hot rolling strongly affect the entire microstructure and texture evolution process [21]. This process results in rolling texture and recrystallisation where rolling texture consists of β-fibre textures containing Cu {112} <111>, S {123} <634> and Bs {011} <211> while recrystallisation texture consists of Cb {001} <100>, Gs {110} <001>, and P {011} <122>. The texture that forms in aluminium alloys includes Bs, S, Cu, Cb, rotated-Cube (r-cube), {111}, and Gs components. Figure 10 shows the Euler space for the orientation positions of these textures. Bs, S and Cu textures are common rolling orientations which form at the centre layer of the metal strip, and due to the high dislocation density formed during deformation, these textures become unstable during annealing. However, studies show that recrystallisation texture consists of Cb, Gs, and random texture [5]. Many parameters must be controlled during hot finish rolling because they determine the texture and microstructure evolution, thereby determining the properties of the final gauge sheet and earing level of beverage cans [15], [21].

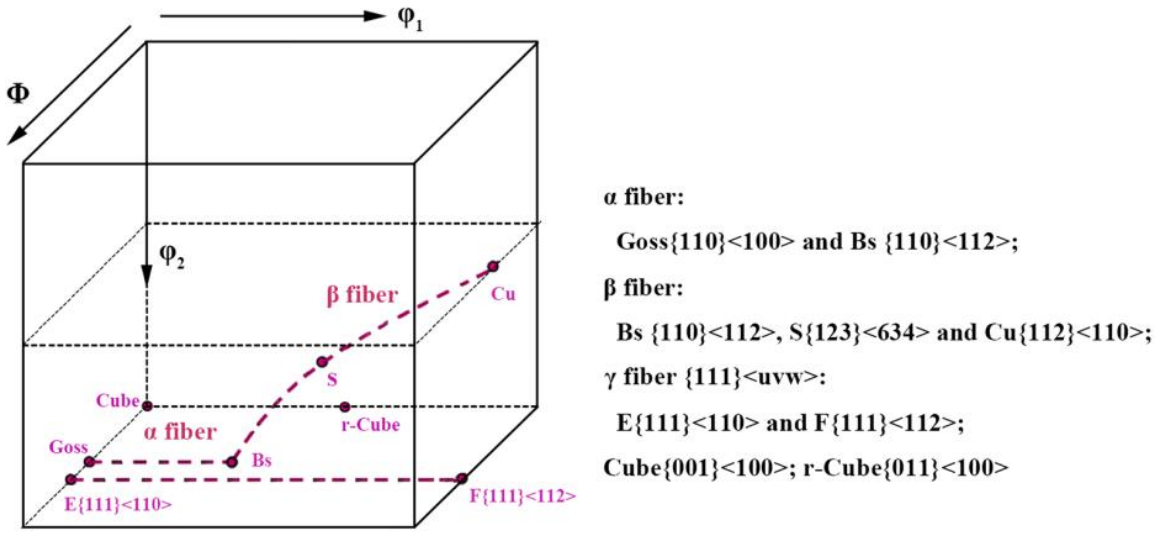

Figure 10 Orientation positions for possible textures [8]

2.10. Factors that affect the evolution of texture during hot rolling

The evolution of microstructure and texture during hot rolling is affected by the recrystallisation processes involved, which, in turn, depend on deformation temperature, strain rate, strain, and the amount of recovery and recrystallisation during the inter-stand pause times [4], [15], [21]. Furthermore, the recrystallised texture depends on the distribution of dispersoids, the amount of solute in solid solution, and hot rolling conditions [15], [21]. These hot rolling parameters and their effects on recrystallisation and Cb texture formation are shown in Table *4*. Increasing total rolling strain in the hot finishing mill leads to an increased volume fraction of Cb texture after hot rolling and recrystallisation anneal. High strain rate and strain will encourage recrystallisation between stands. However, the microstructure of AA3104 after homogenisation, principally based on the effect of the dispersoids and associated dislocation interactions, results in relatively slow recrystallisation kinetics. This is why recrystallisation does not occur between the stands of a tandem hot finishing mill [4], [37], [38].

Table 4 Hot rolling parameters and their effects on the recrystallisation and Cb texture formation *[15]*

Process parameter	**rolling temperature [T_{hr}]**	**Strain , strain rate [φ, dφ /dt]**	**time between passes [t_p]**
Effect on microstructure and properties	high temperature **T_{hr}** supports recovery and recrystallization	high **φ** and **dφ /dt** accelerates recrystallization	long **t_p** allows more recrystallization
Positive Effects :	**T_{hr} enhances recovery** reduces deformation stresses **T_{hr} induces recrystallization** -> transforms coarse as-cast structure into a finer grain size with strong cube texture **self-annealing** produces recrystallized microstructure with strong cube texture (avoids hot band annealing)	fewer / faster rolling passes = reduced **process time** hot band heating = raised **temperatures** and reduced losses enhanced structure transformation by **recrystallization**	**t_p enhances recovery** reduces deformation stresses
Negative Effects :	**reduced cube texture strength** by frequent recrystallization in-between rolling passes, may cause unbalanced earing behaviour of finish gauge sheet product	**Reduced recovery** = higher deformation stresses Temperature raise enhances **interpass recrystallization** = low cube strength	enhanced **inter-pass recrystallization** = low cube strength

2.10.1. Temperature

During hot rolling at temperatures above 500°C, a new recrystallized grain structure forms, with all particles aligned and evenly distributed [15]. Complete recrystallisation occurs after hot rolling in the coil at temperatures above 330°C. However, it is further promoted by heavy hot deformation, as the grains elongated by subsequent hot rolling can readily grow into the surrounding deformed matrix during the final recrystallisation process. This is facilitated by their preferred nucleation and growth behaviour [39] whereby the competing mechanisms of oriented nucleation, such as Cb bands vs PSN (particle-stimulated nucleation) and oriented growth, contribute to the development of recrystallisation texture.

According to a study by Maurice and Driver [6], the intensities of hot rolling textures, namely copper, s, and Bs, increase with an increase in temperature and a decrease in strain rate. They further explained that this is attributed to the enhancement of dynamic recovery, which

makes deformation more homogeneous. To be more specific, Xia et al. [5] explained that the Bs component increases more than s and copper components at high temperatures while s and copper components increase more at higher rolling reductions, and this was attributed to the activation of non-octahedral slip systems at high temperature [7]. At elevated temperatures, dislocations may cross slip from octahedral slip systems {111} <110> to non-octahedral slip systems; {100}, {110}, and {112} <110> [40]. Activation of non-octahedral slip systems depends on the factor α which is defined by the ratio of Critical Resolved Shear Stresses of non-octahedral slip systems and octahedral slip systems, as shown in Equation 4. Table *5* summarises possible non-octahedral slip systems that can be activated and the related texture components that can develop during hot finish rolling of FCC metals as explained by Bracroix and Jonas [40].

$$\alpha = \tau_c^n / \tau_c^{(111)} \qquad \textit{Equation 4}$$

Bracroix and Jonas [40] further explained that CRSS are not constant, even if {111} <110> slips are only active slip systems at the beginning of the deformation, differential hardening of different systems can activate themselves, and this is explained by latent hardening law. Activation of all the slip systems leads to the development of all the texture components during deformation, and their relative amount depends on the value of the critical resolved shear stress.

Table 5 Types of activated cross-slip system and texture.

Cross-slip systems	**α≤**	**Texture components**
{100} <110>	$\sqrt{3}$	Strong S
{110} <110>	$\sqrt{3/2}$	Strong Copper (Cu)
{112} <110>	$\sqrt{2}$	Strong Brass (Bs)

Panchanadeeswaran et al. [41] also studied the effect of temperature on the evolution of texture and found an increase in rolling texture at elevated temperatures. He further explained that the evolution of texture depends on the initial texture of the material before

rolling. It was observed that material with a random initial texture evolves into a dominant copper texture, diminishing other rolling texture components. In contrast, material with a strong initial Cb texture tends to develop a prominent Bs component during plane strain deformation, while the intensity near the copper position remains relatively weak. However, the study by Hirsch [42], found that increasing hot band exit temperatures led to a decrease in rolling texture (from 54% to 6%) and an increase in Cb texture (from 16% to a maximum of 35%), along with a rise in random orientations (from 30% to 59%), due to the increasing amounts of recrystallisation and the recrystallised structure with equiaxed grains was formed [21]. On the other hand, decreasing exit temperatures lead to a high increase in rolling textures with a partially recrystallised microstructure with a weak Cb texture [42].

2.10.2. Strain per pass (rolling reductions)

Rolling reductions or strain per pass also affect the evolution of texture during hot rolling. In high-temperature deformation, straining causes the simultaneous work hardening and softening of the material through dynamic recovery. Large deformations lead to an increase in dislocation density and strain accumulation, which is important for the nucleation of new grains. Low strain rates are associated with the occurrence of recrystallisation through the bulging of pre-existing grain boundaries by the strain-induced boundary migration (SIBM) mechanism. Whereas at higher strain rates, recrystallisation may occur by the growth of sub-grains to form a high-angle grain boundary (> 15) through annihilation of dislocations when they bump into each other on new slip systems [43]. Even though, on average, as strain per pass increases, a corresponding increase in the rolling textures is also seen, Xia et al. [5] have found that strong Bs texture develops even at lower reductions (74%) while S and Cu components show lower intensities at the same reduction but show higher intensities at higher reductions (90%).

However, Bs development only occurred at high temperatures (>420^{o}C), and it could not develop at lower temperatures even at high rolling reductions. This was attributed to the activation of the octahedral slip system at high temperatures. Furthermore, he explained that, at lower reductions, α-fibre texture containing Gs, P, and Bs occur at very low intensities and grow towards β-fibre texture at high reductions with increased densities [5], [41]. The development of texture also depends on the initial texture of the material before deformation. The material with an initially random texture evolves into a strong copper

texture, reducing the presence of other rolling texture components. In contrast, the material with a strong initial Cb texture tends to form a prominent Bs component during plane strain deformation, with weak intensities of copper and S components [41]. Liu et al. [7] demonstrated that volume fractions of the Cb, r-cube, and r-Gs components decreased with increasing hot rolling true strain while the volume fraction of the β-fibre component increased more specifically between S and Bs components on AA5xxx series.

2.10.3. Second-phase particles

Literature shows that the presence of second phase intermetallic particles in aluminium alloys affects recrystallisation hence, microstructure and texture [41], [42], [43]. Li et al. [8] explained that second-phase particles change the way dislocations move around themselves, and the dislocations' motion further determines lattice rotation. Studies [47], [48] further explained that coarser particles (> 5 μm) may act as particle-stimulated nucleation (PSN), which promotes recrystallisation as they act as nucleation sites, thereby enhancing the development of random texture. On the other hand, small, closely spaced dispersoids can retard (Zener pinning) both low and high-angle grain boundary motion. This difference will influence the subsequent recrystallisation annealing, as the zener pinning pressure due to the small particles will retard the nucleation of recrystallisation, while the largest particles will act as nucleation sites for recrystallisation.

Hu et al. [49] studied dispersoid formation and recrystallisation behaviour on the AA6xxx series, and they concluded that small dispersoid particles lead to a more homogeneous distribution of dislocations, resulting in a reduced number of nucleation sites for recrystallisation, thus promoting the development of Cb texture during subsequent annealing. Moreover, the small inter-particle spacing because of the small size and the high number of dispersoids leads to difficulties during the re-arrangement of the sub-grains due to dispersoid particles' pinning. Resultantly, both the nucleation and growth of recrystallised grains were retarded. Yu et al. [47] also found that a high amount of silicon leads to the precipitation of coherent dispersoids, which contribute towards strengthening the retarding force on grain/sub-grain growth, resulting in reduced recrystallisation, hence reducing recrystallisation texture and increased rolling texture during hot deformation. However, large dispersoids lead to a heterogeneous distribution of high dislocation density during

deformation, which acts as preferential sites for nucleation, and there is no pinning, hence an increase in nucleation and growth of recrystallised grains [49].

2.10.4. Inter-pass time

Inter-pass time refers to the time duration between consecutive passes of the metal through the rolling mill. During hot finish rolling, especially on the single stand reversing mill, the sheet of metal experiences inter-pass time from which the static recovery and/or recrystallisation may happen. During high-temperature deformation, the unstable microstructure undergoes both work hardening and softening during straining and softens further during unloading between passes [50]. This softening affects the forming load of each pass, texture, and microstructure evolution in the multi-pass PSC process, and the peak stress of the next pass decreases with the increasing inter-pass time [51]. Softening during unloading between passes depends on the extent and relative proportion of static recovery and recrystallisation. The extent of these processes also depends on the inter-pass time.

In high stacking fault energy materials like aluminium, the dislocation climb is rapid, hence rapid recovery occurs. At the same deformation temperature and strain rate, shorter inter-pass times mean relatively little recovery, while the long inter-pass, the opposite is true. During static recovery, the stored energy of deformed materials is lowered by the annihilation and rearrangement of dislocations, both of which are favourable to the formation of Bs texture components [8]. Furthermore, Bs texture also increases during recrystallisation due to strain-induced boundary migration. This is explained by Vatne et al. [52] that the Bs texture component has lower stored energy than average while the S component has higher stored energy than average; therefore, the Bs component has higher resistance to recrystallisation while the S and Cu components become unstable during recrystallisation.

2.11. Evolution of cube texture

Studies have shown that the development of texture has been explained in terms of nucleation and growth of oriented grains and that originally oriented grains that have been deformed can return to Cb-oriented during recrystallisation. In 2001, Kashyap explained that Beck and Hu (1966) and Lucke (1984) supported that the misorientation of the S-component of the deformation texture {123} <634> turns into a Cb component of the recrystallisation texture when oriented 40° about a common rotation axis (111) [53]. However, he argued that

is not true, but the Cb texture component of recrystallisation texture can grow from misorientation of the R-component (124) [211] of deformation texture when it is oriented at 40° about a common rotation axis (111). R-texture {124} <211> is one of the minor recrystallisation textures, and it is defined as retained rolling textures [54]. Other studies [55] show that nucleation of Cb grains is promoted by S deformed grains, and only after a substantial growth of Cb grains and reduction of S grains does recrystallisation in Bs grains proceed.

On the other hand, Chakraborty et al. [48] proved that the Cb-oriented grains are not restricted to ND-oriented Cb grains; rather, other orientated grains can also develop Cb-oriented grains. From their studies, they found that grains which range within 10 - 20^{o} from ideal Cb orientations may develop Cb orientation at early stages of deformation but rotated away with increasing deformation, while those that are at higher angles may develop Cb components at high deformation [48]. In 2005, Lee [56] explained some of the results that showed that Cb texture originates from copper texture. He further explained that the energy stored in deformed crystals is proportional to the Taylor factor, and it was found that copper orientation has a higher Taylor factor compared to other rolling textures. Since recrystallisation occurs first in high-strain energy regions, and copper orientation has a higher Taylor factor compared to other rolling textures hence Cb texture is likely to form from the copper-oriented grains.

It was also found [57] that coincidence lattice site (CSL) boundaries play an important role in the development of certain textures. Coincidence lattice site boundaries are types of boundaries where atoms on one crystal unit overlap with atoms on another crystal unit structure. In aluminium and its alloys, it is reported that CSL boundaries have higher mobility, leading to higher driving pressure for nucleation and growth of Cb texture. Sigma7 (∑7), a type of CLS boundary, led to the growth of the S component into the Cb component, and Sigma 9 (∑9) grew from the Bs component into the Gs component. However, PSN competitively nucleates with CSL boundaries, destroying the formation of Sigma 9 and 5 boundaries, hence reducing Cb texture development. Cube texture development can be facilitated by increasing the grain boundary between Cb and S texture and Cb and Cb and Bs texture, which form during deformation.

3. Methodology

3.1. Overview

In this chapter, the experimental procedure will be explained. This will include collection of the samples, preparation of samples (cleaning, taking dimension readings), simulation of hot rolling process using Gleeble 3800, metallographic preparation of specimens, and techniques that will be used for data analysis. During the hot finish rolling process on a single stand reversible mill, the metal strip experiences different inter-pass times because the leading end (LE) and tailing end (TE) interchange places during the deformation process. For this project, LE and TE are termed Positions A and B, respectively. Positions A and B are the final positions after the last hot rolling pass, just before cold rolling. Figure 11 shows a schematic diagram of how Position A and B interchange the positions during rolling, and it also indicates the final positions before cold rolling.

During the interpass time, recovery and/or recrystallisation take place, and the extent thereof depends on the length of the interpass time. Longer times allow for more extensive annealing and a resulting decrease in total strain accumulation. Therefore, position A and position B will exhibit different properties and texture distributions, representing the variability at the opposite ends of the metal strip. This work aims to investigate the effect that minor changes in the time between successive passes during the hot rolling process will have on the final texture of the material and, hence, earing. Literature shows that the texture and microstructure evolution is affected by processing factors such as temperature, strain, strain rate, microstructural features, and inter-pass time during the hot finishing rolling process.

This chapter will explain how plane compression tests and data analyses were conducted to determine how inter-pass time affects the texture evolution on the edges of the metal strip. The control of texture is not easy in a hot rolling process because dynamic recovery and deformation happen concurrently.

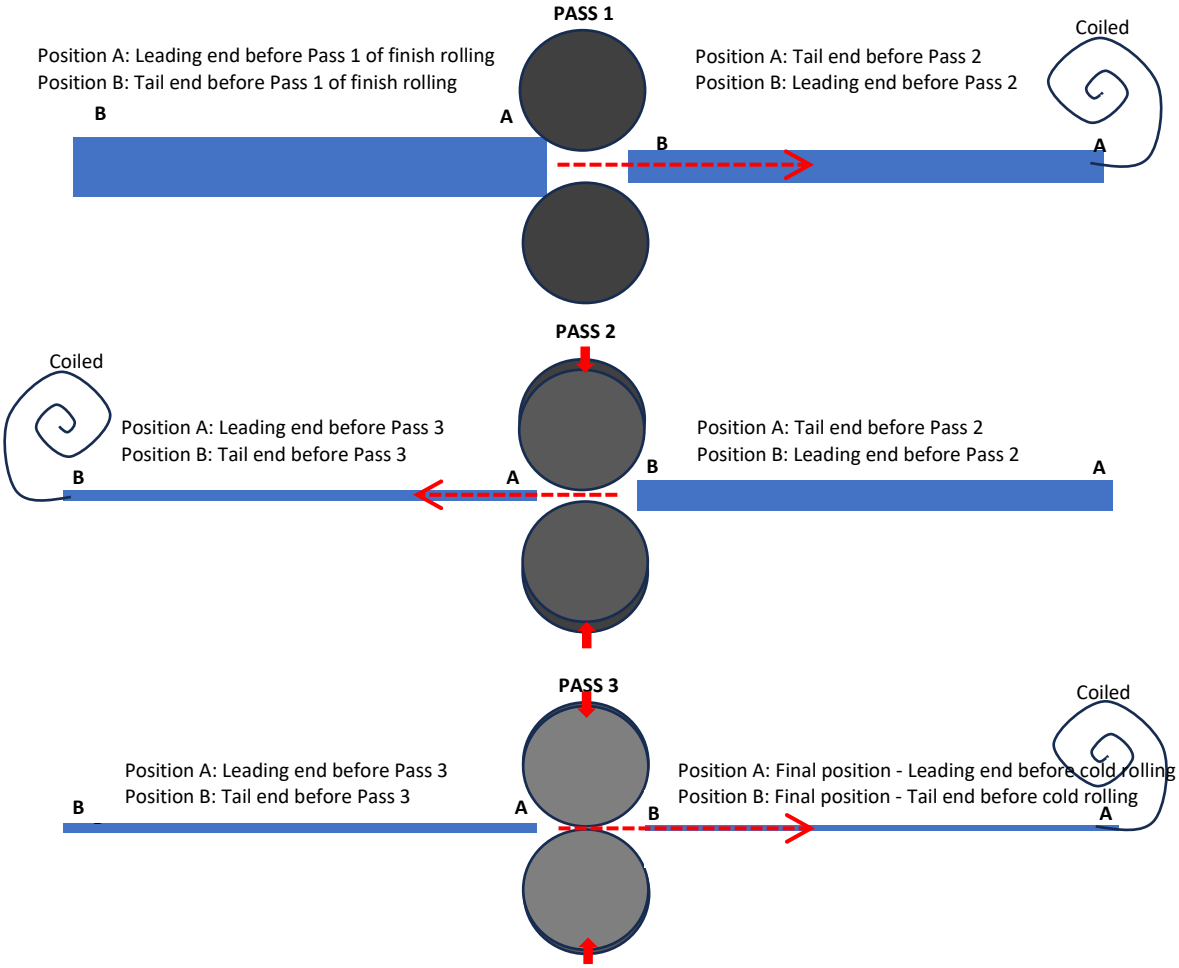

Figure 11 Schematic diagram of how Positions A and B interchange the places during hot finish rolling

The plane strain compression tests were conducted on the AA3104 transfer bar samples to simulate hot finish rolling processing using Gleeble 3800. The deformation processes were conducted at different temperatures, strain rates, and strain per pass for each pass. The deformed samples were quenched and then annealed to allow recrystallisation to occur, and microstructural and texture analyses were performed on the samples representing positions A and B using POM and EBSD. Texture distribution, grain characterisation, morphological exploration, strain accumulation, and the existence of special boundaries were analysed using ATEX software. The hardness test was also conducted on the deformed samples to determine the softening fraction during interpass time.

3.2. Material preparation

AA3104 transfer bar at 23 mm gauge from the hot roughing mill was supplied by Hulamin Rolled Products in Pietermaritzburg, South Africa. The specimens representing positions A and B were extracted from transfer bar material in the as hot, rough rolled condition. The transfer bar was machined into blocks of metals of sizes 12 x 20 x 30 mm, followed by labelling using a laser engraving machine, as shown in Figure 12. Each sample was issued a unique ID number that was engraved on it, together with its location from the transfer bar and positions where thermocouples 1 and 2 will be placed in the Gleeble PSC testing.

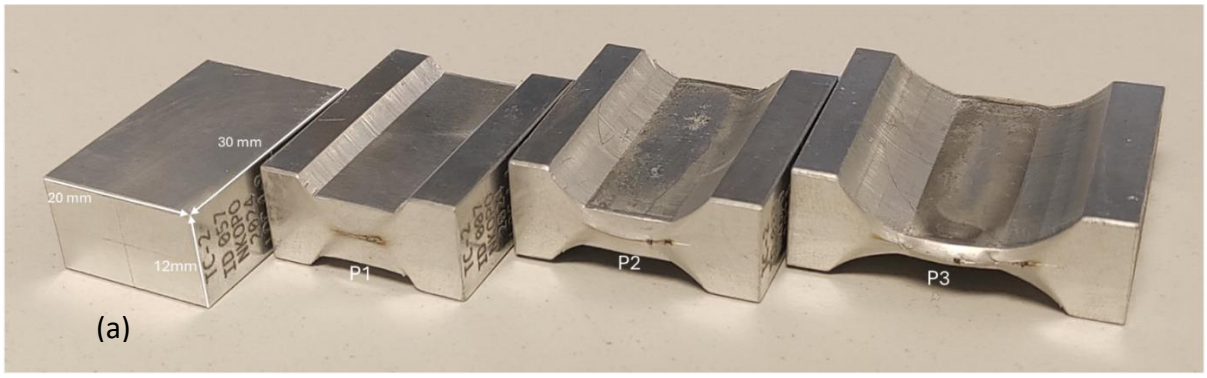

Figure 12 Samples used for PSC tests (a) before deformation (P1, P2, and P3) after deformation pass 1,2 and 3, respectively.

3.3. Simulation of the hot finish rolling process on the Gleeble

Table *6* shows the processing matrix used to acquire the deformation data.

Table 6: Processing matrix

Position A				Position B			
Passes	**Deformation Temp (°C)**	**Inter-pass time (s)**	**Strain rate (/s)**	**Passes**	**Deformation Temp (°C)**	**Inter-pass time (s)**	**Strain rate (/s)**
P1	360	-	30	P1	360	-	30
P1 + t_1	360	395	30	P1 + t_1	360	40	30
P1+ t_1 +P2	330	-	50	P1+ t_1+P2	330	-	50
P1+ t_1+P2+t_2	330	20	50	P1+ t_1+P2+ t_2	330	539	50
P1+ t_1+P2+ t_2+P3	300	-	100	P1+ t_1+P2+ t_2+P3	300	-	100

Multi-pass, high-temperature plane strain compression (PSC) tests were conducted on a Gleeble 3800 to simulate the hot finish rolling process with variable inter-pass times between deformation events. Two scenarios were investigated. The first scenario is termed “Position

A", where the material experiences a long inter-pass time between deformation pass one (P1) and pass two (P2), this inter-pass time is referred to as t_1, and a shorter inter-pass time before deformation pass three (P3), referred to as t_2. The second scenario is termed "Position B," which experiences a short inter-pass t_1 and a longer inter-pass t_2. Figure 11 shows a schematic diagram of deformation events as Positions A and B interchanged the placing, thereby imposing different interpass times between the two positions. A summary of the simulated process parameters is shown in Table *6*.

A temperature–time plan for the multi-pass rolling simulation using plane strain compression (PSC) testing on the Gleeble was developed and is illustrated in Figure 13. All samples were initially heated to 360°C and held for 90 seconds to eliminate thermal gradients, as illustrated in Figure 13. To investigate the effect of the inter-pass time variability, samples were compressed according to the full three-pass deformation simulation in the Gleeble and were quenched at critical points in the cycle (as laid out in Table *6*). After the Gleeble testing was complete, certain samples were then exposed to a recrystallisation anneal heat treatment (1 hour at 365°C for recrystallisation) before microstructural characterisation using Scanning Electron Microscopy (SEM) and Electron Backscatter Diffraction (EBSD) in a Tescan Mira3. The EBSD maps were then analysed to interrogate and characterise the microstructural features, such as grain size and grain boundary statistics, and the crystallographic texture in Position A and Position B at all critical steps throughout the full rolling sequence.

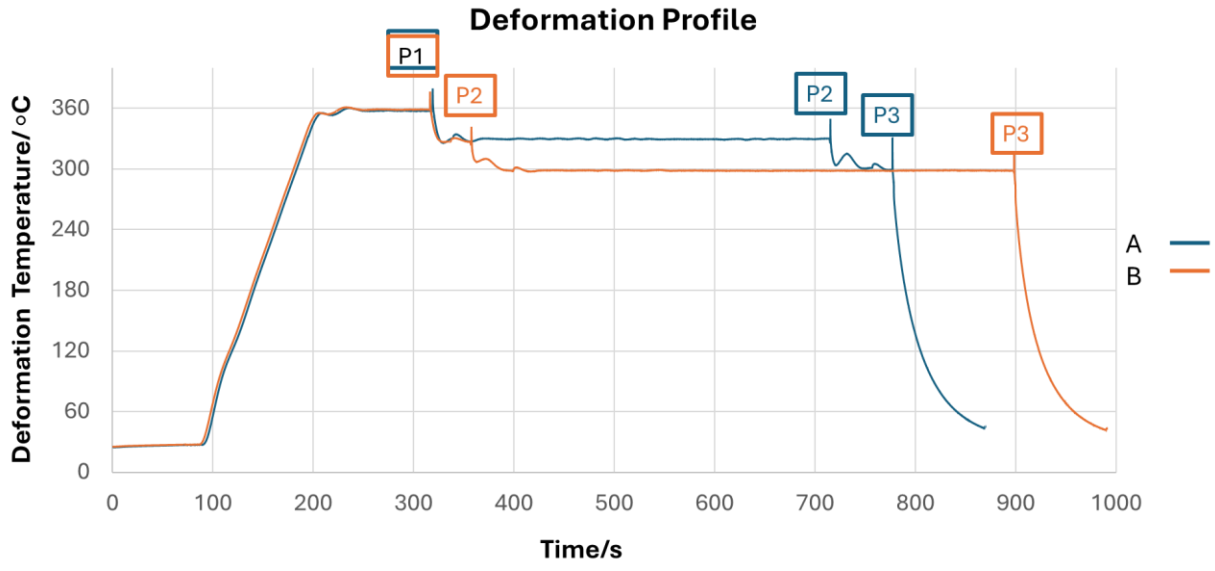

Figure 13 The illustration of the multi-pass hot-rolling schedule of Positions A and B.

3.4. Metallographic preparation of the samples

Two different microscopy techniques utilised were Polarized optical (POM) and SEM-EBSD microscopy. Both recrystallised and deformed specimens were cut, as shown in Figure 14 and then mounted. They were hot-mounted using a Struers labopress-3 hot mounter for 14 minutes at 25KN force. Thereafter, the specimens were ground and polished for microscopic analysis as per Table 7. Steps II to IV were repeated if there were still deep visible scratches on the surface after the last step. The first step was manually done and then step II-IV was automated using a Struers Tegramina-25 grinding and polishing machine. After the last step, the specimens were washed with warm, soapy water using cotton wool to ensure thorough removal of OP-suspension on the polished surface. The samples were rinsed further with 99.9% ethanol grade and dried using a blow dryer. For EBSD analysis, the mirror-finished samples were unmounted after the last step of polishing and placed on the stabs for ion polishing.

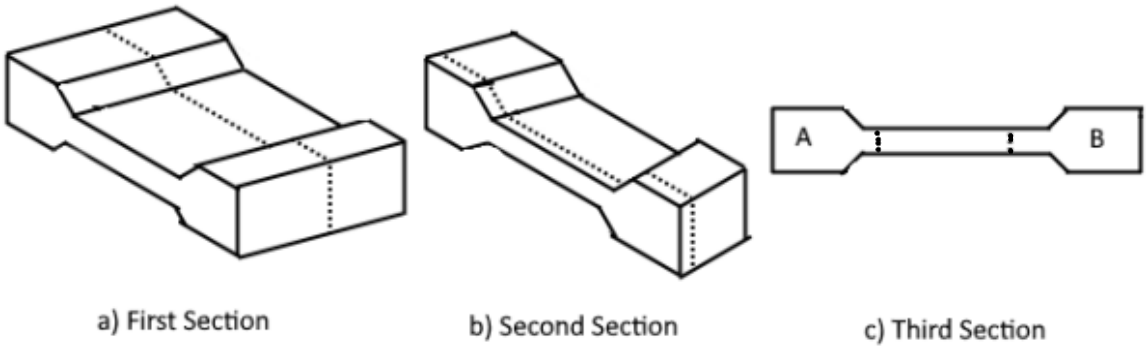

Figure 14: Illustration of the three-step sectioning of plane compressed samples for microstructural analysis, A and B were also cut out.

Table 7: AA3104 Metallographic sample preparation procedures

Sic paper/Polishing pad	Suspension	Force (N)	Time(minutes)	Speed (rpm)
I. 1200 grit paper	water	-	1	300
II. MD Mol cloth	DiaDuo-2 (3μm)	10/15	6 - 8	150
III. MD chem cloth	OP-S	10	1 - 4	150
IV. MD chem cloth	Soapy water	5	1 - 2	150

3.4.1. Microscopic analysis using POM.

To analyse the grain structure using polarised optical microscopy (POM), the mirror finish polished samples were anodised with Barker's reagent (a mixture of 7 ml tetra-hydro fluoroboric acid and 93 ml distilled water). The specimens were anodised for 30-60s at room temperature, using 20-25V voltage. This was used to assess the effects of hot rolling parameters on the microstructure evolution of both Positions A and B samples.

3.4.2. Microscopic analysis using EBSD.

EBSD texture measurements were done on the perfectly polished surface specimens, polished further by ion polisher Leica EM TIC3X for 20-60 minutes at 5kV and 2mA. EBSD texture maps were constructed from the Tescan Mira3 machine using 15 keV and 12V-14V beam intensity. Small and large area mapping were constructed and acquired using AztecHKL acquisition software at the step size of 0.2-0.5 µm for a small map area and 1µm for a large map area and at up to 48.5ms exposure time per pixel. A minimum of seven out of ten Kikuchi bands were used to index the pattern during data collection to ensure good, reliable results, and a minimum of 1000 grains were scanned to ensure a statistically reliable representation of grain orientations. The samples were tilted at a 70º angle to the horizontal, optimising electron diffraction towards the detector.

Orientation distribution functions (ODFs) and (111), (100), and (112) pole figures were obtained using analysis tools for electron and x-ray diffraction (ATEX) software [58] by considering orthorhombic sample symmetry and cubic crystal symmetry and using the harmonic series expansion method (L = 22)/boxing + c-coefficients method and a Gaussian half width of 5°. ODFs where φ_2= 0°,45°,65° were calculated and drawn. AztecCrystal was also employed for EBSD analysis. This work focuses on the following deformation texture components: Bs {110} <112>, Cu {112} <111>, (S3) {123} <634>, and Taylor (Ty) {4 4 11} <11 11 8>; S3 texture component is the same as S with orientation {123} <634>, the ATEX software uses S3 instead of S, and (2) recrystallisation texture components such as Cb {001} <100>, Gs {110} <001>), (P) {011} <122>), Q {013} <231>. R texture component is a retained rolling texture found after recrystallisation [54], and it has the orientation {124} <211>. S3 texture component is the same as S with orientation {123} <634>, the ATEX software uses S3 instead of S. A grain is considered part of a specific texture component if its

orientation falls within a 15° deviation from the ideal component when determining the fractions of these texture components.

3.5. Hardness test

The extent of softening during deformation and inter-pass time was studied through the Vickers hardness test at room temperature. Hardness measurements were conducted using a three kgf load with a dwelling time of 10s, and the average hardness from six to seven independent measurements was collected.

3.6. Flow stress

To evaluate how interpass time affects flow stress during subsequent deformation passes, stress and strain data obtained from the Gleeble were analysed using Paramaterial [59], a Python package for parameterising materials test data. Four samples at each critical step (as tabulated in Table *6*) were tested, that is, at P1, 4 samples were tested representing position A and 4 samples representing position B, then 4 samples at the first interpass time (t_1) for each position. The average strain rates at each point during the deformation passes (or "hits") were calculated, and their graphical representations are shown in Appendix A. Paramaterial first converted the engineering stress-strain data from Gleeble into true stress–true strain data, then applied fitting curves and smoothing algorithms to reduce noise in the dataset. It then calculated the flow stress values at each specified true strain. In this study, the average flow stress values across all deformation passes were computed for both positions A and B, and these were used to analyse the effect of interpass time on the material's flow stress.

4. Results

4.1. Introduction to results

The hot finish rolling simulation for the Positions A and B samples was conducted through plane compression tests using the Gleeble 3800. Appendix A presents the average strain rates experienced during hot rolling for each pass. The scatter plots demonstrated that the nominal average strain rates and temperatures closely matched the set values. The raw data collected from the Gleeble was used to determine the changes in average flow stress for both the Positions A and B samples using paramaterial, a Python package, and flow stress curves were analysed and plotted as shown in Appendix B.

All samples were subjected to the same temperature, strain, and strain rate at each pass, along with a 90-second holding time before the first pass. However, the Positions A and B samples experienced different inter-pass times between passes. Figure 15 shows the temperature-time (T-t) curves for the Positions A and B samples. After the first pass, the position B sample was held for about 40 seconds (t_1) (short inter-pass time) at 360-330°C, while the position A sample was held for about 395 seconds (long inter-pass time) at the same temperature before the next pass. Similarly, after the second pass, the position B sample was held at 330-300°C for about 539 seconds (t_2) (long inter-pass time), while the position A sample was held for only 60 seconds (short inter-pass time) before the final pass.

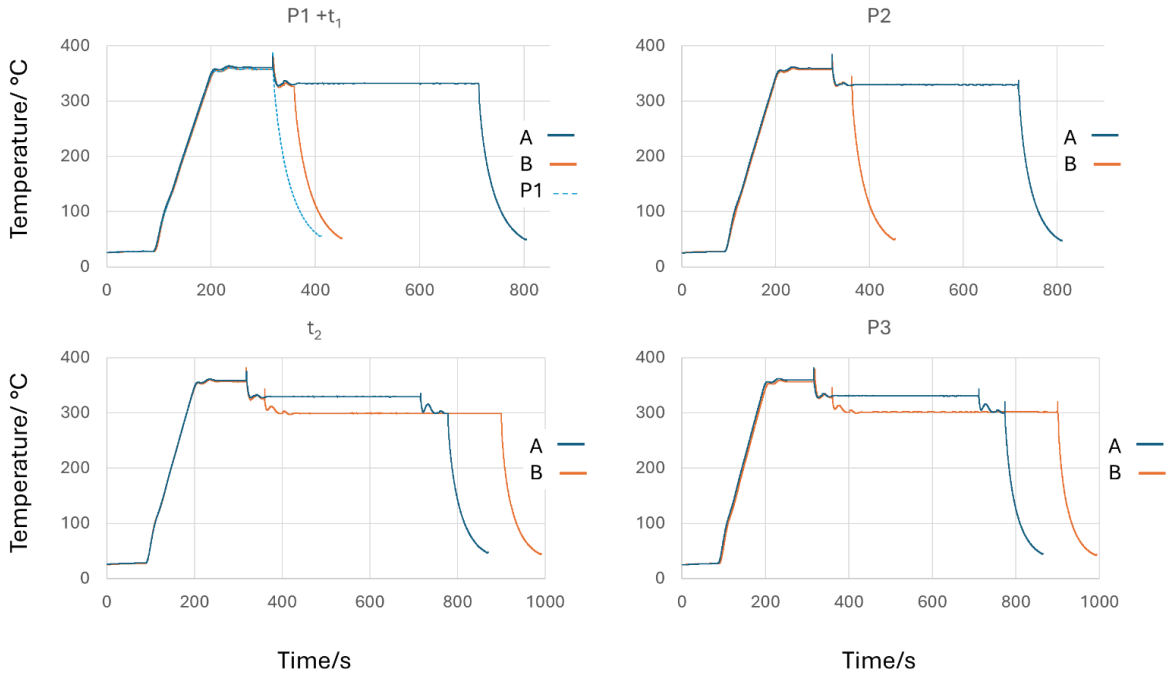

Figure 15 Temperature-time curves of Positions A and B. (a) Pass 1 and Inter-pass time 1 (b) Inter-pass time 2 (c) Pass 2 (d) Pass 3.

During deformation, strain energy accumulates and acts as the driving force for recrystallisation. The amount of accumulated strain energy can be inferred from the extent of recrystallisation after annealing. It can also be measured through hardness testing, as higher strain energy corresponds to higher hardness values. Since the deformation occurred at high temperatures, both deformation and softening processes took place simultaneously. Softening also occurred during the inter-pass times. The degree of softening can be evaluated using true stress vs. true strain data during the inter-pass times, hardness measurements, and optical and electron microscopy after quenching and recrystallisation annealing of the deformed samples. The softening results generated from the experimental data reflect the progress of dynamic and static recovery and/or recrystallisation, which is directly related to the accumulated strain [60]. The effects of softening periods between the passes on the mechanical, microstructural and texture evolution results are also outlined in this chapter.

4.2. Changes in Mechanical Properties during hot rolling

4.2.1. Flow stress

The thermomechanical history of the Positions A and B samples was significantly different, leading to variations in the strain accumulated during deformation. As a result, the mechanical properties, microstructure, and texture evolution also differed. Figure 16 illustrates how the flow stress during the full three-pass sequence for both Positions A and B samples changed, and the results showed that flow stress increased with each pass. This indicates that as the temperature decreased and the strain rate increased, the flow stress also increased.

In Pass 1 (Hit 1), positions A and B were deformed at 360°C with a strain rate of 30/s to a strain of 0.5 and the flow stress was expected to be the same between both positions. However, the flow stresses for positions A and B were found to be 130 and 131 MPa, respectively. The slight difference between the values may be attributed to a small difference in the nominal strain rates experienced, as shown in Appendix A. High strain rates lead to more dislocations entanglements, which result in increased flow stress. Position B had on average higher nominal strain rates than position A, and position A had an outlier.

During deformation, the Zener-Hollomon parameter (Z) influences flow stress, accounting for the combined effect of strain rate and temperature. Higher strain rates and lower deformation temperatures result in higher Z values, which in turn promote higher flow stress. Ghosh et al. [61] studied the microstructure and texture evolution during high-temperature compression of Al-Mg-Si-Zr-Mn alloys and found that flow stress decreases with increasing deformation temperature and decreasing strain rate. They also noted that higher temperatures and lower strain rates encourage dynamic softening by reducing dislocation density, facilitating dislocation movement, and limiting the multiplication of dislocations, leading to fewer dislocation entanglements and the formation of sub grains.

Before the second pass, position B experienced a short inter-pass time and was expected to show higher flow stress than position A during the subsequent rolling. However, the flow stresses for positions A and B were 179 and 181 MPa, respectively. This similarity might be because, since the deformation temperature was high, the deformation and recovery occurred simultaneously; therefore, the level of softening might not have been much to cause

a significant reduction in the flow stress of position A during the next deformation pass. Furthermore, after the first deformation pass, there was no sufficient stored energy to drive significant recrystallisation during the inter-pass time. The difference in the nominal strain rates might have also contributed.

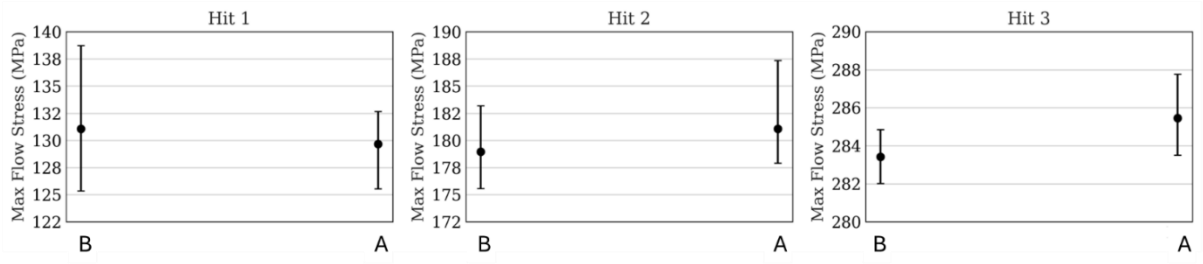

Figure 16 The max flow stress of Positions A and B during hot deformation.

Softening during the inter-pass time occurs through recovery and/or recrystallisation. The longer the inter-pass time, the more the material softens, reducing the amount of strain energy accumulated during deformation. Giordani et al. [50] conducted a similar study on steels, investigating recovery and recrystallisation during inter-pass times at high temperatures in Nb- and N-bearing austenitic stainless-steel biomaterial. They found that fractional softening increased with both time and temperature. They also explained that recovery plays a critical role in softening during the inter-pass time, particularly at lower temperatures, as it occurs before recrystallisation.

During the final pass, position A exhibited higher flow stress than position B. The flow stresses for Positions A and B after P3 were 286 and 283 MPa, respectively. Prior to the final pass, position A experienced a short inter-pass time, while position B had a longer inter-pass time, allowing position B to soften more. As a result, more stored energy was lost in position B, leading to lower flow stress during the final rolling, as seen in Figure 16.

4.2.2. Hardness

Experimentally, the extent of recovery can be measured using a single parameter, such as hardness. Microstructural changes that occur during recovery also influence mechanical properties, so recovery is often assessed by changes in yield stress or hardness. Therefore, hardness tests were conducted on both the Positions A and B samples after each pass and inter-pass time.

The hardness test results aligned with the flow stress plots. Figure 17 shows how the hardness values changed after each pass and inter-pass time. After each inter-pass time, there was a reduction in hardness due to the softening period. Following the first inter-pass time, the hardness value of the position A sample decreased more than that of the position B sample, confirming that longer inter-pass times lead to more softening. Additionally, after the second inter-pass time, position B exhibited a more significant drop in hardness compared to position A, which experienced a short inter-pass time. During this phase, position B experienced a longer inter-pass time, allowing more recovery to occur, which reduced the accumulated strain energy, thus softening the material.

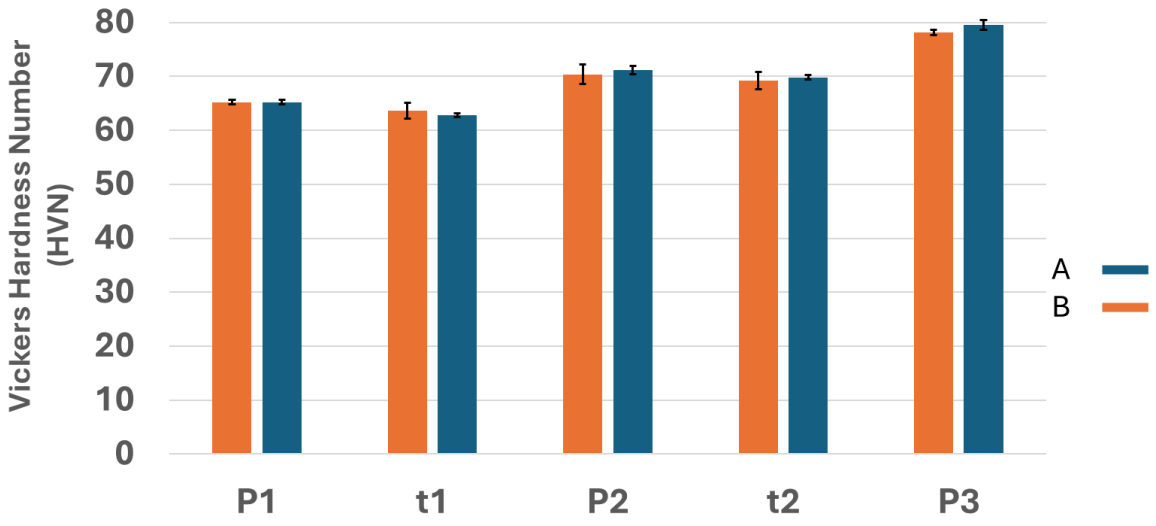

Figure 17 Hardness values of hot rolled samples of Positions A and B

Recovery consists of several stages, including dislocation tangling, cell formation, annihilation of dislocations within cells, sub-grain formation, and sub-grain growth. The extent of recovery depends on how easily recovery and recrystallisation can take place depending on the material and the driving forces available [62]. During recovery, the accumulated strain is reduced through dislocation annihilation and rearrangement, achieved through dislocation glide, climb, and cross-slip. Furthermore, sub grain formation always happens dynamically during the hot deformation of AA3104. Sub grain coarsening further softens the material during interpass time due to static recovery. If conditions are favourable for recrystallisation, recovery may extend to cell formation.

4.3. Microstructure evolution during hot rolling

Recovery and recrystallisation affect the microstructural evolution during inter-pass time and on subsequent deformation passes. Although the flow stress and hardness values between Positions A and B samples showed slight differences between the passes, microscopic analysis revealed significant variations in microstructural and textural features. This section highlights microstructural evolution on both positions during hot rolling.

4.3.1. Initial microstructure

Figure 18 (a) represents the transfer bar microstructure, and (b) hot finish rolled microstructure after the first deformation pass. After hot finish deformation, the second phase particles were reduced in size and were uniformly distributed along the grain boundaries (circled on the micrographs). These are the particles that act as particle nucleation sites (PSN) during recrystallisation because they are coarser, promoting the formation of randomly oriented grains and reducing the formation of other texture components, especially Cb texture. Moreover, the grains became longer and thinner compared to the transfer bar (rough rolled sample), as shown by black arrows on the micrographs. As the transfer bar is rolled back and forth on the reversing mill, the grains decrease in thickness and become pan-caked shape and longer.

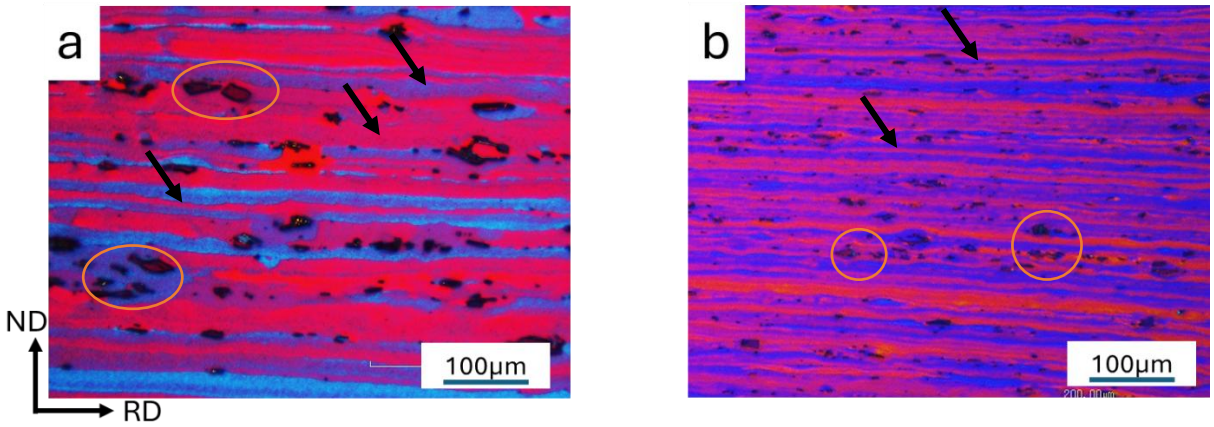

Figure 18 Micrographs of a) transfer bar b) 1st hot finish deformed sample

4.3.2. Light Microscopy Analysis

Figure 19 presents the Polarized Optical Microscopy (POM) images of the hot-rolled and annealed Positions A and B samples after P1 and t_1, with a scale bar representing 100 µm, following electrolytic etching. The POM images revealed various grain structures by emphasising contrast with different colours. The variation in grain colours indicates different crystallographic orientations within the sample. After deformation, the intermetallic particles appear uniform, as shown in Figure 18 (b). Both Positions A and B deformed samples demonstrated elongated grains aligned with the rolling direction in the hot-deformed condition. Deformation bands were observed throughout all samples. No recrystallisation was detected after the first pass (P1) and after the inter-pass time.

Although the temperature was high enough for recrystallisation, the stored energy after P1 might have been insufficient to drive recrystallisation during the inter-pass. Furthermore, aluminium's high stacking fault energy (SFE) encourages deformation through slip, which tends to generate high dislocation densities on active slip planes. As a result, the preferred softening mechanism at high deformation temperatures is dynamic recovery [62]. The high SFE also promotes rapid dislocation climb during high-temperature deformation, leading to substantial recovery [50].

To evaluate the stored energy after deformation and inter-pass time, the samples were recrystallised. A high amount of stored energy is indicated by faster and many tiny, recrystallised grains formed after recrystallisation anneal. After annealing, both Positions A and B samples were partially recrystallised, transforming the elongated bands into a mix of equiaxed and elongated grain structures. Figure 19 shows the POM images of Positions A and B after P1 and t_1, (a) and (b) are images after the first deformation and subsequent recrystallisation for both Positions A and B, respectively, (c) and (d) are for Position A after t_1 as deformed and recrystallised respectively, and (e) and (f) are for Position B after t_1 as deformed and recrystallised respectively.

The sample (a), which was quenched immediately after deformation, recrystallised more than the samples that experienced inter-pass times, as numerous new small grains were formed after recrystallisation, indicating that (a) had more accumulated energy. In contrast, samples (d and f) formed fewer new grains, suggesting that there was less stored energy after the

inter-pass time. However, sample (f) showed more and smaller grains than (d), as seen in Figure 19. The sample (d) displayed fewer, larger grains, implying that few sub-grains might have formed during the longer inter-pass time experienced for this sample. The sub-grains would have coalesced and grown into larger grains during annealing. This confirms that softening during the inter-pass time occurred through recovery, reducing the stored energy available to trigger recrystallisation in the post-processing anneal illustrated in Figure 19 (b), (d) and (f). The extent of softening is time dependent and is qualitatively assed using recrystallised grain size in the annealed state as a metric, where the smaller the grains, the greater the prior stored energy.

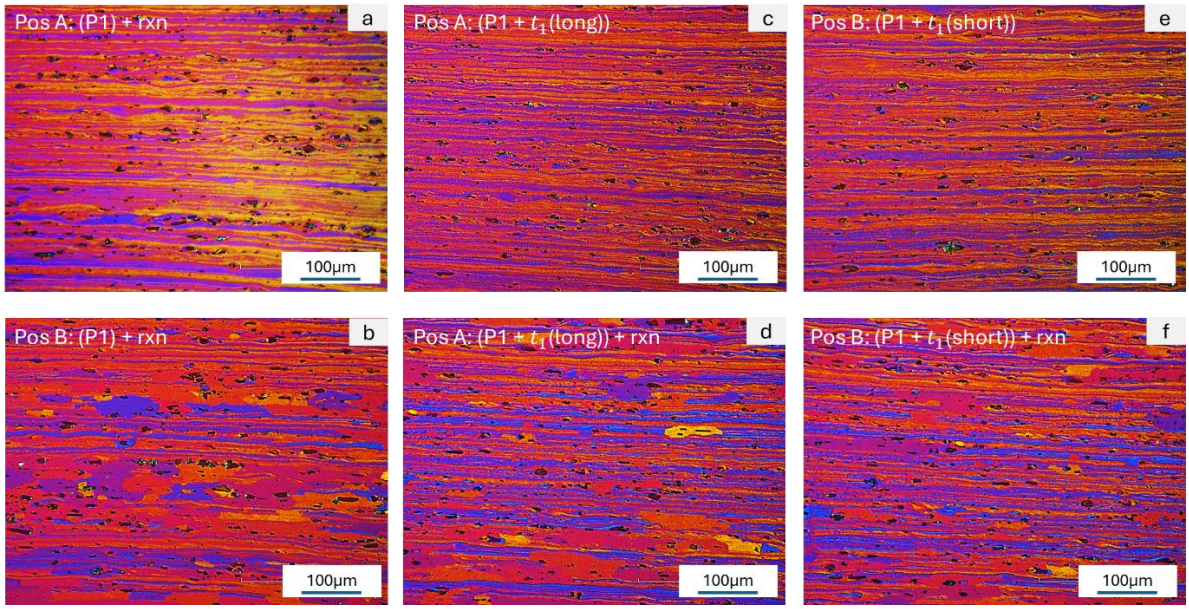

Figure 19 Polarised optical microscopy images to investigate stored energy. Images show (a) Position A with anneal after P1, (b) Position B with anneal after P1, (c) Position A after P1+t_1, (d) Position A with anneal after P1+t_1, (e) Position B after P1+t_1 and (f) Position B with anneal after P1+t_1.

The degree of softening during the inter-pass time is also influenced by the strain energy accumulated during deformation, which is affected by both strain rate and deformation temperature. Lower deformation temperatures and higher strain rates promote greater strain accumulation during deformation. A similar analysis was conducted on samples after P2, t2, and P3, and Figure 20 and 23 show the results obtained. The POM images of hot-rolled positions A and B samples after P2, t_2, and P3 also revealed elongated grains aligned with the rolling direction. Second-phase particles appeared relatively uniform in all samples, and the

micrographs still did not show any new grains formed during interpass time and deformation passes.

To further examine the strain energy differences after P2, t_2, and P3, the samples were annealed at 365°C for 1hr. After P2, both positions A and B showed near-complete recrystallisation, with numerous new grains forming, but Position B showed more and smaller grains than position A. This difference can be attributed to the long inter-pass time that position A experienced before P2, allowing more recovery to occur and reducing more strain energy than in position B, which had a shorter inter-pass time. However, before P3, position B experienced a long inter-pass time, reducing more strain energy, as indicated by the larger recrystallised grain size after t_2 as compared to after P2. During dynamic recovery, dislocations may rearrange to form well-developed sub grain structures, and sub grain formation and growth can continue during the inter-pass time. Upon subsequent annealing, the sub grains formed during the long inter-pass time may coarsen, leading to grain growth while new grains also form.

In contrast, position A experienced a short inter-pass time before P3, resulting in little to no change in grain size between the P2 and t_2 samples, and their grain sizes were comparable. Figure 20 b) and d) show micrographs of the recrystallised samples of position A after P2 and t_2, both of which display comparable grain sizes of newly formed grains. This suggests that although some softening occurred during the short inter-pass time, it was insufficient to significantly reduce the stored energy compared to the long inter-pass time. Figure 21 b) and d) show micrographs of recrystallised samples of Position B after P2 and t_2. Sample (b) was hot-rolled, quenched, and recrystallised, while sample (d) was hot-rolled, held at 330-300°C for 539s, and then recrystallised. Sample (d) exhibited fewer and smaller recrystallised grains and more larger grains compared to sample (b), indicating that during the long inter-pass time, recovery occurred, reducing the stored strain energy necessary for recrystallisation. Moreover, the recovered sub-grains grew during annealing, increasing the grain sizes. After deformation P3 and annealing, both Positions A and B samples were fully recrystallised, with elongated grains completely replaced by new, small equiaxed grains, as shown in Figure 20 (f) and Figure 21 (f) respectively.

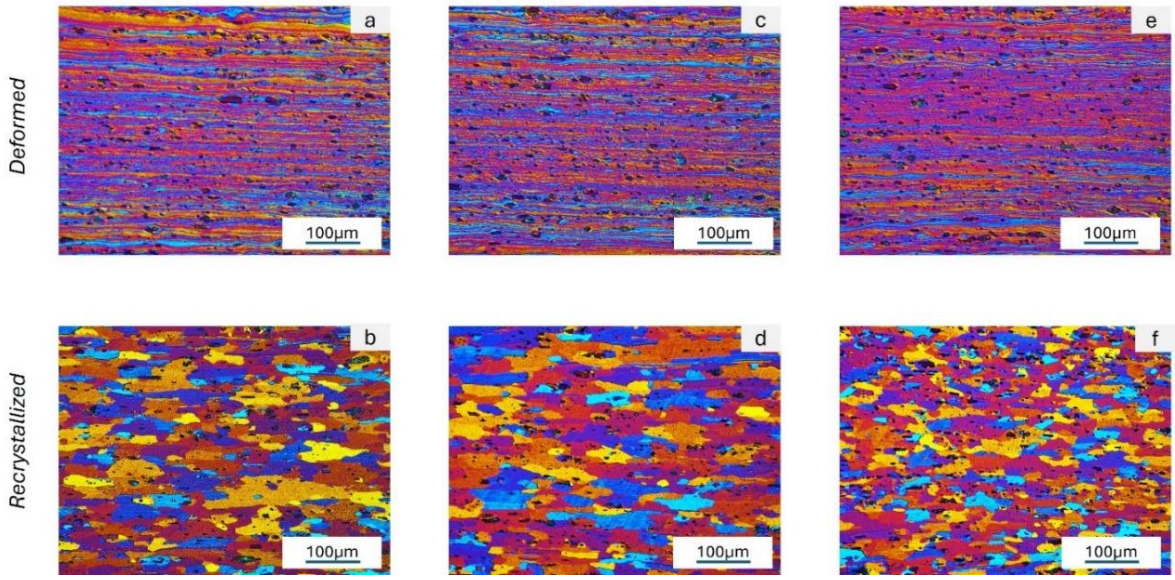

Figure 20 POM images showing (a) Position A after P2, (b) Position A with anneal after P2, (c) Position A after P2 +t_2, (d) Position A with anneal after P2+t_2, (e) Position A after P3 and (f) Position A with anneal after P3.

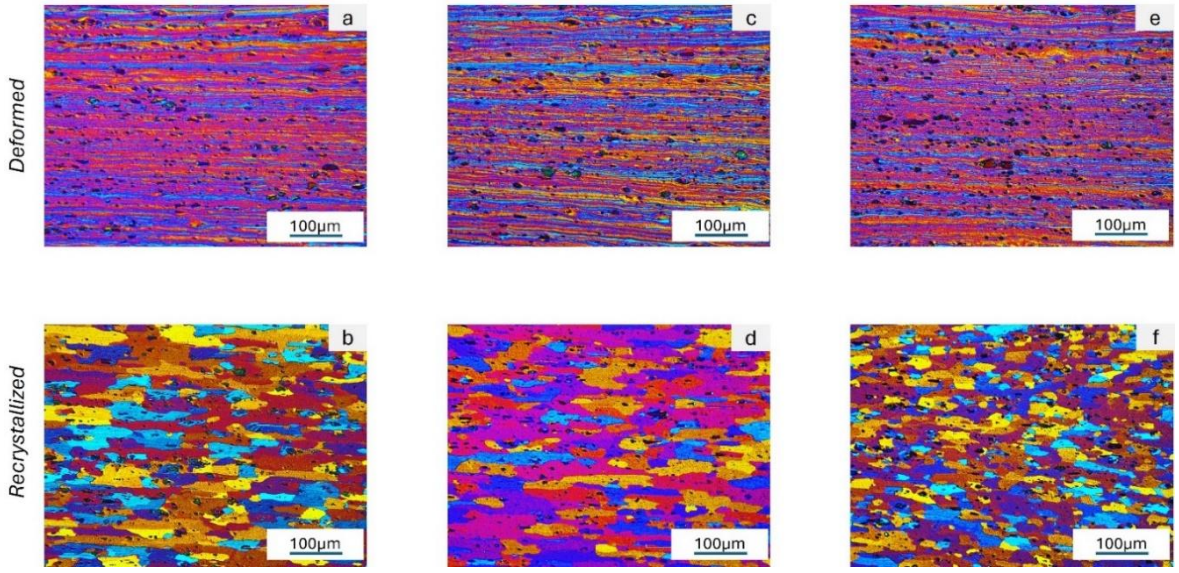

Figure 21 POM images showing (a) Position B after P2, (b) Position B with anneal after P2, (c) Position B after P2 +t_2, (d) Position B with anneal after P2+t_2, (e) Position B after P3 and (f) Position B with anneal after P3.

.

4.3.3. Electron microscopy analysis

In addition to POM analysis, Secondary Electron Microscopy - Electron Backscatter Diffraction (SEM-EBSD) analyses were carried out on the hot-deformed and annealed samples to study the grain structure and grain orientation in more detail. Figure 22 depicts EBSD inverse pole figures (IPF) for Positions A and B deformed and recrystallised samples, which underwent a full 3-Pass sequence, showing grains in different colours based on their orientation. Consistent with the POM images, both Positions A and B samples in the hot-rolled condition show elongated grains in the rolling direction. The deformed microstructure displays a banded structure with numerous un-indexed points, possibly due to the many sub-grain structures formed due to recovery. During hot rolling, recovery and deformation occur simultaneously, allowing a significant amount of deformation in a single pass due to the low work-hardening rate at hot rolling temperatures. Furthermore, there was the formation of many sub grains within elongated grains due to high strain accumulation and recovery at high temperatures during deformation [61]. The EBSD maps of deformed samples are shown in Figure 22 (a) and (b) show many low-angle grain boundaries (LAGB) (2-15° misorientation) depicted by white lines within deformed grains.

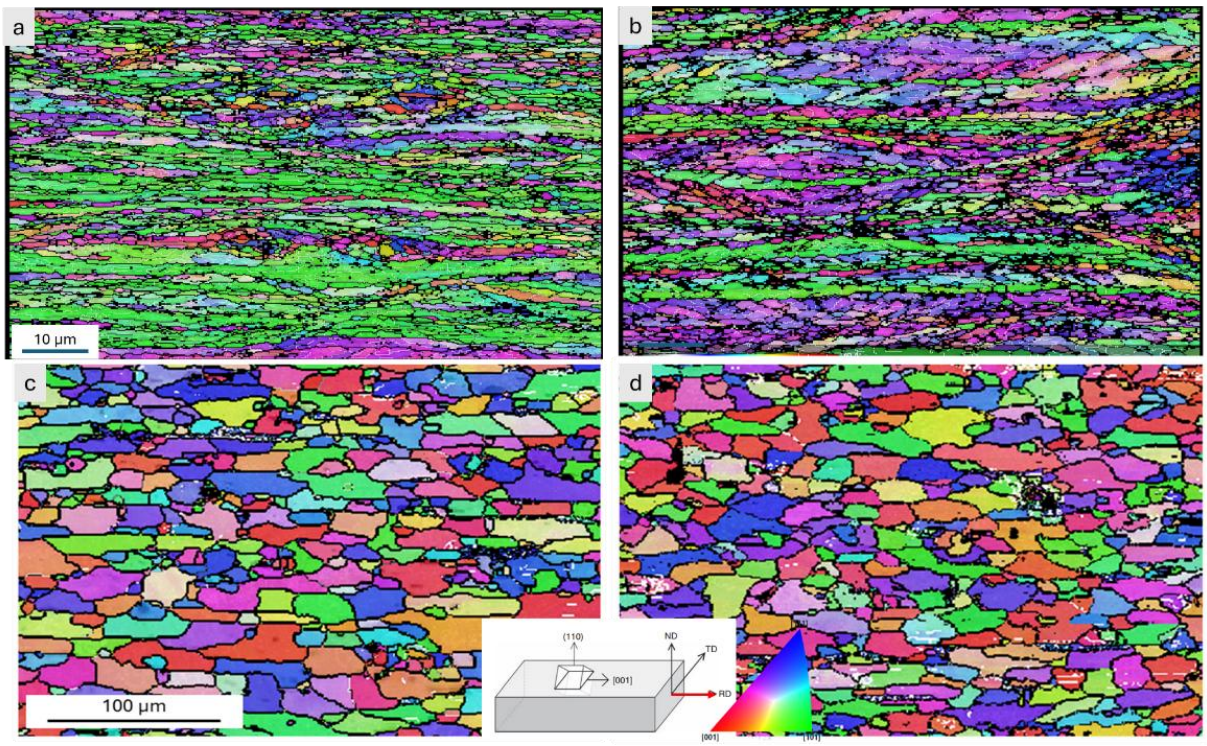

Figure 22. EBSD IPF maps for Position A (a) and (c) and Position B (b) and (d) after 3-pass deformation followed by a recrystallisation anneal, respectively.

On the other hand, The IPF maps of annealed samples indicated a fully recrystallised structure for both Positions A and B supported by new grains formed with high-angle grain boundaries, HAGB (>15° misorientation) depicted by solid black lines. However, the grain size variability is evident between the two positions. The recrystallised grains in Figure 22 (c) are typically bigger than those in (d). There were larger recrystallised grains and many small, recrystallised grains in clusters. Larger recrystallized grains were observed alongside clusters of smaller recrystallized grains, while Position B displayed a more uniform grain size distribution. This variation in grain size can be attributed to the degree of restoration through recovery during the inter-pass time and the resulting strain accumulation after P3. The difference in accumulated strain would create a sufficient difference in driving force for recrystallization, with increased strain concentration near intermetallic particles (IMPs), suggesting particle-stimulated nucleation (PSN) and leading to a bimodal grain distribution.

4.4. Texture evolution during hot rolling

To determine the anisotropy difference between Positions A and B, texture analysis was performed on both hot-rolled and annealed samples after a full three-pass sequence and during interpass times. The texture components of Positions A and B were characterized and shown as ODFs, pole figures, and texture component maps. This sub-section highlighted texture evolution during hot rolling and after recrystallisation anneal.

4.4.1. Initial texture

Texture analyses were performed from P2; thus, P2 was taken as the starting texture for this research. Figure 23 shows pole figures of samples Positions A and B, and (a) and (b) are pole figures of Positions A and B after P2, respectively. The pole figures show the well-developed deformation textures from both positions. However, the intensities of textures developed were found to be different, with Position A (a) having a maximum of 8.83 while Position B (b) showed 8.14. Furthermore, the texture index was also found to be different for both positions. Texture index provides insights into how much the orientations of the grains deviate from the randomly oriented grains, and it is mathematically expressed as J:

$$J=\int f^2(x)\,dx \qquad \textit{Equation 5}$$

When J is equal to 1, then the grains are randomly oriented, but greater than one means that the grains are preferably oriented. Figure 23 (a) shows a texture index of 9.41 while (b) shows 7.92, this shows that sample position A is highly textured than sample position B.

(a) (b)

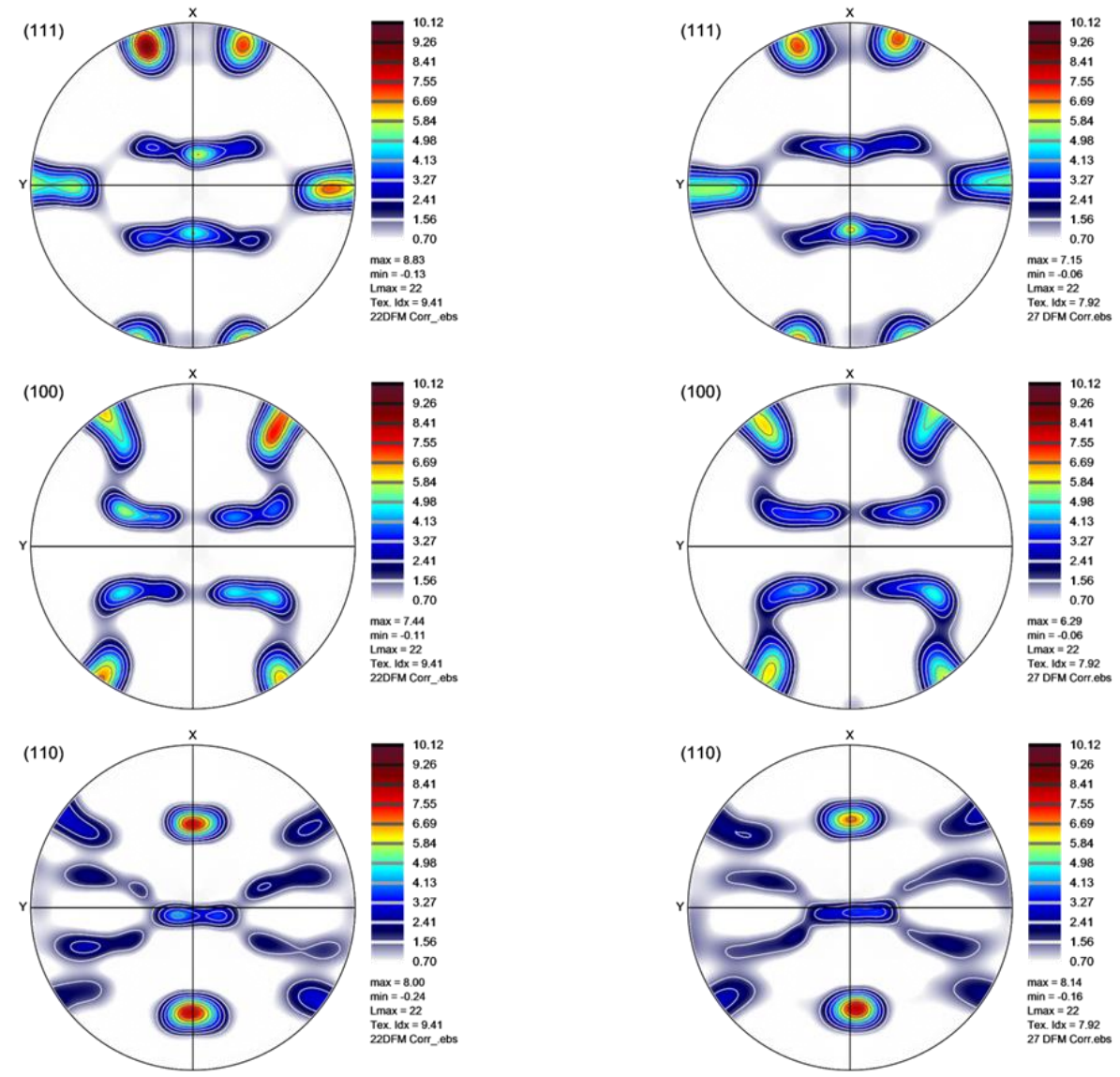

Figure 23 Pole figures of 100,111,110 to show the deformation texture after P2 on Positions A (a) and B (b)

4.4.2. Texture components developed on positions A and B after P2

Texture components developed after P2 on positions A and B were represented by Orientation distribution functions (ODF) and texture components map as shown in Figure 24.

Figure 24 (a) and (b) are ODF and texture components maps of Position A, while (c) and (d) are of Position B, respectively. The main deformation texture components highlighted here are Bs, Cu, and S and one recrystallisation texture Cb. From the ODFs, it was found that position B exhibited a slightly stronger Bs texture at the intensity of 15.97 than position A, which exhibited 15.51. The S and Cu textures were found to be also stronger in position B with an intensity of 13.5 and 3.61, while position A showed 9.67 and 3.13, respectively. The texture components map shows elongated bands of different texture components with Cb bands placed near S and/or Bs components. Furthermore, the Bs and S bands were found to be longer than the Cu bands, which appear to be broken and thinner. Figure 24 (a) and (c) show weak Cb texture components in both positions A and B. However, the intensity of Cb in position A was found to be 1.21, which was a little higher than that of position B, which showed 1.10. Position A had a longer inter-pass time before P2, during which Cb grains might have developed.

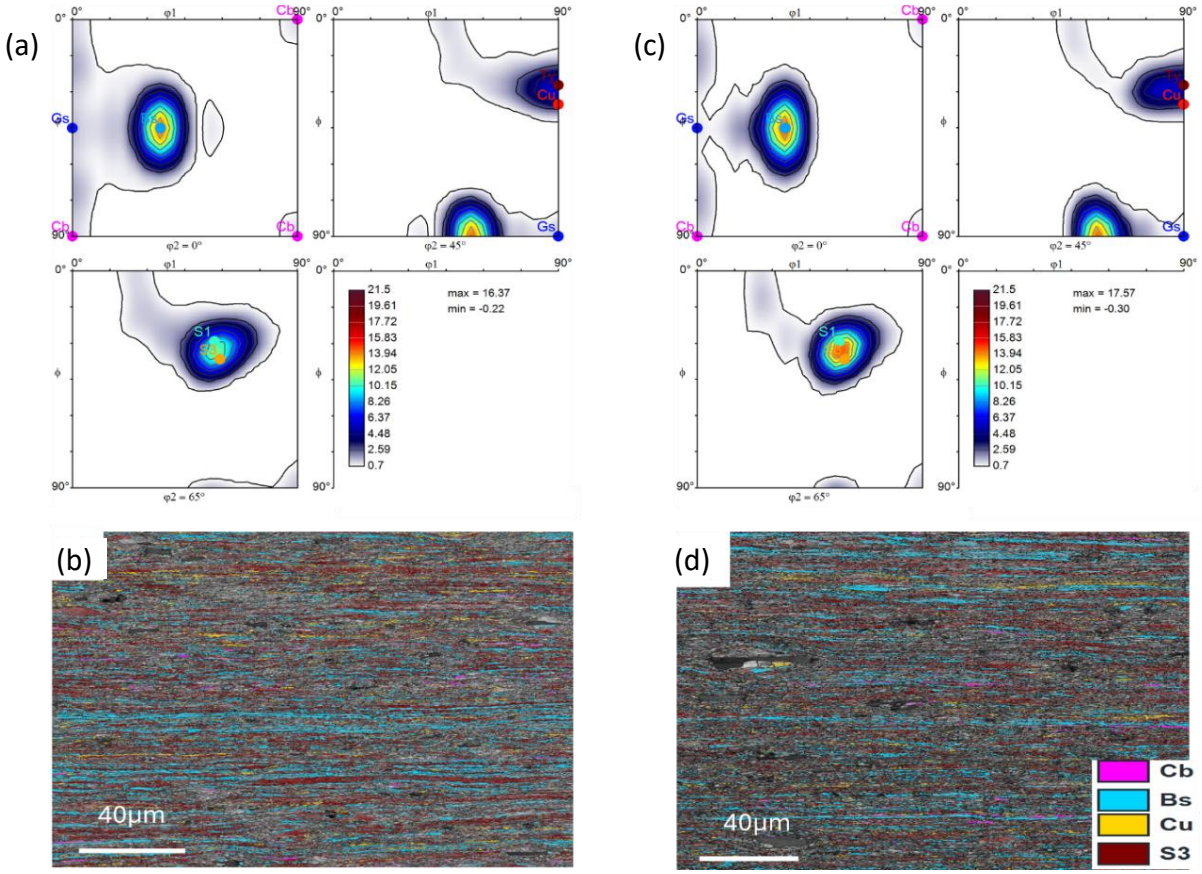

Figure 24 ODFs and texture components maps of Positions A and B after P2.

4.4.3. Effects of interpass time on texture development during hot rolling

During inter-pass times, the material recovers and /or recrystallises, reducing the strain accumulated during deformation, changing microstructure as shown in sub-sections 4.2 and 4.3, therefore, the texture developed also changed. Figure 25 illustrates how texture intensity from ODFs changed during deformation and interpass time. Figure 26 and Figure 27 show the ODFs of Positions A and B during deformation, respectively.

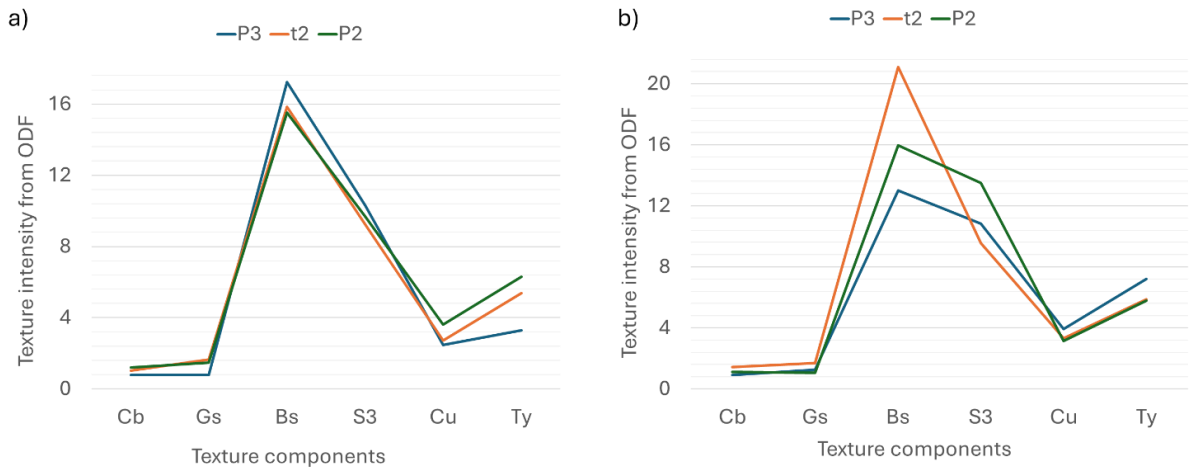

Figure 25 Changes in the texture intensity during deformation and interpass time of (a) position A and (b) position B.

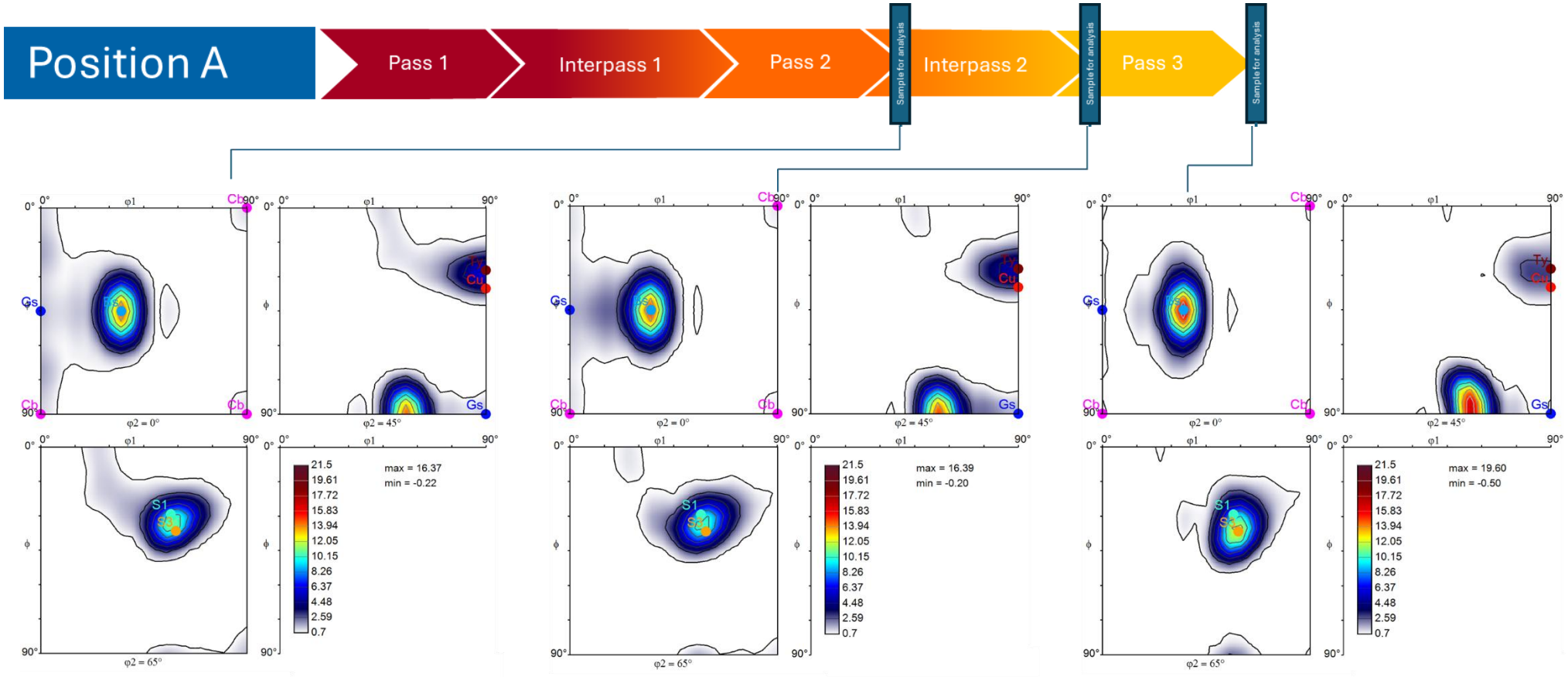

Figure 26 ODFs of position A after P2, t1, and P3 illustrate how texture intensity changed with interpass time, temperature, and strain rate

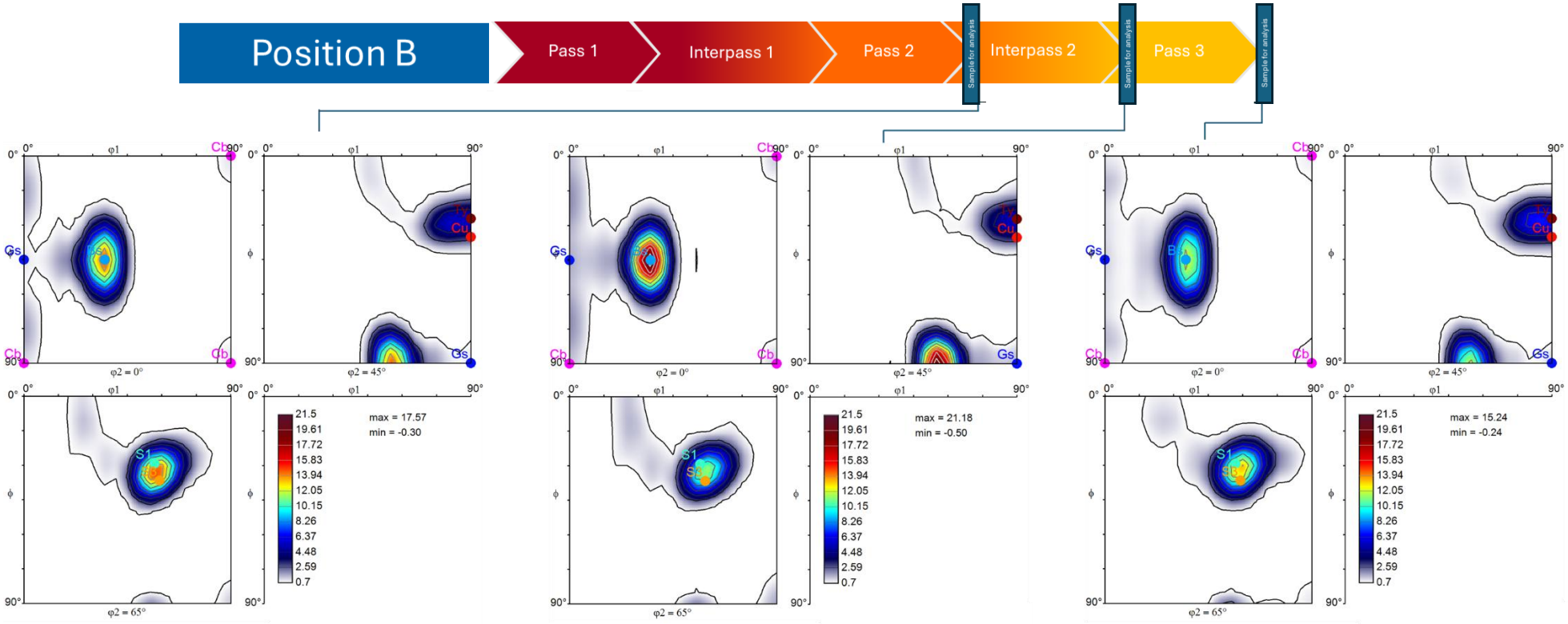

Figure 27 ODFs of position B after P2, t1, and P3 illustrate how texture intensity changed with interpass time, temperature, and strain rate

From Figure 25 (a), it is evident that there was no or little change in the texture intensity of Cb, Gs, Bs, Cu, and S3 during the short interpass time of position A. However, there was an increase in the intensity of Ty during interpass time. On the other hand, Figure 25 (b) showed an increase in the intensity of Cb, Gs, and Bs and a decrease in S3 textures during the long inter-pass time of position B, while the Ty and Cu texture components showed no change. Pole figures after P2, t_2, and P3 for Positions A and B are also shown in Appendix C and D, and they support what is observed from ODFs, strong deformation textures and weak recrystallisation textures, which their intensities change mostly during longer inter-pass time as shown in

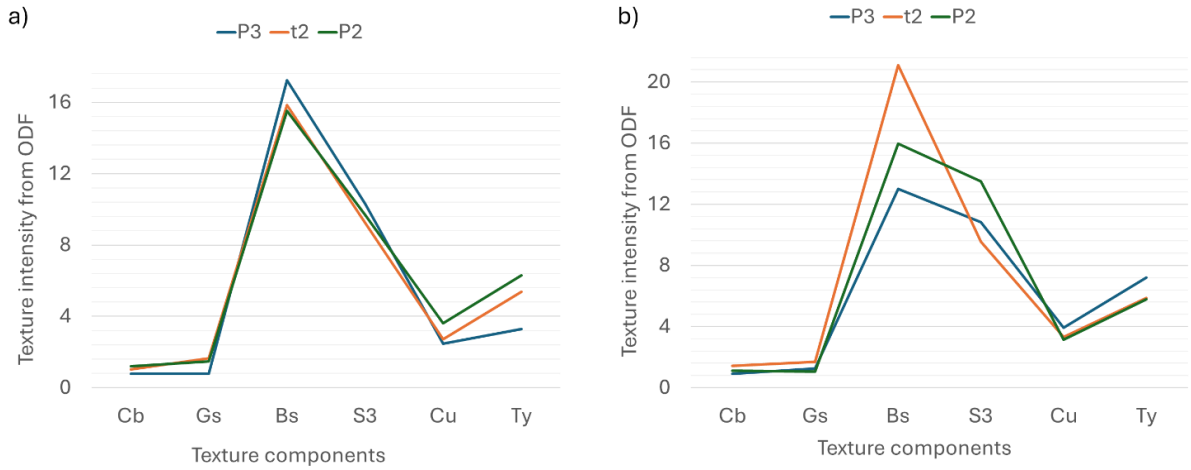

Figure 25 (b) and Figure 27.

4.4.4. Texture developed after three full pass sequence

After the second inter-pass time, the samples went through the last deformation pass (P3). Apart from deformation temperature, strain rate, and total strain that the samples went through, inter-pass times also influenced the texture developed after P3. From Figure 26 (P3) and Figure 27 (P3), deformation textures are dominated by Bs and S textures from positions A and B, respectively. The volume fraction and intensity of Bs, S, and Cu texture for positions A and B after P3 are shown in Table 8. From this table, position B showed the presence of a stronger and higher volume fraction of S and Cu texture, while position A showed a stronger and higher volume fraction of Bs texture. Position B also pointed out the presence of a very weak Cb texture component (Cb) on ODF (P3), which could have retained texture from previous deformation passes.

Position B experienced a long inter-pass time before deformation pass three (P3); therefore, it is possible that the recovery and recrystallisation occurred, and Cb texture may have developed during that time, and then retained during P3. Position B consistently showed relatively higher volume fraction and intensity of Cb texture during deformation and interpass, as shown on Figure 27. On the other hand, position A showed a very weaker and lower volume fraction of the Cb that developed during the short inter-pass time but disappeared after P3. Ty texture is considered as the intermediate of Bs and Cu texture, and as shown on the components map, it developed between Bs and/or Cu-oriented grains. Ty was found to be higher and stronger in position B than in position A.

Table 8 Volume fraction and intensity of deformation texture components after P3

	Texture component% (relative to random orientation).					
	Bs		**S3/S**		**Cu**	
	Volume fraction	**Intensity**	**Volume fraction**	**Intensity**	**Volume fraction**	**Intensity**
Position A	71.10	17.24	46.25	10.30	18.61	2.47
Position B	52.62	13.00	47.13	10.84	28.28	3.93

The volume fractions of texture components were determined using ATEX software based on the ODF rather than discrete orientations. These values are expressed relative to a random orientation distribution, indicating the volume fraction of each texture component compared to what would be expected in a randomly oriented material. Appendix F shows how the volume fraction of each component is calculated from both discrete orientations and ODF. Discrete orientations quantify grains associated with each texture component, and they may eliminate overlap, hence total volume fraction can be less than or equal to 100%. On the other hand, ODF-based calculation captures the intensity and distribution of texture components over orientation space, including overlapping regions. This was very useful as it was able to assess how sharp the texture was. By integrating over the ODF, it was possible to identify the enrichment or weakening of texture components relative to a random distribution, thereby offering a more sensitive and quantitative way to track changes in texture sharpness and dominance throughout the process.

4.5. Texture evolution during annealing

4.5.1. Introduction to recrystallisation texture

After three full pass sequences, the samples went through recrystallisation anneal to study the evolution of recrystallisation texture and, most importantly, the Cb texture, which was taken as a comparative metric between positions A and B. Recrystallisation textures include Cb, Gs, P, Q, and R. During subsequent recrystallisation after hot rolling, it is very important to develop a very strong Cb texture, which is necessary for the formation of 0/90°ears, which are essential to balance off 45° ears formed during cold rolling as a result of deformation textures. As a result, this phenomenon reduces the cup anisotropy during cup forming, leading to better mechanical properties and a reduction in material loss.

Appendix G shows pole figures of positions A and B samples after P3 and recrystallisation anneal. The well strongly developed deformation textures were replaced by weak recrystallisation textures, including random texture. After P3, the texture index was found to be 11.89 and 8.18 on positions A and B, respectively, which also proved that after deformation, the grains were highly preferentially oriented more in position A than in position B. After recrystallisation anneal, texture indices were reduced to 1.35 and 1.36 for positions A and B respectively which is closer to 1, that is, more grains were randomly oriented other than textured. However, there were still weakly textured grains.

4.5.2. Texture components developed during annealing

Figure 28 (a) and (b) show ODFs after full three-pass deformation plus recrystallisation anneal representing positions A and B, respectively. The ODFs show the presence of different recrystallisation textures, and it is evident that the intensity of deformation textures is diminished. Figure 28 (a) indicates the presence of strong Cb texture in position A, with a long-short inter-pass time combination as a dominant recrystallisation texture and the dominance of the Gs and P texture components in position B, with the short-long inter-pass time combination. Both positions A and B also indicated the presence of a higher intensity of Random texture, which is commonly associated with PSN. Furthermore, there is a presence of {111} <110> texture along y-fibre, <111> ND in position A.

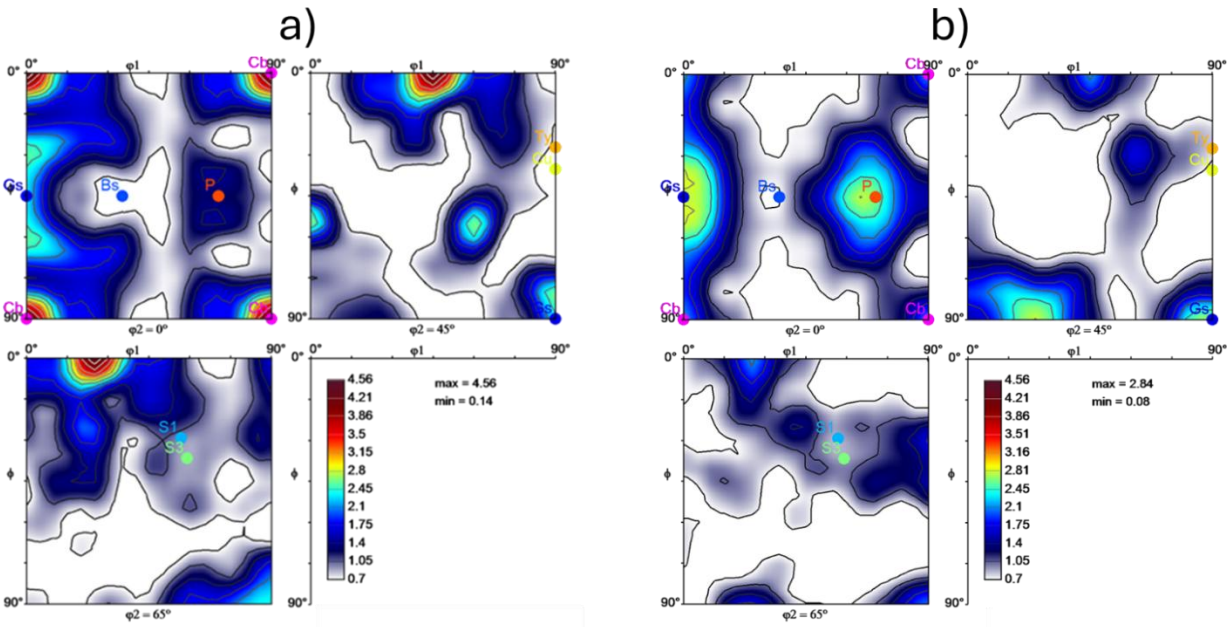

Figure 28 ODFs of (a) position A and (b) position B after recrystallisation anneal.

Figure 29 shows the volume fraction of different deformation and recrystallisation texture components present in both positions A and B after recrystallisation anneal. The volume fraction calculations are based on the ODF peak intensities, and they give an indication of how much each texture component is related to random distribution. The graph also depicts that in both positions, volume fractions of deformation texture components are very low, with Bs and Cu at 6.99% and 7.1% for position A and 7.89% and 7.61% for position B, respectively. Furthermore, position B has a higher volume fraction of Ty texture (8.48%) than position A (7.97%), but they both have the same volume fraction of the S component (7.8%).

The difference in inter-pass times between the two positions affected the volume fractions of recrystallisation textures. Position A, which experienced a long-short inter-pass time, has a higher volume fraction of Cb texture at 19.59%, compared to 11.82% for position B, which experienced a short-long inter-pass time. Furthermore, position B has higher volume fractions of the Gs, P, Q, and R texture components than position A. Specifically, position B has volume fractions of 21.54% for Gs, 19.98% for P, 4.87% for Q, and 3.93% for R. In contrast, position A has volume fractions of 17.6% for Gs, 10.5% for P, 3.72% for Q, and 3.5% for R.

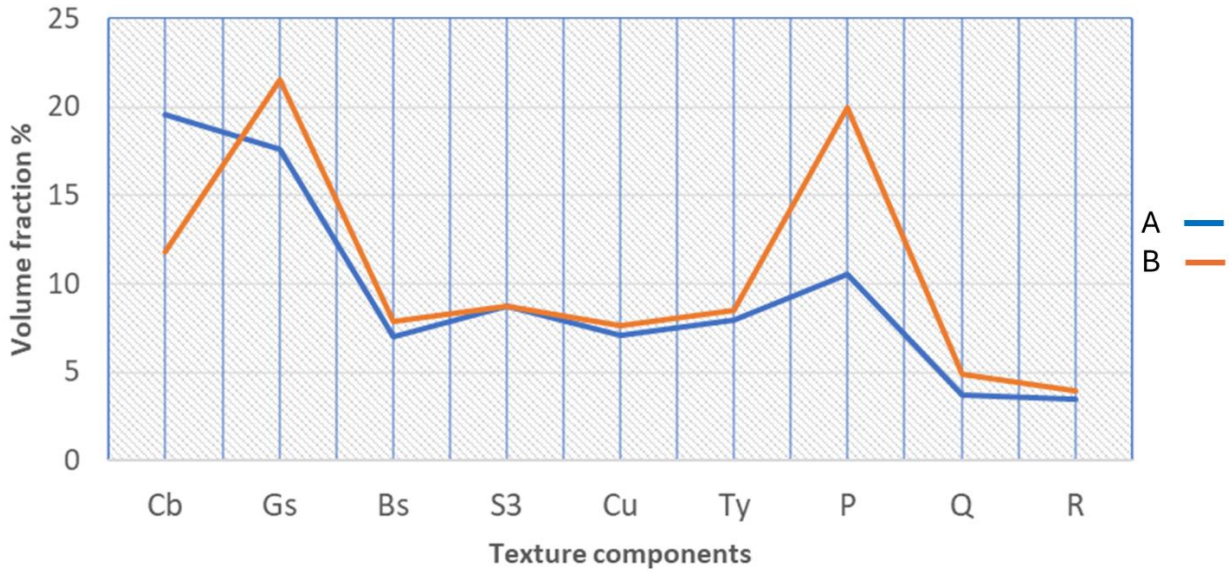

Figure 29 Volume fractions of recrystallisation and deformation textures after recrystallisation anneal.

5. Discussion

5.1. Effects of interpass time on:

5.1.1. Mechanical properties

There was a softening during interpass time, which affected the microstructure development on subsequent deformation passes and after recrystallisation. In this study, the softening between passes was investigated by performing hardness tests on samples after and before deformation, and the results are depicted in Figure 17. It was found that position A exhibited higher hardness values than position B after the final deformation. This suggests that the short inter-pass time experienced by position A before P3 leads to a lower hardness reduction, while a longer inter-pass time experienced by position B leads to greater softening periods due to extended recovery.

During recovery, dislocation intensity is decreased through dislocation annihilation and the formation of cells and sub grains [62], therefore, there is a reduction in the driving force for recrystallisation on subsequent annealing. Aluminium is a high-stacking fault energy metal; the climb is rapid, and as a result, significant recovery is possible [50], [62]. This was also supported by flow stress plots in Figure 16, which depicted higher flow stress on position A during P3 than on position B. During deformation, the dislocations multiply and entangle with one another, increasing the dislocation density; as a result, the material work-hardens, increasing the flow stress. However, when softening occurs between passes, the dislocation density decreases, reducing the flow stress on the subsequent deformation pass. Position B experienced extended softening periods before P3, while position A experienced shorter softening periods.

5.1.2. Microstructure evolution during deformation

A transfer bar (hot rough rolled aluminium strip) with elongated and few recrystallised grains was hot deformed through a three-pass deformation schedule, as summarised in Table 6, to simulate hot finish rolling in a single stand reversing mill where both ends of the bar experienced different inter-pass time. From the results obtained, it was found that softening that occurred during interpass time did not only affect the mechanical properties but the strain energy accumulation, as well as microstructural features, as differences were evident

when comparing positions A and B. The inter-pass time in high-temperature multipass deformation leads to two principal softening mechanisms, namely, static recovery and static recrystallisation; thus, different interstage delay times before the next deformation pass have a different influence on the next stage of peak stress [51]. Longer inter-pass time experienced by position B before final deformation reduced the strain accumulated through static recovery; hence, lower flow stress during P3 than in position A. Yan et al. [51] investigated static softening behaviours of 7055 alloy during the interval time of multi-pass hot compression, especially the microstructural observations and they found that the longer the delay times before the next pass the more the reductions in the flow stress after the following pass. Moreover, Giordani et al. [50] did a similar study on an Nb- and N-bearing austenitic stainless steel biomaterial, where they investigated the proportion of recovery and recrystallisation during interpass times at high temperatures. Softening during inter-pass times was measured in terms of fractional softening, and they found that fractional softening increased with increasing inter-pass time and temperature.

Static recovery during interpass, as discussed above, reduces the retained strain energy, leading to changes in the misorientation between grains. Consequently, these modifications influence the final microstructure, altering its characteristics. Figure 30 illustrates the evolution of grain misorientation during the interpass period and highlights the influence of softening between passes on grain misorientation following the final deformation pass. Low-angle grain boundaries (LAGBs) form during deformation and recovery, while high-angle grain boundaries (HAGBs) develop during recrystallisation. After a longer interpass time at position B, the proportion of LAGBs decreased, whereas the fraction of HAGBs increased, as shown in Figure 30 (b). This suggests that sub grain formation and sub grain coarsening took place during longer interpass time, leading to the formation of high-angle grain boundaries (HAGBs). This observation is further supported by changes in the aspect ratio after an extended interpass time, as shown in Figure 31.

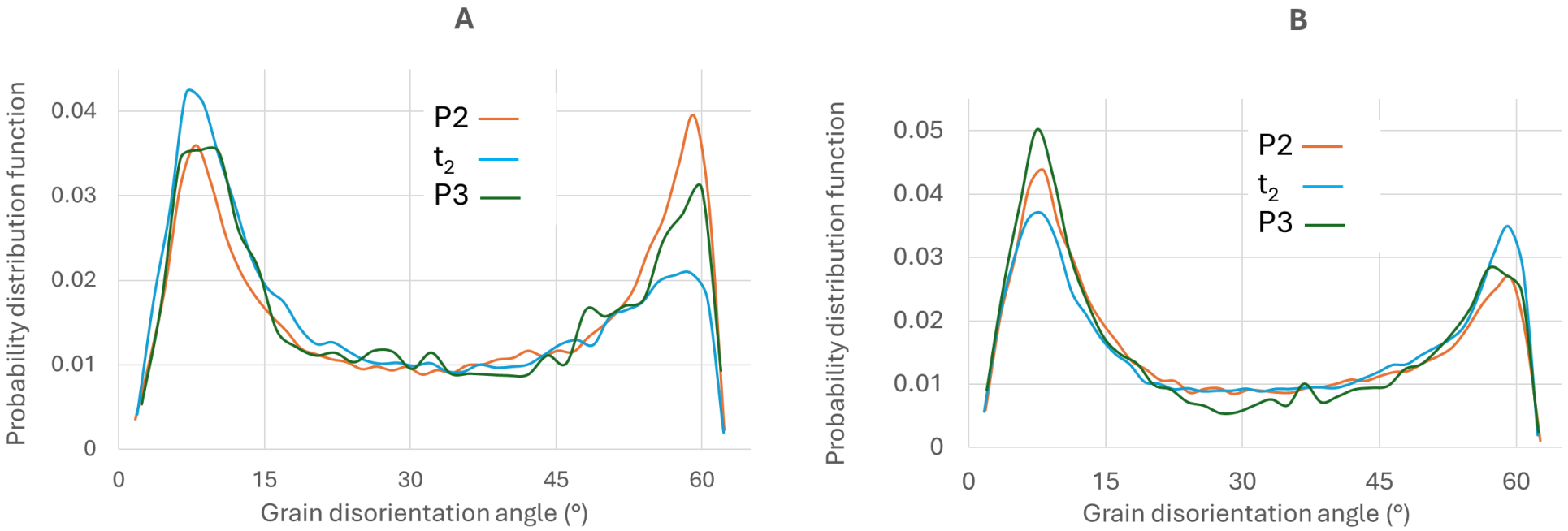

Figure 30 Grain Disorientation of (a) and (b) Positions A and B illustrating how grain boundary formation changed with interpass time, respectively

The grain aspect ratio, defined as the ratio of grain length to width, serves as an indicator for distinguishing between recrystallised/recovered and deformed grains. A ratio closer to 1 represents equiaxed grains, whereas values greater than 1 indicate elongated or flattened grains. After an extended softening period at position B, the grain aspect ratio decreased, with the distribution shifting closer to 1 and the relative frequency of lower aspect ratios increasing. In contrast, after a short interpass time at position A, the aspect ratio also decreased; however, the changes were not as pronounced as those observed at position B. This further suggests that longer interpass times facilitated greater static recovery, which in turn promoted sub-grain coarsening.

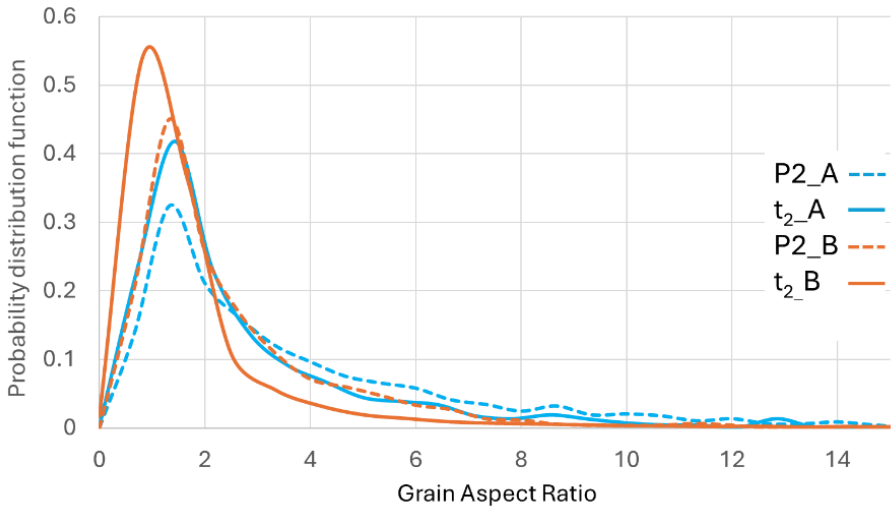

Figure 31 Effects of interpass time on the grain aspect ratio

After the third deformation pass (P3), position B exhibited a higher fraction of low-angle grain boundaries (LAGBs) compared to position A. The longer softening period before P3 allowed for extensive recovery, facilitating the rearrangement of dislocations into sub grains. During P3, grains became elongated; however, the presence of sub grains formed during the interpass time influenced not only the misorientation of grains but also the grain aspect ratio. Position B demonstrated a higher relative frequency of lower aspect ratios, meaning the grains were closer to an equiaxed shape (aspect ratio near 1), as shown in Figure 33.In contrast, position A experienced a shorter softening period before P3, limiting the formation of sub grains. As a result, after P3, grains in position A were further elongated, leading to an increased grain aspect ratio.

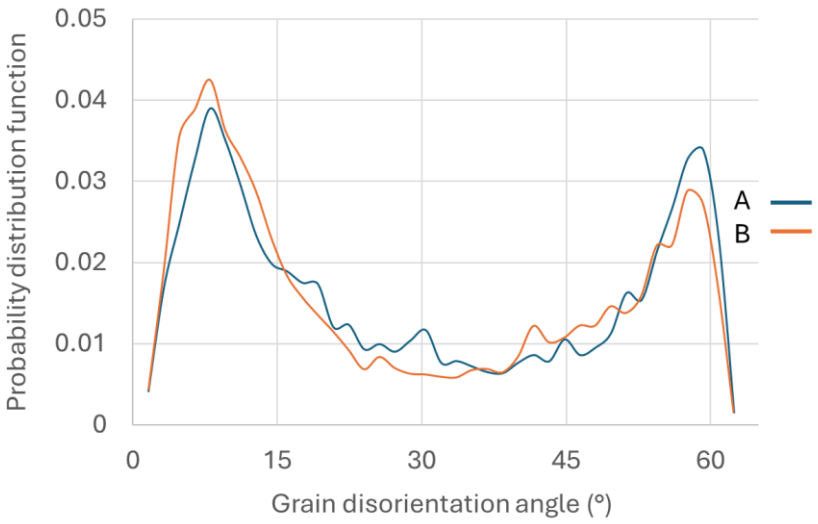

Figure 32 Grain disorientation distribution of Positions A and B after P3

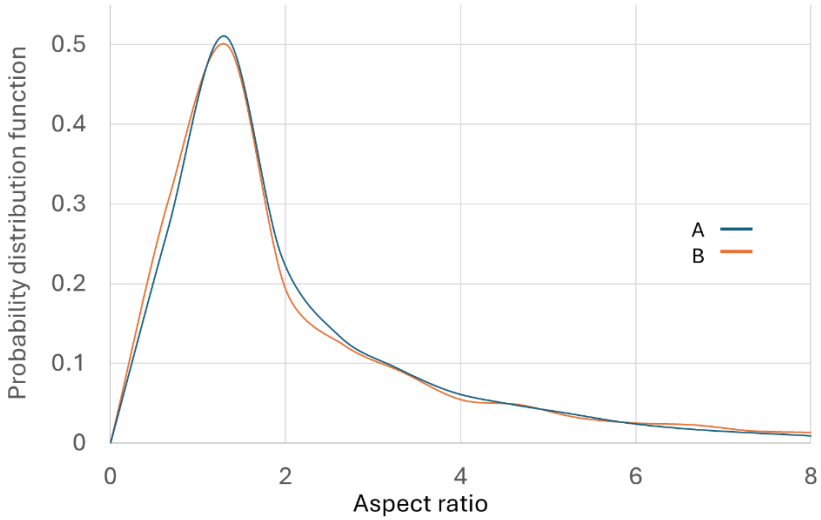

Figure 33 The grain aspect ratio of Positions A and B after P3

Although position B exhibited a slightly higher fraction of low-angle grain boundaries (LAGBs) than position A after deformation pass P3, these LAGBs did not significantly contribute to the stored energy. Instead, position A retained a higher stored energy than position B at this stage. Figure 34 presents the Grain Orientation Spread (GOS) plots for Positions A and B during deformation, illustrating how local misorientation evolved throughout the interpass time and following the subsequent deformation pass (P3).

GOS represents the average difference in orientation between each pixel within a grain, providing a measure of the internal misorientation. This parameter is useful for assessing local strain distribution between grains and distinguishing between recrystallised/recovered and

deformed grains. Smaller grains that have undergone recrystallisation or recovery typically exhibit a low orientation spread (GOS < 1°) [63] or (GOS < 2°) [64] , while larger grains tend to retain more deformation strain and, as a result, exhibit higher Grain Orientation Spread (GOS) value. Figure 34 (a) shows that at GOS < 1°, position B, after a longer interpass time (t2_B), exhibited a higher intensity of recovered grains compared to its state after P2. Additionally, the peak at GOS < 1° for t2_B was higher than that of position A at all stages. This observation further indicates that during the extended interpass time, grains underwent static recovery, leading to the formation of new sub grains and sub grains coarsening with minimal or low dislocation density. Consequently, this process contributed to a reduction in the overall stored energy. This is also shown in Figure 34 (b) whereby after P3, position B exhibited lower frequency of grains beyond GOS > 1°.

During deformation P3, new dislocations were introduced, resulting in increased strain accumulation. However, since position B experienced longer softening periods than position A before P3, dislocation density was reduced in position B, leading to lower strain accumulation after P3 compared to position A, which had a shorter interpass time. It was observed that, unlike position B, position A exhibited a slight difference in the frequency of grains at GOS < 1° during the short interpass time. Furthermore, position A displayed a relatively higher frequency of grains at GOS > 1° after P3, indicating a slight reduction in dislocation density during the short interpass time.

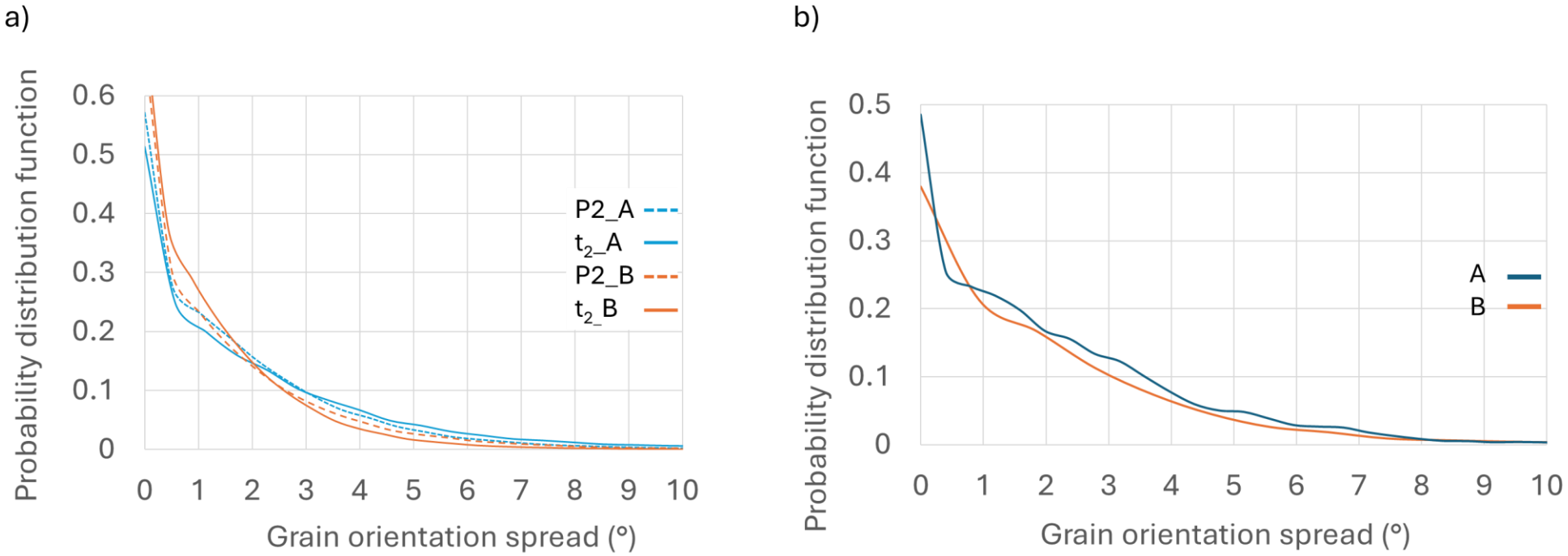

Figure 34 Grain Orientation Spread of Positions A and B after deformation (a) P2 and t_2 and (b) P3

5.1.3. Microstructure evolution after recrystallisation

The difference in the thermomechanical history of Positions A and B during deformation does not only affect the mechanical properties of the material but also affects the microstructure development during deformation and on subsequent recrystallisation anneal. Position A was found to have higher flow stress than position B after three full pass deformation sequences, as shown in Figure 16. This suggests that position A had more strain energy accumulated than position B; therefore, it is expected that during subsequent anneal, more free strain energy grains will be formed [62]. After recrystallisation anneal, both Positions A and B appeared to be fully recrystallised, as shown in Figure 22 (c) and (d) with clear high-angle grain boundaries. The grains were found to be equiaxed, with position A exhibiting a larger grain size compared to position B. This suggests that grain growth may have occurred in position A following recrystallisation.

The interpass time variation in Positions A and B has an impact on the strain accumulation during the passes; therefore, the extent of recovery, the concurrent dispersoid formation, as well as the recrystallisation kinetics vary. Thus, influences the final grain microstructure and recrystallisation texture after recrystallisation anneal. Huang et al. [65] studied the control of grain structure and texture in Al-Mn alloys through the competition between precipitation of concurrent dispersoids and recrystallisation. They found that, depending on the annealing heating profile, concurrent dispersoids could form both before and during recrystallisation. Additionally, their study demonstrated that during the pre-recovery step, prior to the onset of recrystallisation, concurrent dispersoids were particularly formed in two-step and three-step annealing processes.

Strain energy accumulated during deformation is the driving force for recrystallisation during annealing. High-strain energy accumulated leads to more equiaxed grains with clear high-angle grain boundaries, while lower strain energy leads to fewer equiaxed grains and more elongated grains with low-angle grain boundaries, which may grow towards ND direction at high temperature. Furthermore, high strain energy increases recrystallisation kinetics, therefore, at higher temperatures, recrystallisation may be completed within a very short period, and annealing for a longer time may result in grain growth.

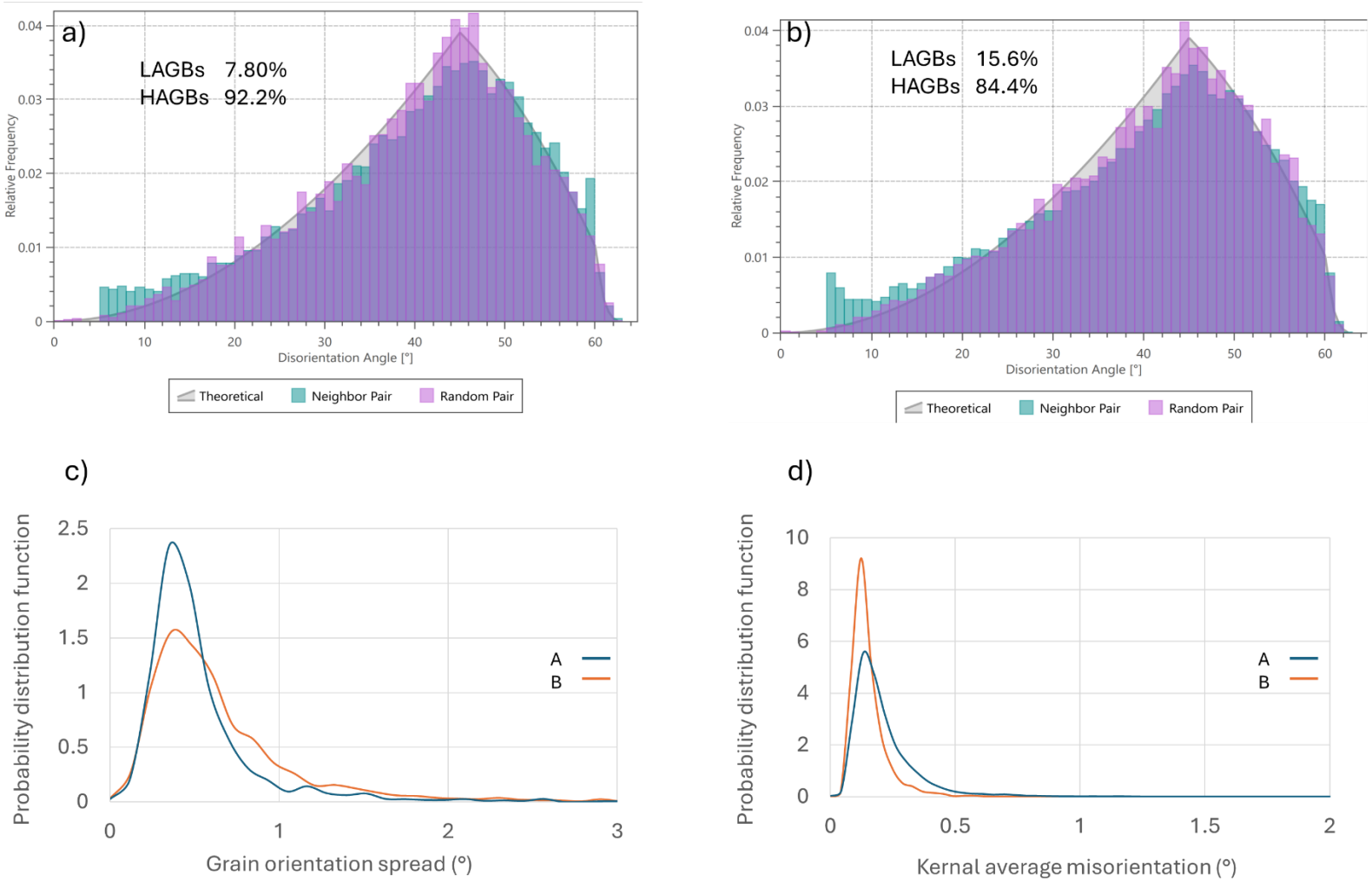

Figure 35 Grain Disorientation Angle of (a) position A and (b) position B, (c) Grain orientation spread and (d) Kernal average misorientation of Positions A and B after recrystallisation

Figure 35 (a) and (b) show the Grain Disorientation Angle distribution for Positions A and B, respectively, after recrystallisation. These distributions are comparable to the McKenzie graph, which represents the theoretical disorientation distribution of a fully recrystallised material. However, the presence of low-angle grain boundaries (LAGBs) remains in both positions, with position B exhibiting a higher fraction of LAGBs compared to position A.

The LAGBs in position B may represent sub grain structures formed during the longer interpass time. As a result of reduced strain accumulation, grain boundary mobility during recrystallisation may have been limited, leading to the retention of sub grains with LAGBs, while some coalesced to form high-angle grain boundaries (HAGBs). In contrast, position A exhibited more HAGBs after recrystallisation. The higher strain energy accumulated during deformation in position A enhanced recrystallisation kinetics, promoting the formation of grains with lower strain energy and more HAGBs.

These findings are consistent with the GOS and Kernel Average Misorientation (KAM) distribution graphs, which indicate that position A had more grains at the lowest angles, as shown in Figure 35 (c) and (d).

5.2. Texture development during three full pass deformation sequence

During hot deformation, dynamic recovery occurs simultaneously with deformation, leading to the development of recrystallisation textures. The results indicate that during hot rolling, position B consistently exhibited a stronger Cb texture compared to position A, as shown in Figure 25. This can be associated with the activation of non-octahedral slip systems during high deformation temperatures; above 300°C, which influence the development of recrystallisation textures [6]. Cantergiani et al. [66] investigated the influence of strain rate sensitivity on Cb texture evolution in aluminium alloys and found that during hot rolling, the stability of Cb texture depended significantly on strain rate sensitivity. They also discovered that the volume fraction of retained Cb texture increased and stabilised further due to the activation of non-octahedral slip systems. This was quantified using the parameter r^{110}, defined as the ratio of the critical resolved shear stress on non-octahedral slip systems to the critical resolved shear stress on octahedral slip systems. In this study, three non-octahedral slip systems were studied and are shown in Figure 36. Li et al. [8] explained that the presence

of {110} <110> slip system promotes the stability of Cb texture. As shown in Figure 37, position B consistently exhibited a higher volume fraction of the {110} <110> slip system, although in relatively small quantities. Therefore, it can be inferred that the stronger Cb texture observed in position B compared to position A during deformation was influenced by the presence of the {110} <110> slip system. However, the literature [8] shows that the high amount of Mn reduces the probability of activating {110} <110> slip system during hot deformation.

On the other hand, the {100} <110> slip system is associated with the development of the Bs texture during deformation. Position A exhibited a higher volume fraction of the {100} <110> slip system after deformation P3, which could explain why position A developed a stronger and higher volume fraction of the Bs texture after P3. Li et al.[8] further explained that the presence of the Bs texture is not solely dependent on non-octahedral slip systems but is also influenced by the level of stored energy. High stored energy provides resistance to Bs-oriented grains, preventing their rotation toward the Gs orientation. This explains why position A exhibited a higher volume fraction of the Bs texture after deformation pass P3. Position A experienced a shorter interpass time before P3, leading to greater strain accumulation compared to position B, as previously discussed in section 5.1.

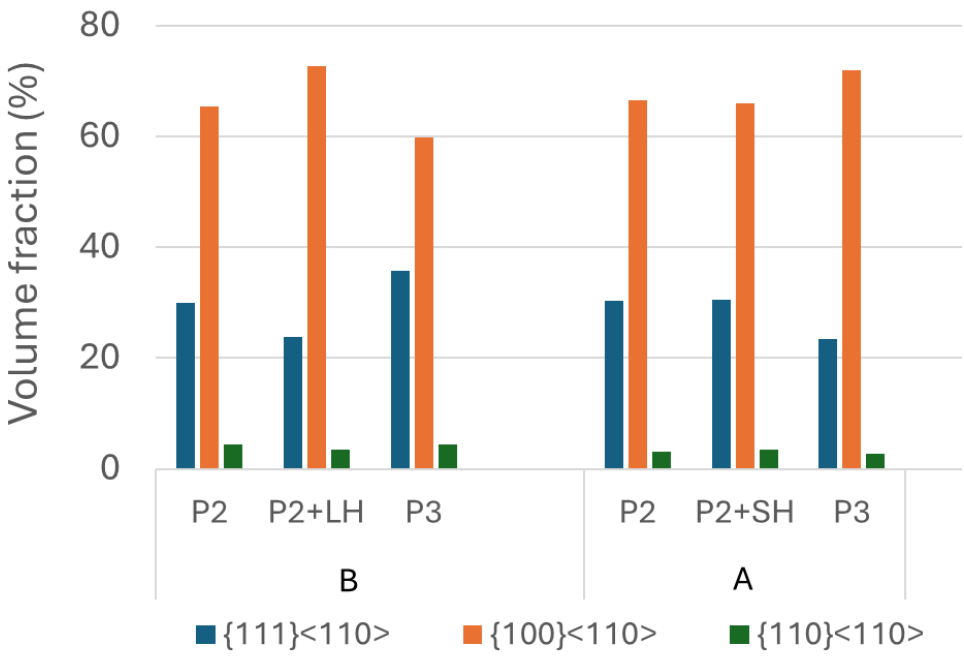

Figure 36 Non-octahedral slip systems activated during hot rolling (determined using ATEX software tools - See Appendix F).

5.3. Evolution of recrystallisation texture after annealing

The intensity and volume fraction of all deformation textures diminished drastically during recrystallisation. The deformation textures transformed into different recrystallisation textures through the movement of special grain boundaries, CSLs, and SIBM.

The intensity of the Gs and P texture components of position B was found to be greater than that of position A. Furthermore, the volume fractions of Gs and P texture in position B are higher than that of position A by 3.94% and 9.48%, respectively as shown in Figure 29. Variations in interpass times influence not only microstructure development but also the evolution of texture. The microstructural restoration occurring during longer interpass times may have created favourable nucleation sites for the formation of P- and Gs-oriented grains and/or promoted the preferential growth of these orientations during subsequent annealing. Texture formation is typically explained by two primary mechanisms: oriented nucleation and oriented growth [50], [55], [56], [57]. In this case, the microstructural changes induced by extended softening periods likely contributed to the preferential development of specific texture components, influencing the overall texture evolution in the material.

The higher fractional volume of Gs-oriented grains in position B may have been retained from the deformation process. After deformation pass P3, position B exhibited a greater volume fraction of Gs-oriented grains compared to position A, as shown in Figure 25. The Gs texture is one of the components that form during both dynamic and static recovery, as it is the softest texture component with the lowest elastic modulus. During deformation, grains tend to align themselves in a manner that minimises stored energy in the system. Since the Gs orientation has the lowest elastic modulus, grains can orient themselves such that this direction aligns with the maximum applied stress, thereby facilitating energy reduction and promoting the development of the Gs texture component [61].

Hence, Gs-oriented grains are likely to form during recovery to maintain their stability. Position B, which experienced extended recovery due to the longer interpass time, may have retained Gs-oriented grains or caused slight misorientation, with an eventual increase in their fraction during subsequent annealing. The early-stage development of Gs texture in aluminium, as explained by Ghosh [61], may be attributed to these factors. The prolonged recovery period in position B could have facilitated the stabilisation and retention of Gs-

oriented grains, contributing to their increased presence after recrystallisation. On the other hand, position A experienced a very short inter-pass time, resulting in limited recovery and minimal formation of Gs-oriented grains. Consequently, the presence of Gs grains in position A can be primarily attributed to recrystallisation rather than recovery.

Regarding a stronger and higher volume fraction of P texture in position B compared to position A, the literature centres the explanation on PSN [46], [67]. Studies suggest that P-oriented grains develop within the deformation zone around constituent particles after significant deformation passes [65]. There is a possibility that during the longer inter-pass time in position B after P2, diffusion of Mn (manganese) may have occurred, leading to the formation of fine dispersoids known as type II and III dispersoids, which concurrently precipitated during recovery or with recrystallisation. The study made by Huang et al. [68] showed that during pre-recovery, a substantial amount of stored energy is dissipated, while a greater number of fine dispersoids simultaneously precipitate from the solid solution.

Type II dispersoids are dispersoids that heterogeneously precipitate on grain/sub grain boundaries prior to recrystallisation (type II) or concurrently with recrystallisation (type III) at low annealing temperatures of the deformed material [65]. Dispersoids reduce the recrystallisation kinetics [41], [42], [44] and lead to the development of strong uncommon textures like ND Rotated Cb and P-texture [46], [65], [69]. Moreover, because of some extended softening that occurred during the longer inter-pass time of position B, which lowered the final strain energy accumulated before recrystallisation anneal, the recrystallisation kinetics were further lowered. The lower intensity and volume fraction of P texture in position A can be attributed to higher stored energy due to short inter-pass time. Huang et al. [65] in their study showed that when the formation of concurrent dispersoids (type II & III dispersoids) is reduced due to quick recrystallisation kinetics and/or lack of precipitation, the intensity of P-texture is reduced.

Tangen et al. [46] found that the P texture and rotated ND Cb texture components nucleation sites experience an initial growth benefit over PSN sites because of their 40°<111> rotation relationship to the Cu texture. They further explained that these sites exhibit a growth advantage because of the higher mobility of the reaction front relative to grains with random orientations. Additionally, the grain boundaries between these sites and the surrounding matrix are of the ∑7 types, which are believed to be less influenced by solute segregation and

precipitation. As a result, these highly ordered boundaries contribute to the early growth advantage.

Studies made by [46], [65] also explained that the material that recrystallises without the effects of concurrent precipitation results in an equiaxed grain structure with strong random texture while the one affected by concurrent precipitation experiences Zener pinning and results in coarse grained structure with a sharp P and ND rotated Cb texture components. From the results obtained in this research, Position B was affected by concurrent dispersoids, which led to the formation of a stronger P texture and a weaker Cb texture. However, the grains were fully recrystallised, and the Zener pinning affected the grain growth, leading to grains with smaller grain size distribution as compared to position A.

Xie et al. [67] later found that P texture components can grow from original P orientations that may be stable during the deformation and from non-P oriented grains that are oriented between 33.6-56.4° to {023}<100> or nearly Gs texture. Specifically, they found that P grains are surrounded by grains of {023}<100> with the orientation of 44.6°<121>, 52° <323>, 49.9° <223> and, 51°<334>, which is like the preferred growth of P orientation about 40°<111> in recrystallisation annealing. According to the strain energy release maximization theory, non-P grains, particularly near Gs orientation, can transform into P orientation during recrystallization [43].

In contrast, position A showed Cb texture as a dominant texture component with a volume fraction higher than that of position B by 8.07%. Position A experienced a short inter-pass before final deformation; therefore, it had higher retained strain energy, which is the driving force for recrystallisation. The high deformations introduce more nucleation sites and because of limited or no recovery during short inter-pass times, there were more nucleation sites for recrystallisation. These include transition bands, Cb bands shear bands, and PSNs. Hence, position A also has more randomly oriented grains than position B. Humphreys and Hatherly [62] mentioned that Cb-oriented grains are metastable during hot deformation and they are retained as deformation bands and during recrystallisation anneal, Cb grains nucleate on those sites. Unlike position B, the rate of concurrent dispersoid formation was limited in position A, therefore, it might not have experienced greater Zener pinning, and the recrystallisation rate might have been higher, as a result, more recrystallised nuclei were formed, and grains were able to grow thereafter.

Cube grains were found to be larger than other textured grains. Studies [62], [70] explained this occurrence as a result of higher mobility of a 40° <111> CSL boundary between S and Cb, which promotes faster growth of the grains or the one between Bs and Cb.

5.4. Contribution of second phase particles to the recrystallisation textures during annealing

Recrystallisation texture components of both Positions A and B samples consisted of random texture component, as shown by pole figures of recrystallised samples in Appendix F. Random texture is one of the texture components that develop during recrystallisation annealing. The development of recrystallisation textures during annealing is normally explained by nucleation and growth mechanisms. Texture components can nucleate from transition bands of their texture component, for example, Cb grains can nucleate from Cb bands retained during deformation. They can also nucleate around large particles known as PSN sites. PSN sites are known to promote the development of randomly orientated grains with weak textures like P and weaken the formation of Cb texture [71]. Position B showed a lower volume fraction and weaker Cb texture than position A, and it also consisted of a weaker P texture component, which suggests that position B had more PSN sites than position A and the grains were more randomly oriented than they were in position A.

Moreover, PSN sites also reduce recrystallised grain size. After recrystallisation of three full pass sequence samples, position B samples had more grains with smaller grain sizes compared to position A samples, which showed some degree of grain growth. A reduced grain size is associated with particle-stimulated nucleation (PSN) sites. Figure 37 shows a grain size distribution of Positions A and B after recrystallisation of three full pass deformation sequences. Weak P-texture is also associated with concurrent dispersoids. Position B had a pre-recovery stage during a long inter-pass time from which it can be hypothesised that type II and III dispersoids might have concurrently precipitated. Furthermore, long inter-pass time reduced stored energy, reducing recrystallisation kinetics energy, thereby delaying recrystallisation while promoting the development of concurrent dispersoids. Small dispersoids might have retarded grain growth post-recrystallisation, reducing the grain size of position B samples. However, with higher recrystallisation kinetics in position A,

recrystallisation might have been rapid, and the extended annealing time promoted grain growth, and there might have been little or no dispersoids formed to retard grain growth.

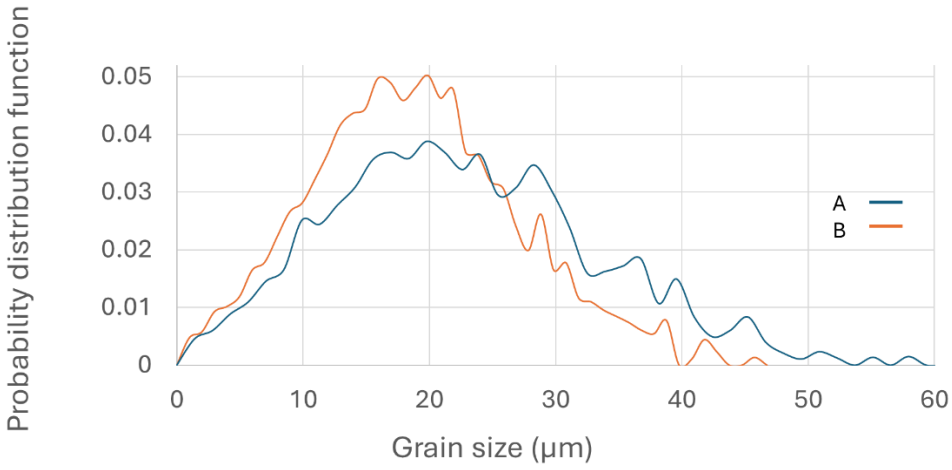

Figure 37 Grain size distribution of Positions A and B after recrystallisation anneal

5.5. Evolution of Cube texture

Position A has a stronger and higher volume fraction of Cb texture than position B after recrystallisation, as shown by ODF in Figure 28. This could be attributed to several reasons, which include the amount of retained Cb bands during deformation, the type of boundaries between grains/sub-grains in the deformed state, the growth rate of the new grains, the stored energy of the grains from which new grains grow into, and the stored energy of the new grains [39]. In Figure 38, the location of Cb bands on the deformed sample is highlighted. From both Positions A and B, Cb bands were mostly found between Bs and S bands or just near S bands or Bs bands throughout the deformation passes, and they were much shorter than other deformation bands.

This agrees with the research by Brahme et al. [39] from which they showed that Cb texture grains were more likely to nucleate from S-oriented grains than from any other orientations and possibly from Bs-deformed grains than from Cu grains. They further explained that this was because S-oriented grains have higher stored energy than any other orientations, hence, they are more likely to nucleate new grains during recrystallisation to reduce the energy. Furthermore, all other deformation texture components are likely to form S grains during recrystallisation.

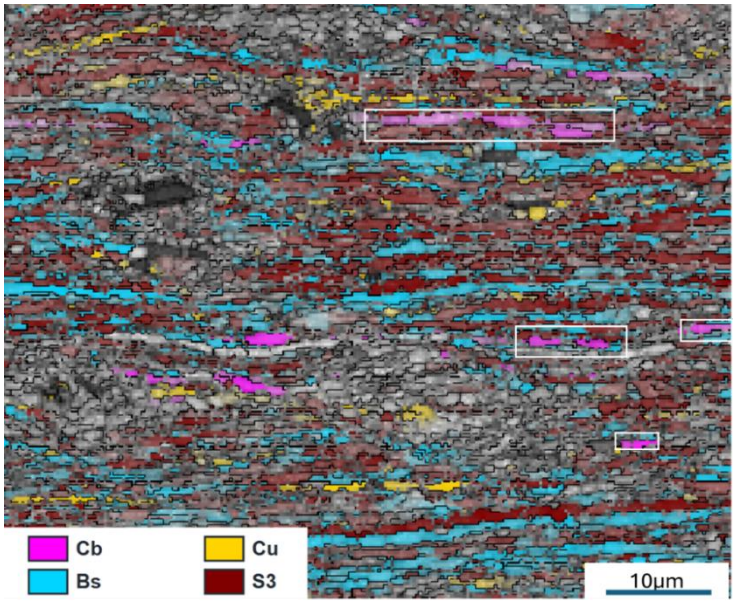

Figure 38 EBSD map of orientation distribution of deformed sheet illustrating texture components after deformation

Humphreys and Hatherly [62] mentioned that the high retained strain energy of S-components provides the driving force for Cb bands near the S-components to grow into Cb grains during recrystallisation through strain-induced boundary migration (SIBM), from which Cb sub-grains consume neighbouring sub-grains. After the third deformation pass, position B had more Cb bands than position A, which might have been the main source of the developed Cb grains during annealing. Unlike other studies [52], [53], [62] where they found that the Cb grows from the S-deformed grains, Zhao et al. [57], [72] found that Cb grains grow from the Bs-deformed grains. They explained that it could be that the strong presence of Bs texture might have been the reason why only Bs grains grew into Cb grains.

Consequently, it can be assumed that the stronger and higher volume fraction of Cb grains on position A after recrystallisation is due to the presence of stronger Bs texture as they have a similar volume fraction of S3 texture. Furthermore, Zhao et al. [57] also explained that Bs grains do not only grow into Cb grains but also into Gs grains following the coincidence site lattice (CSL) boundary between the Bs and Cb or Bs and Gs. Therefore, it is possible that most of the Bs grains grew into Gs grains during recrystallisation in the position B sample, leaving Gs and Cb as a dominant texture in Positions A and B, respectively. CSL boundaries are special boundaries with lower energy than normal boundaries, and they have the highest mobility [57].

Figure 39 shows the EBSD map illustrating some of the texture components after recrystallisation anneal. Cube-textured grains in position A were found to be bigger in size as compared to the ones in position B, and this observation can be attributed to the presence of CSL boundaries. Since they have low energy and are very mobile, they can move rapidly, leading to a high growth rate in grains associated with them. This might be one of the reasons why position A had a higher and stronger Cb texture after recrystallisation.

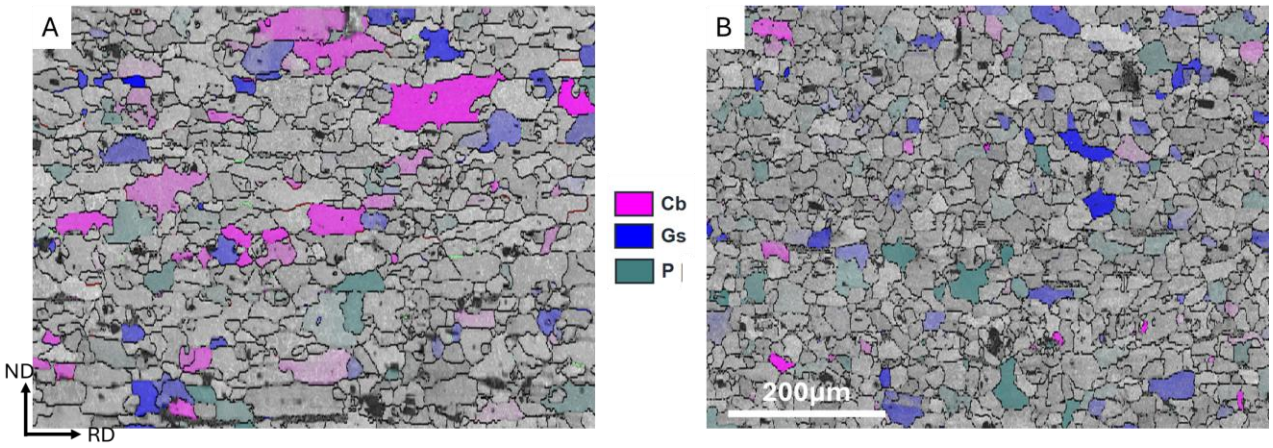

Figure 39 EBSD map of annealed metal strip of position A and position B illustrating texture components

6. Conclusion

This study focused on investigating the effects of interpass time variability experienced during hot finish rolling of AA3104 can body stock on a single stand reversing mill, where the leading and tailing ends of the sheet experience different inter-pass times.

The results indicate that the samples undergo substantial softening during extended inter-pass times, which reduces retained strain energy and subsequently lowers the driving force for recrystallisation. More pronounced effects were observed at longer interpass durations compared to shorter ones. This is highlighted by the formation of LAGBs, the formation of sub grains, and sub grain coarsening during extended interpass times, leading to a reduction in retained strain energy. This softening reduces the accumulated strain, thereby decreasing the overall recrystallisation kinetics during subsequent recrystallisation anneal.

As recrystallisation progresses, concurrent dispersoid formation may take place. These type II and III dispersoids promote the development of P texture, although its intensity remains weak, while simultaneously inhibiting the formation of Cb texture. Additionally, the presence of dispersoids appears to restrict grain growth, resulting in finer grain size.

In contrast, shorter interpass times facilitate faster recrystallisation kinetics. This condition favours the formation of a more random texture and enhances the development of Cb texture while limiting the formation of P texture. However, the increased recrystallisation kinetics associated with short interpass times also contribute to grain growth.

7. Recommendations

This research highlights the important effects of interpass time variability between Positions A and B during hot deformation. However, some additional studies are encouraged to further understand the texture development during hot deformation and how Cb texture can be enhanced to mitigate the development of ears during cup formation. Therefore, the following recommendations were drawn:

- Incorporate in situ EBSD to observe real-time changes in recrystallisation texture growth into the deformed matrix. It is believed that recrystallisation textured grains either nucleate or grow from deformation textured grains. Observing this transformation in real time can help identify specific deformation textures that transform into recrystallisation textures during annealing. It can further help determine the conditions at which those transformations occur in the presence or development of CLSs, as it is stated that some of the CSLs develop during the early stages of recrystallisation and diminish as it continues.

- To use complementary techniques like XRD to study a broader view of texture development. EBSD only measures the micro-texture, and to capture meaningful results which show repeatability and reliability, different sections of the sample must be tested, which could be costly and time-consuming, especially for deformed grains. Furthermore, it was very difficult and almost impossible to get a good index on the deformed grains due to recovery, which was causing overlapping of patterns, resulting in poor results. Therefore, to validate the obtained results through EBSD, complementary tests like XRD are necessary to capture the macro texture.

- TEM to quantify the stored energy within individual grains and sub-grain size. As explained above, it was difficult to get a good index on the deformed samples. As a result, the results were not reliable for grain analysis. Hence, TEM would be a perfect tool for further grain analysis. Moreover, since poor indexing is the result of pattern overlaps, and it has also been proved that static recovery and recrystallisation do occur during interpass time, the rolling simulation must be set up such that it also simulates the coiling and decoiling of the sheet during hot deformation on the single

stand reversible mill. Some of the grains will be well recovered and recrystallised with low dislocation density; as a result, a clear pattern will be constructed.

- Correlate mechanical properties with specific texture components using advanced modelling techniques
- The results suggested that there was a development of concurrent dispersoids (type II and III) during long interpass time and recrystallisation. Next, sets of experiments could involve electrical conductivity tests at every critical stage of deformation to determine the Mn remaining in the solution, which would be used to infer the amount of Mn precipitated. TEM can also be employed to further study the existence, the size, and the nature of these dispersoids.

8. References

[1] Y. Shi, H. Jin, and P. D. Wu, “Analysis of cup earing for AA3104-H19 aluminium alloy sheet,” *Eur. J. Mech. - A Solids*, vol. 69, pp. 1–11, May 2018, doi: 10.1016/j.euromechsol.2017.11.013.

[2] A. Singh *et al.*, “Prediction of earing defect and deep drawing behaviour of commercially pure titanium sheets using CPB06 anisotropy yield theory,” *J. Manuf. Process.*, vol. 33, pp. 256–267, Jun. 2018, doi: 10.1016/j.jmapro.2018.05.003.

[3] R. D. Doherty, “Recrystallization and texture,” *Prog. Mater. Sci.*, vol. 42, no. 1–4, pp. 39–58, Jan. 1997, doi: 10.1016/S0079-6425(97)00007-8.

[4] O. Engler, “Modelling of Microstructure and Texture and the Resulting Properties during the Thermo-Mechanical Processing of Aluminium Sheets,” *Mater. Sci. Forum*, vol. 519–521, pp. 1563–1568, Jul. 2006, doi: 10.4028/www.scientific.net/MSF.519-521.1563.

[5] P. Xia, Z. Liu, W. Wu, Q. Zhao, L. Lu, and S. Bai, “Texture Evolution in an Al-Cu-Mg Alloy During Hot Rolling,” *J. Mater. Eng. Perform.*, vol. 27, no. 7, pp. 3255–3267, Jul. 2018, doi: 10.1007/s11665-018-3427-2.

[6] C. Maurice and J. H. Driver, “Hot Rolling Textures of Aluminium,” *Mater. Sci. Forum*, vol. 157–162, pp. 807–812, May 1994, doi: 10.4028/www.scientific.net/MSF.157-162.807.

[7] W. Liu and J. Morris, “Effect of hot and cold deformation on the fibre rolling texture in continuous cast AA 5052 aluminium alloy,” *Scr. Mater.*, vol. 52, no. 12, pp. 1317–1321, Jun. 2005, doi: 10.1016/j.scriptamat.2005.02.031.

[8] S. Li, Q. Zhao, Z. Liu, and F. Li, “A review of texture evolution mechanisms during deformation by rolling in aluminium alloys,” *J. Mater. Eng. Perform.*, vol. 27, no. 7, pp. 3350–3373, Jul. 2018, doi: 10.1007/s11665-018-3439-y.

[9] J. Kraner *et al.*, “The Influence of the hot-rolling technique for en aw-8021b aluminium alloy on the microstructural properties of a cold-rolled foil,” *Mater. Tehnol.*, vol. 55, no. 6, Dec. 2021, doi: 10.17222/mit.2021.216.

[10] B. K. Chen and H. N. Kha, “Development of hot rolling practices for lithographic sheet using a thermo-mechanical and microstructural model of a reversing hot finishing mill,” *J. Mater. Process. Technol.*, vol. 152, no. 2, pp. 221–227, Oct. 2004, doi: 10.1016/j.jmatprotec.2004.03.028.

[11] Struers, “Metallographic preparation of aluminium and aluminium alloys,” Metallographic preparation of aluminium and aluminium alloys. [Online]. Available: Metallography of aluminium insight | Struers.com

[12] S. M. Amer, “Aluminium and Its alloys,” 2022, doi: 10.13140/RG.2.2.33040.07685.

[13] AlcoTec, “Understanding the alloys of aluminium.” [Online]. Available: http://alcotec.com/us/en/education/knowledge/techknowledge/understanding-the-alloys-of-aluminum.cfm

[14] C. Cavallo, “All about 3003 aluminium (properties, strength and uses).” [Online]. Available: https://www.thomasnet.com/articles/metals-metal-products/3003-aluminum/

[15] J. Hirsch, “AlMn1Mg1 for beverage cans en-aw 3104 processing, microstructure, simulation and property control,” in *Virtual fabrication of aluminium products: microstructural modelling in industrial aluminium production*, Weinheim: Wiley-VCH, 2006.

[16] O. Engler and K. Knarbakk, “Temper rolling to control texture and earing in aluminium alloy AA 5050A,” *MATEC Web Conf.*, vol. 326, p. 05002, 2020, doi: 10.1051/matecconf/202032605002.

[17] B. Hutchinson, “The cube texture revisited,” *Mater. Sci. Forum*, vol. 702–703, pp. 3–10, Dec. 2011, doi: 10.4028/www.scientific.net/MSF.702-703.3.

[18] V. Klosek, “Crystallographic textures,” *EPJ Web Conf.*, vol. 155, p. 00005, 2017, doi: 10.1051/epjconf/201715500005.

[19] S. Suwas and N. P. Gurao, “Crystallographic texture in Materials,” vol. 88, 2008.

[20] A. L. T. Martins, A. A. Couto, N. B. D. Lima, and G. F. C. Almeida, “Crystallographic texture evolution of aluminium alloy 3104 in the drawn and wall ironing (DWI) process,” *Mater. Res.*, vol. 22, no. 1, 2019, doi: 10.1590/1980-5373-mr-2019-0037.

[21] K. Koyama, S. Urayoshi, T. Tanaka, R. Shoji, Y. Tsuzuki, and H. Matsuda, “Development of low-earing can body stock using the 4-stand hot finishing mill at the fukui works,” *Furukawa Rev.*, no. 18, 1999.

[22] J. Humphreys, “Texture analysis: macrotexture, microtexture and orientation mapping.,” *J. Microsc.*, vol. 203, no. 2, pp. 231–232, Aug. 2001, doi: 10.1046/j.1365-2818.2001.00936.x.

[23] DoITPoMS, “Dissemination of IT for the promotion of materials science,” crystallographic texture. [Online]. Available: https://www.doitpoms.ac.uk/tlplib/crystallographic_texture/index.php

[24] H.-R. Wenk and P. V. Houtte, “Texture and anisotropy,” *Rep. Prog. Phys.*, vol. 67, no. 8, pp. 1367–1428, Aug. 2004, doi: 10.1088/0034-4885/67/8/R02.

[25] U. F. Kocks, C. N. Tome, and H. R. Wenk, *Texture and Anisotropy: Preferred orientations in polycrystals and their effect on materials properties*. United Kingdom: Cambridge University Press, 1998.

[26] M. A. Asadabad and M. J. Eskandari, “Electron diffraction,” in *Modern electron microscopy in physical and life sciences*, M. Janecek and R. Kral, Eds., InTech, 2016. doi: 10.5772/61781.

[27] L. A. Bendersky and F. W. Gayle, “Electron diffraction using transmission electron microscopy,” *J. Res. Natl. Inst. Stand. Technol.*, vol. 106, no. 6, p. 997, Nov. 2001, doi: 10.6028/jres.106.051.

[28] P. A. Midgley and A. S. Eggeman, “Precession electron diffraction – a topical review,” *IUCrJ*, vol. 2, no. 1, pp. 126–136, Jan. 2015, doi: 10.1107/S2052252514022283.

[29] Mimar Communications Ltd, “Electron Backscatter Diffraction,” Oxford Instruments. Accessed: May 04, 2023. [Online]. Available: https://www.ebsd.com/ebsd-explained/what-is-ebsd

[30] O. Engler, N. Mertens, and P. Van Dam, “Texture-based design of a convoluted cut-edge for earing-free beverage cans,” *J. Mater. Process. Technol.*, vol. 211, no. 7, pp. 1278–1284, Jul. 2011, doi: 10.1016/j.jmatprotec.2011.02.011.

[31] W. F. Hosford and J. L. Duncan, “The aluminum beverage can,” *Sci. Am.*, vol. 271, no. 3, pp. 48–53, Sep. 1994, doi: 10.1038/scientificamerican0994-48.

[32] F. Sun, P. Liu, and W. Liu, “Multi-level deep drawing simulations of AA3104 aluminium alloy using crystal plasticity finite element modelling and phenomenological yield function,” *Adv. Mech. Eng.*, vol. 13, no. 3, p. 168781402110012, Mar. 2021, doi: 10.1177/16878140211001203.

[33] W. Liu and B. K. Chen, “Sheet metal anisotropy and optimal non-round blank design in high-speed multi-step forming of AA3104-H19 aluminium alloy can body,” *Int. J. Adv. Manuf. Technol.*, vol. 95, no. 9–12, pp. 4265–4277, Apr. 2018, doi: 10.1007/s00170-017-1526-0.

[34] A. M. Zaky, A. B. Nassr, and M. G. El-Sebaie, “Optimum blank shape of cylindrical cups in deep drawing of anisotropic sheet metals,” *J. Mater. Process. Technol.*, vol. 76, no. 1–3, pp. 203–211, Apr. 1998, doi: 10.1016/S0924-0136(97)00349-X.

[35] J. Hirsch, “Texture evolution and earing in aluminium can sheet,” *Mater. Sci. Forum*, vol. 495–497, pp. 1565–1572, Sep. 2005, doi: 10.4028/www.scientific.net/MSF.495-497.1565.

[36] S. Kodukula, T. Manninen, and D. Porter, “Estimation of Lankford coefficients of austenitic and ferritic stainless steels using mean grain orientations from micro-texture measurements,” *ISIJ Int.*, vol. 61, no. 1, pp. 401–407, Jan. 2021, doi: 10.2355/isijinternational.ISIJINT-2020-256.

[37] O. Engler, “Modelling of rolling and recrystallization textures in the production of aluminium sheets,” *Mater. Sci. Forum*, vol. 408–412, pp. 1407–1412, Aug. 2002, doi: 10.4028/www.scientific.net/MSF.408-412.1407.

[38] O. Engler, L. Löchte, and K. F. Karhausen, “Modelling of recrystallisation kinetics and texture during the thermo-mechanical processing of aluminium sheets,” *Mater. Sci. Forum*, vol. 495–497, pp. 555–566, Sep. 2005, doi: 10.4028/www.scientific.net/MSF.495-497.555.

[39] A. Brahme, J. Fridy, H. Weiland, and A. D. Rollett, “Modelling texture evolution during recrystallization in aluminium,” *Model. Simul. Mater. Sci. Eng.*, vol. 17, no. 1, p. 015005, Jan. 2009, doi: 10.1088/0965-0393/17/1/015005.

[40] B. Bacroix and J. J. Jonas, “The influence of non-octahedral slip-on texture development in fcc metals,” *Textures Microstruct.*, vol. 8, pp. 267–311, 1988, doi: 10.1155/TSM.8-9.267.

[41] S. Panchanadeeswaran and D. P. Field, “Texture evolution during plane strain deformation of aluminium,” *Britian*, vol. 43, no. 4, pp. 1685–1692, Apr. 1995.

[42] J. Hirsch, “Texture evolution during rolling of aluminium alloys,” *Miner. Met. Mater. Soc. Light Met.*, Jan. 2008, [Online]. Available: https://www.researchgate.net/publication/286952758

[43] K. A. Annan, C. W. Siyasiya, and W. E. Stumpf, “Characterization of the texture evolution in AISI 430 and AISI 433 ferritic stainless steels during simulated hot rolling,” *MRS Adv.*, vol. 3, no. 34–35, pp. 1985–2002, Jul. 2018, doi: 10.1557/adv.2018.408.

[44] Y. Huang, Q. Li, Z. Xiao, Y. Liu, and H. Zhang, “Influence of precipitation on recrystallization texture of AA3104 aluminium alloy,” *J. Cent. South Univ.*, vol. 22, no. 10, pp. 3683–3688, Oct. 2015, doi: 10.1007/s11771-015-2910-2.

[45] J. J. Jonas, “Effect of quench and interpass time on dynamic and static softening during hot rolling,” *Steel Res. Int.*, vol. 76, no. 5, pp. 392–398, May 2005, doi: 10.1002/srin.200506027.

[46] S. Tangen, K. Sjølstad, T. Furu, and E. Nes, “Effect of concurrent precipitation on recrystallization and evolution of the P-texture component in a commercial Al-Mn Alloy,” *Metall. Mater. Trans. A*, vol. 41, no. 11, pp. 2970–2983, Nov. 2010, doi: 10.1007/s11661-010-0265-8.

[47] C.-Y. Yu, J.-P. Chang, S.-X. Ding, T.-Y. Tseng, and H.-C. Shih, “Influence of Si addition on the recrystallization texture of Al-Mn-Mg aluminium alloy”, *China Steel Tech. Rep.,* vol. 29, pp.67-73, 2016.

[48] S. Chakraborty, C. S. Patil, and S. R. Niezgoda, “Development of the Cube component $$ \left({\left\{ 001 \right\}\left\langle {100} \right\rangle } \right) $$ during plane strain compression of copper and its importance in recrystallization nucleation,” *Metall. Mater. Trans. A*, vol. 53, no. 2, pp. 503–522, Feb. 2022, doi: 10.1007/s11661-021-06513-0.

[49] R. Hu, T. Ogura, H. Tezuka, T. Sato, and Q. Liu, “Dispersoid formation and recrystallization behaviour in an Al-Mg-Si-Mn alloy,” *J. Mater. Sci. Technol.*, vol. 26, no. 3, pp. 237–243, Mar. 2010, doi: 10.1016/S1005-0302(10)60040-0.

[50] E. J. Giordani, A. M. Jorge, and O. Balancin, “Proportion of recovery and recrystallization during interpass times at high temperatures on a Nb- and N-bearing austenitic stainless-steel biomaterial,” *Scr. Mater.*, vol. 55, no. 8, pp. 743–746, Oct. 2006, doi: 10.1016/j.scriptamat.2006.05.015.

[51] L.-M. Yan, J. Shen, J.-P. Li, and B.-P. Mao, “Static softening behaviours of 7055 alloy during the interval time of multi-pass hot compression,” *Rare Met.*, vol. 32, no. 3, pp. 241–246, Jun. 2013, doi: 10.1007/s12598-013-0065-6.

[52] H. E. Vatne, R. Shahani, and E. Nes, “Deformation of cube-oriented grains and formation of recrystallized cube grains in a hot deformed commercial AlMgMn aluminium alloy,” *Acta Mater.*, vol. 44, no. 11, pp. 4447–4462, Nov. 1996, doi: 10.1016/1359-6454(96)00077-8.

[53] K. T. Kashyap, “On the origin of recrystallization textures,” *Bull. Mater. Sci.*, vol. 24, no. 1, pp. 23–26, Feb. 2001, doi: 10.1007/BF02704835.

[54] O. Engler, “On the origin of the R orientation in the recrystallization textures of aluminium alloys,” *Metall. Mater. Trans. A*, vol. 30, no. 6, pp. 1517–1527, Jun. 1999, doi: 10.1007/s11661-999-0088-7.

[55] M. H. Alvi, S. W. Cheong, H. Weiland, and A. D. Rollett, “Recrystallization and texture development in hot rolled 1050 aluminum,” *Mater. Sci. Forum*, vol. 467–470, pp. 357–362, Oct. 2004, doi: 10.4028/www.scientific.net/MSF.467-470.357.

[56] D. Nyung Lee , “Relationship between deformation and recrystallisation textures of FCC and BCC metals,” *Philos. Mag.*, vol. 85, no. 2–3, pp. 297–322, Jan. 2005, doi: 10.1080/14786430412331315734.

[57] Q. Zhao, Z. Liu, S. Bai, S. Li, Y. Hu, and P. Xia, “Coincidence site lattice boundary mechanism for the preferred growth of Goss and Cube grains during annealing in an Al-Cu-Mg alloy,” *Mater. Charact.*, vol. 141, pp. 193–211, Jul. 2018, doi: 10.1016/j.matchar.2018.04.030.

[58] J.-J. Fundenberger and B. Beausir, *Analysis tools for electron and x-ray diffraction (ATEX)*. (2017). Université de Lorraine - Metz. [Online]. Available: www.atex-software.eu

[59] D. Slater, “Development of open-source software for repeatable processing of mechanical test data,” University of Cape Town, Cape Town.

[60] K. P. Rao, Y. K. D. V. Prasad, and E. B. Hawbolt, “Study of fractional softening in multi-stage hot deformation,” *J. Mater. Process. Technol.*, vol. 77, no. 1–3, pp. 166–174, May 1998, doi: 10.1016/S0924-0136(97)00414-7.

[61] A. Ghosh, A. Elasheri, N. Parson, and X.-G. Chen, “Microstructure and texture evolution during high-temperature compression of Al-Mg-Si-Zr-Mn alloy,” *Mater. Charact.*, vol. 205, p. 113312, Nov. 2023, doi: 10.1016/j.matchar.2023.113312.

[62] F. J. Humphreys and M. Hatherly, *Recrystallization and related annealing phenomena*, 2. impr. Oxford: Pergamon, 2002.

[63] R. L. Doiphode, S. V. S. N. Murty, N. Prabhu, and B. P. Kashyap, “Microstructure and texture evolution during annealing of caliber rolled Mg–3Al–1Zn alloy,” *Trans. Indian Inst. Met.*, vol. 68, no. S2, pp. 317–321, Sep. 2015, doi: 10.1007/s12666-015-0621-x.

[64] S. W. Cheong and H. Weiland, “Understanding a microstructure using GOS (grain orientation spread) and its application to recrystallization study of hot deformed Al-Cu-

Mg alloys," *Mater. Sci. Forum*, vol. 558–559, pp. 153–158, Oct. 2007, doi: 10.4028/www.scientific.net/MSF.558-559.153.

[65] K. Huang, K. Zhang, K. Marthinsen, and R. E. Logé, "Controlling grain structure and texture in Al-Mn from the competition between precipitation and recrystallization," *Acta Mater.*, vol. 141, pp. 360–373, Dec. 2017, doi: 10.1016/j.actamat.2017.09.032.

[66] E. Cantergiani, G. Falkinger, S. Mitsche, M. Theissing, S. Klitschke, and F. Roters, "Influence of strain rate sensitivity on cube texture evolution in aluminium alloys," *Metall. Mater. Trans. A*, vol. 53, no. 8, pp. 2832–2860, Aug. 2022, doi: 10.1007/s11661-022-06710-5.

[67] J. Xie, X. Chen, Y. Cao, G. Huang, and Q. Liu, "The evolution of main textures and the formation of P orientation with nanoprecipitates after friction stir processing," *J. Manuf. Process.*, vol. 80, pp. 591–599, Aug. 2022, doi: 10.1016/j.jmapro.2022.06.033.

[68] L. Huang *et al.*, "Influence of pre-recovery on the subsequent recrystallization and mechanical properties of a twin-roll cast Al-Mn alloy," *Mater. Sci. Eng. A*, vol. 682, pp. 63–72, Jan. 2017, doi: 10.1016/j.msea.2016.11.018.

[69] P. Du *et al.*, "Effect of high-pressure heat treatment on the recrystallization and recrystallization texture of CC AA 3003 aluminium alloy," *J. Mater. Res. Technol.*, vol. 19, pp. 2388–2401, Jul. 2022, doi: 10.1016/j.jmrt.2022.06.016.

[70] J. J. Sidor, "Effect of hot band on texture evolution and plastic anisotropy in aluminium alloys," *Metals*, vol. 11, no. 8, p. 1310, Aug. 2021, doi: 10.3390/met11081310.

[71] O. Engler, B. Mulders, and J. Hirsch, "Influence of deformation temperature and strain rate on the recrystallisation nucleation of AlMg1Mn1," *Z.Metallkd*, vol. 87, 1996.

[72] Q. Zhao, Z. Liu, S. Li, T. Huang, P. Xia, and L. Lu, "Evolution of the brass texture in an Al-Cu-Mg alloy during hot rolling," *J. Alloys Compd.*, vol. 691, pp. 786–799, Jan. 2017, doi: 10.1016/j.jallcom.2016.08.322.

9. Appendices

A. Nominal strain rates of Positions A and B during deformation

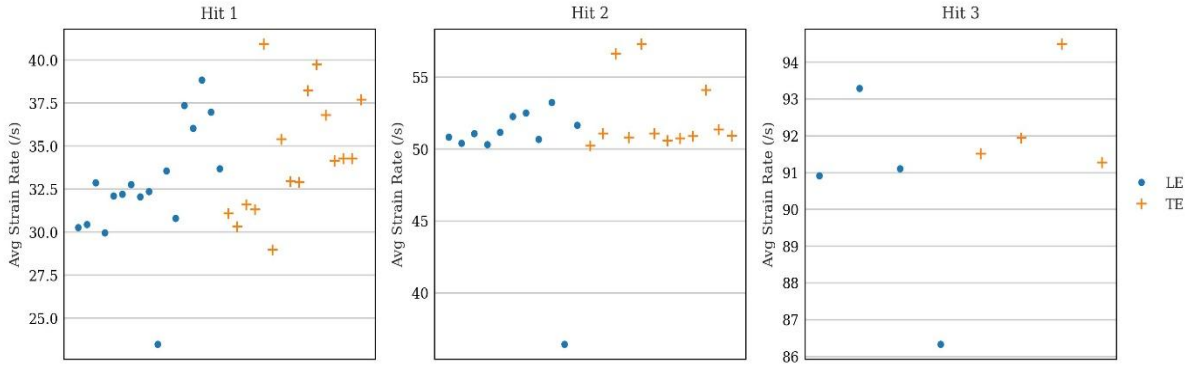

B. Flow stress curves of Positions A and B during deformation

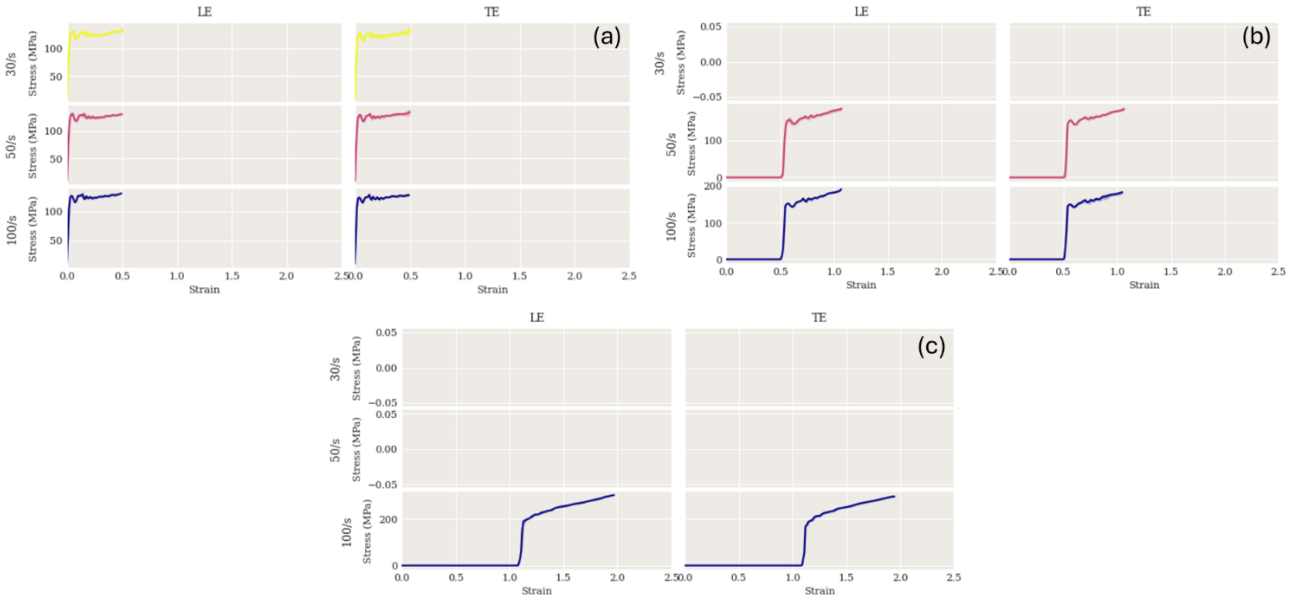

C. Pole figures of position A during deformation

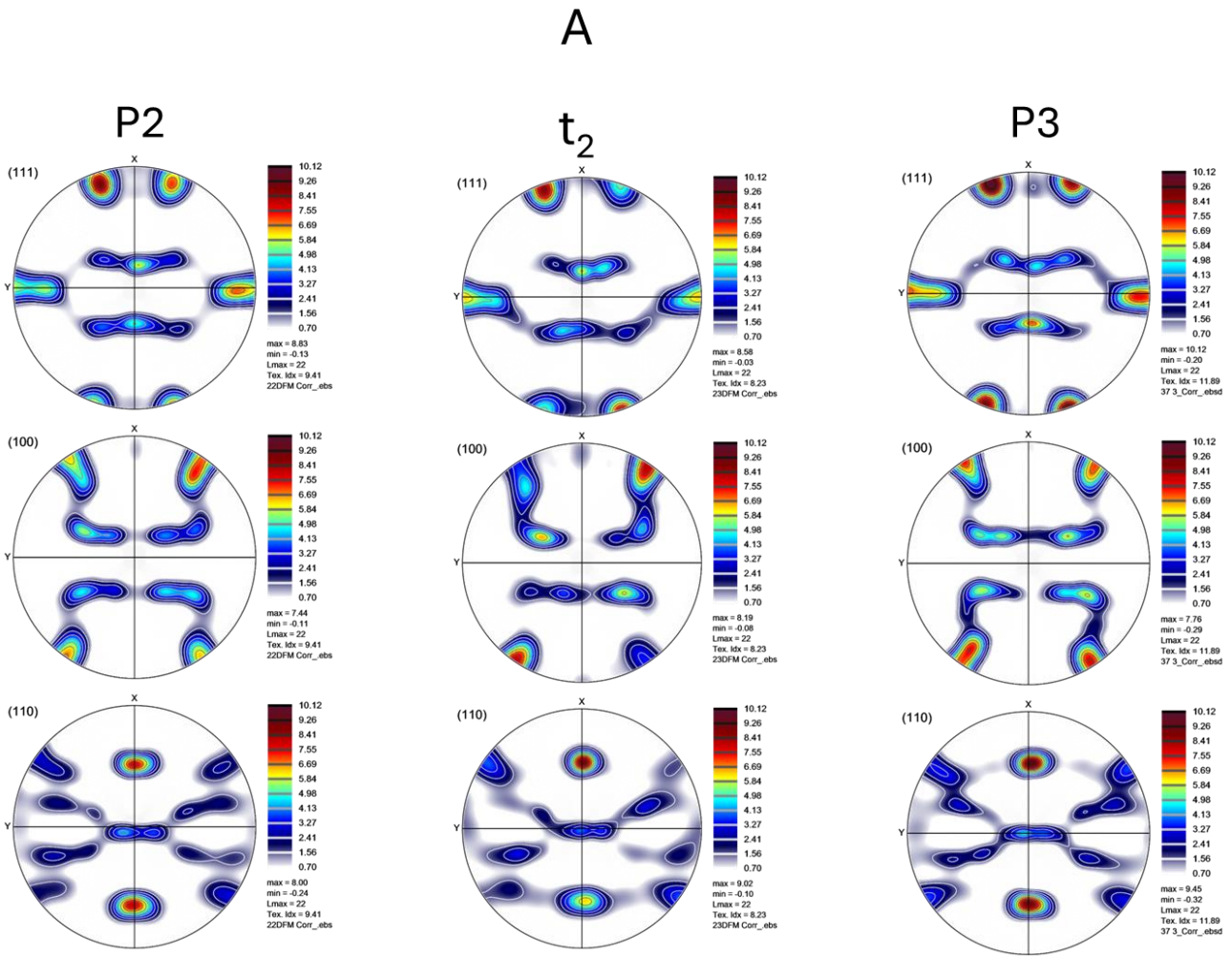

D. Pole figures of position B during deformation

B

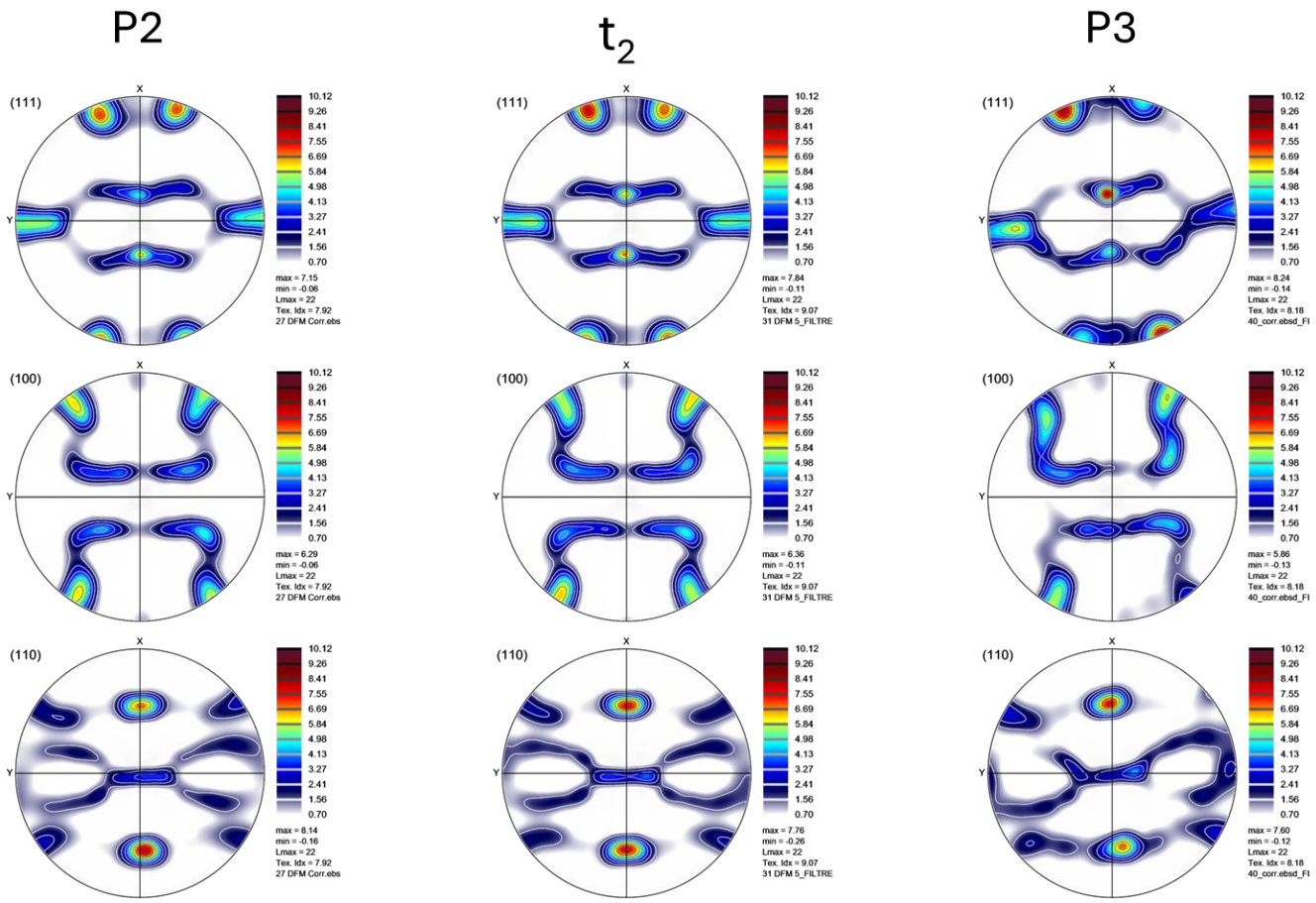

E. Pole figures of Positions A and B after deformation P3 and recrystallisation anneal

P3_A

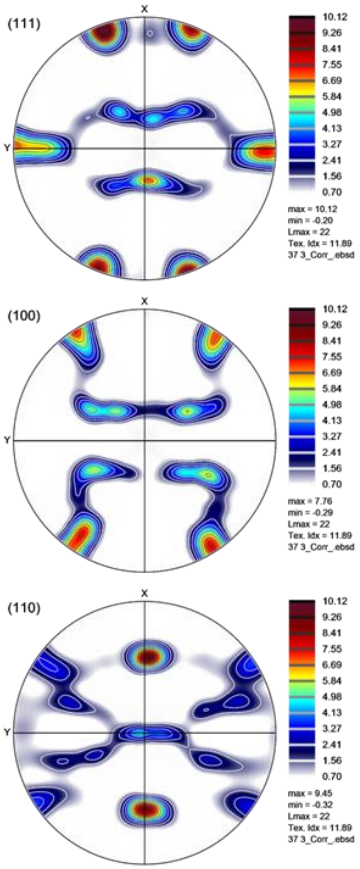

RXN_A

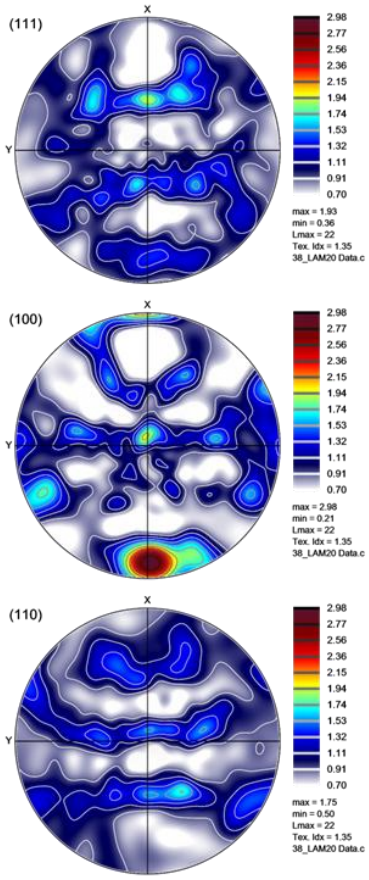

P3_B

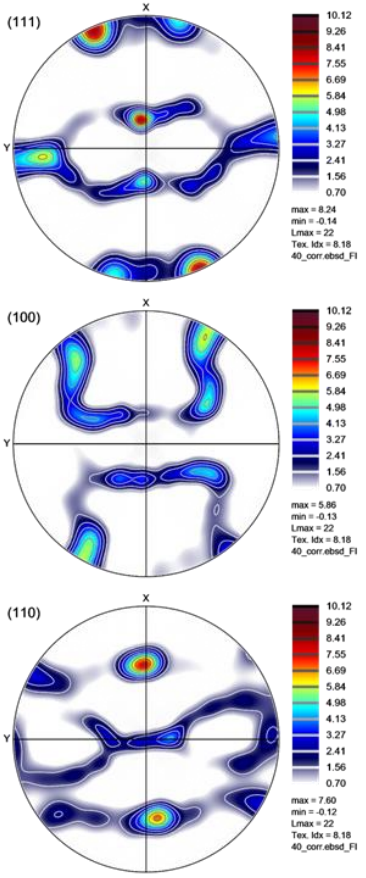

RXN_B

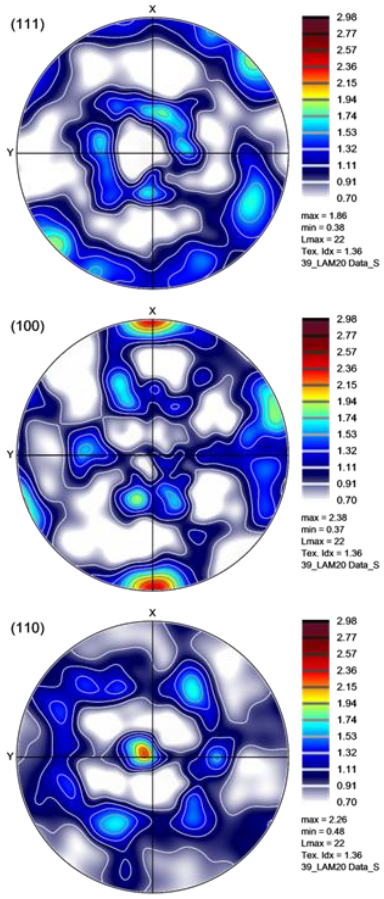

F. Texture components volume fraction based on ODF

G. Texture components volume fraction based on discrete orientations

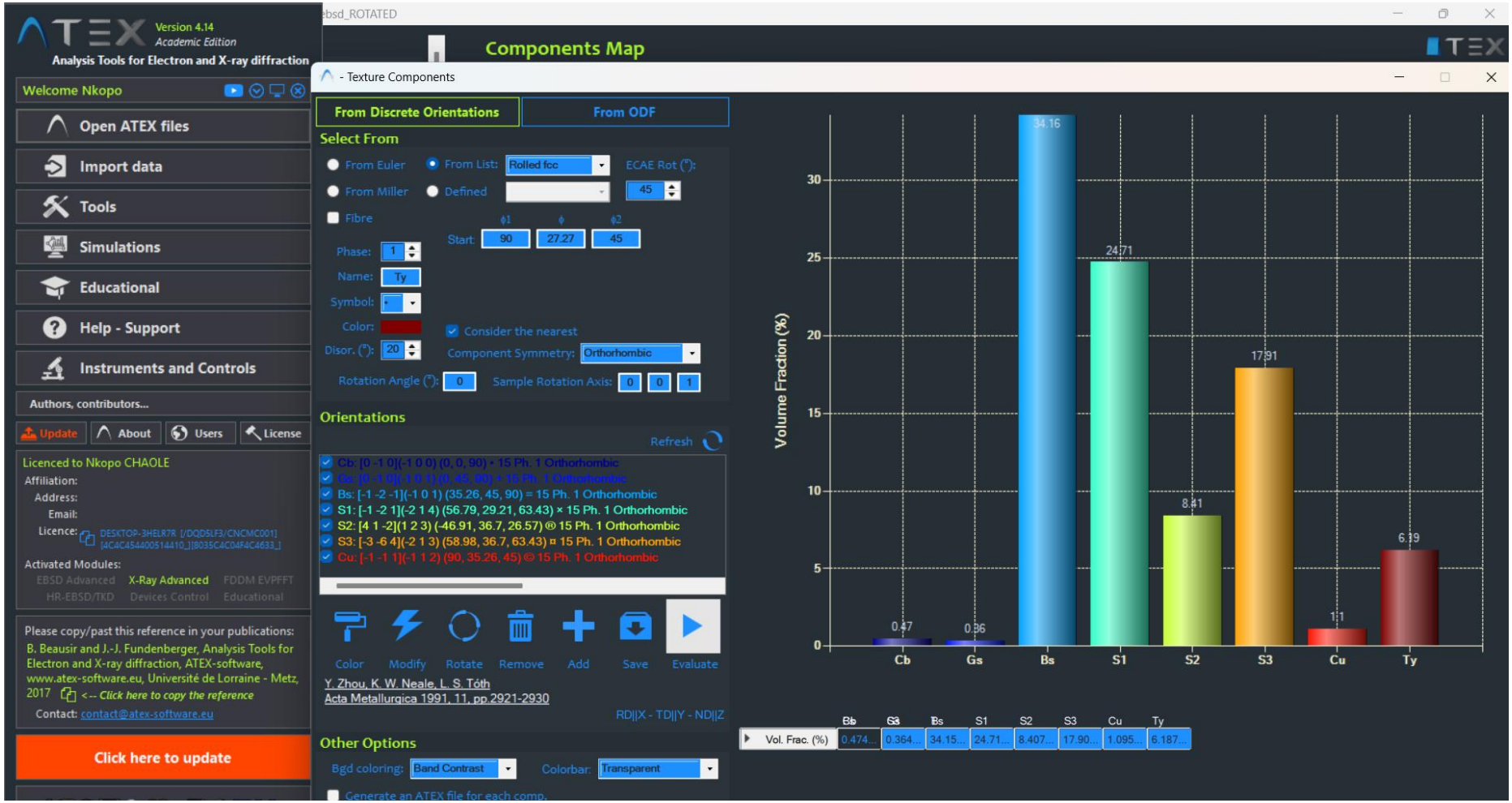

H. Non-Octahedral slip systems percentage calculations.